Progress in Materials Science 97 (2018) 448–487

Contents lists available at ScienceDirect

Progress in Materials Science

journal homepage: www.elsevier.com/locate/pmatsci

Corrosion in the molten fluoride and chloride salts and materials development for nuclear applications

Shaoqiang Guo[a,*], Jinsuo Zhang[a,b,*], Wei Wu[b,c], Wentao Zhou[b]

[a] Nuclear Engineering Program, Department of Mechanical Engineering, Virginia Polytechnic Institute and State University, Blacksburg, VA 24061, United States
[b] Nuclear Engineering Program, Department of Mechanical and Aerospace Engineering, The Ohio State University, Columbus, OH 43210, United States
[c] School of Chemical Engineering and Technology, Xi'an Jiaotong University, Xi'an 710049, PR China

ARTICLE INFO

Keywords:
Materials corrosion
Fluoride salts
Chloride salts
Molten salt reactor
Spent fuel reprocessing

ABSTRACT

Next-generation nuclear reactor concepts and advanced techniques for reprocessing spent nuclear fuel (SNF) are drawing great attention in the nuclear field. Molten halide salts have been proposed as the fuel solvent and coolants for many molten salt reactor (MSR) concepts, and the electrolyte for the electrochemical separation of the SNF. The major concern of using molten salts is the corrosion of the structural materials imposed by these extreme environments. Materials corrosion is more challenging in the molten salt nuclear systems than in the traditional water reactors as the formation of the passivating oxide layer on the corrosion resistant alloys becomes thermodynamically unfavorable in molten salts and the use of many corrosion resistant alloys is restricted. This review takes a comprehensive approach covering all relevant work in the field: corrosion data accumulated since the 1950s to date, major corrosion problems and corresponding mechanisms, metallurgical factors, historical development of corrosion resistant alloys and recent attempts. The key environmental factors influencing corrosion in various nuclear systems, electrode kinetics, thermodynamic properties, and corrosion prevention techniques are also reviewed. Finally, current progress and challenges are summarized with an attempt at identifying knowledge gaps and future research directions.

1. Introduction

Use of molten salts instead of aqueous media is attractive in many applications such as electrolyte [1,2], extraction [3], thermal energy storage and heat transfer fluid [4], etc. In nuclear power systems there are two significant applications of molten salts: electrochemical separation (EChem) for SNF reprocessing and molten salt cooled/fueled nuclear reactors. The EChem of SNFs, also known as a non-aqueous dry processing, separates U, Pu, and minor actinides (MAs) from fission products in SNF by oxidation-reduction reactions at high temperatures [5] using molten salt as the electrolyte. The electrorefiner is the core component of the Echem using electrorefining technology. For the metallic fuel, the chopped spent fuels are placed into the anodic basket and then immersed into the molten salt. The alkali, alkaline earth, and rare earth fission products are oxidized and dissolved as corresponding chlorides into the molten salt [6]. Noble metallic fission products and other undissolved material such as zirconium will remain in the anodic basket. By applying a current, most of the U, Pu, and MAs can be electro-oxidized and dissolved as demonstrated by the laboratory experiments in which up to 99.7 wt% U in the SNF was dissolved [7]. Most of the dissolved uranium can be selectively

---

[*] Corresponding authors at: Nuclear Engineering Program, Department of Mechanical Engineering, Virginia Polytechnic Institute and State University, Blacksburg, VA 24061, United States.
E-mail addresses: guos1987@vt.edu (S. Guo), zjinsuo@vt.edu (J. Zhang).

https://doi.org/10.1016/j.pmatsci.2018.05.003
Received 7 August 2017; Received in revised form 24 February 2018; Accepted 14 May 2018

electro-deposited at a solid cathode in the electro-refiner, while others (e.g., Pu, MAs, and rare earth fission products) are either electro-reduced in the liquid Cd or Bi cathode or remained in the melt and basket. For spent oxide fuel, an additional electrochemical process, electrolytic reduction, is needed to convert the oxide fuel into their metallic forms before electrorefining [8]. The spent oxide fuel can also be recovered by the electrowinning process alone which includes multiple steps [9]. However, it is also possible to electrorefine spent oxide fuel directly, through which 70–80% of UO_2 in the spent fuel can be recovered on a graphite cathode with meager amounts of fission products [10]. For recycling the salt, the accumulated actinides and rare earth fission products in the salt can be collected through an electrolysis process in which chlorine gas will be generated at the anode [11]. During the EChem processes, many corrosive species such as gaseous oxygen and chlorine will be introduced in the system, which causes the concern for structural material corrosion. Therefore, more detailed knowledge regarding the long-term materials performance, such as the corrosion resistance of materials used for the structural components and anodes that are exposed to high temperature and high redox potentials, is one of the key concerns of using EChem for processing SNF.

The molten salt-cooled/fueled reactor system is one of the Gen.IV reactor concepts [12]. For the Molten Salt Breeder Reactor (MSBR), an early concept developed and tested at Oak Ridge National Laboratory (ORNL), molten LiF-BeF_2-ThF_4-UF_4 was selected as fuel and coolant. It was recognized that the Ni-base alloys exhibited superior corrosion resistance to this type of molten salt if the salt redox condition was well controlled [13]. Recently, there are a number of advanced MSR concepts being considered by industry and the U.S. Department of Energy that feature molten fluoride salts as the fuel and/or coolant including, for example, fluoride salt-cooled high-temperature reactors (FHRs). In general, these systems have many attractive features including low-pressure operation, efficient high-temperature power conversion, and passive heat rejection. The preferred salts for these systems consist of LiF mixed with other fluorides such as LiF-BeF_2 and LiF-ThF_4. The corrosion of pure salt is found to be low. However, contaminants caused by ingress of water or oxygen, and neutron irradiation of ^{6}Li in the salt can make the salt more oxidizing [14]. This may result in the corrosion of transition metals such as Ni, Fe, and Cr which are constituents of the structural materials. The released corrosion products in the salt also affect the fuel/coolant properties. Therefore, the material corrosion must be considered when designing a molten salt cooled/fueled reactor system.

Compact oxide layers are often used as corrosion barriers in the nuclear reactor system, for example, in the liquid lead alloy cooled reactor, the oxide layers formed on the structure material are effective barriers to mitigate the corrosion by the liquid metal coolant [15]. However, the formation of oxide barrier layer is challenged in molten chloride and fluoride salt systems because of the presence of chlorine or fluorine ions. The molten halide salt corrosion proceeds via active dissolution without the presence of oxide layer or a mechanism of “fluxing” which is a synergistic process of degrading the metal by alternate chloride dissolution and oxide scale formation [16].

In recent years, the application of molten salt technology has developed a renewed interest in the nuclear industry. There are few brief review article [17] and chapters [18,19] on the corrosion phenomena in molten fluorides and the alloy development for different MSRs. However, no reviews take a comprehensive approach covering all aspects of the research efforts such as material corrosion in molten chlorides, corrosion and redox control in nuclear fusion applications, electrode kinetics, effects of alloying element and grain size, and effects of radiation on corrosion. Furthermore, there are no reviews inclusive of the extensive molten salt corrosion studies in the past five years during which the research progress has been bolstered from the successful application of electrochemical techniques and other innovative approaches. This paper presents a critical review of the material corrosion by molten fluoride and chloride salts in the applications of nuclear energy systems. The review is organized as follows: Section 2 introduces the major molten salts selected for various nuclear applications and summarizes the salt properties. Section 3 devotes to understanding the molten salt corrosion and material performance, for example, the selective dissolution of Cr from alloy in both thermodynamic and electrochemical considerations. Section 4 is a systematic review of the key factors that influence material corrosion in molten fluorides. This section covers major corrosion problems and corresponding mechanisms, environmental factors, effects of alloying elements and grain size on the corrosion resistance, and the present status of the materials development. Section 5 reviews the interacted effects of oxidant impurities, alloying elements, and oxide layer composition on the material performance in molten chloride salts. Section 6 is a review of redox control techniques that were proposed for corrosion prevention in nuclear molten salt systems. Finally, the current understanding and remaining challenges on the material corrosion in molten fluorides and chlorides are summarized with an attempt to identify the future research direction.

2. Molten salt properties

2.1. Choice of molten salt

Molten chlorides were recognized as suitable candidates for Echem of the SNFs. For electrorefining of spent metallic fuels, the process was operated at temperatures in the range of 450–500 °C, molten LiCl-KCl eutectic salt was selected. For the electrowinning of spent oxide fuels, the typical operation temperature was 700 °C, and molten NaCl-KCl eutectic was chosen. The electrolytic reduction of spent oxide fuel to their metallic forms was operated at 650 °C, and molten LiCl salt with a low concentration of Li_2O was used. The feasibility of using an alternative molten salt media LiF-CaF_2 eutectic for reprocessing the spent fuels has also been investigated recently for the separation of actinides and lanthanides operated at 860 °C [20–22].

The molten fluorides are also considered as the fuel and/or coolant for many MSR concepts. Selection of molten salt for MSRs depends on whether it is used for a salt-fueled or salt-cooled reactor, and whether it is used for the primary or intermediate circuit. In the salt-fueled reactor, the fuel is dissolved as fluorides within the carrier salt. The fuel carrier salt must fulfill certain criteria including low neutron cross-section for the solvent components, radiation stability, thermal stability, the adequate solubility of fuel, the adequate heat transfer and hydrodynamic properties, chemical compatibility with container and moderator materials, etc. [23]. Fluoride salts made of alkali metal and alkaline earth elements meet these requirements well. For thermal breeder MSRs, the neutron economy is very critical, and the selection of the carrier salt is limited by the elements with very low thermal neutron absorption cross-section. The $^7LiF\text{-}BeF_2$ salts are the prime choice with very low neutron absorption cross-section of ^7Li ($\sigma_{thermal} = 0.045$ barn) and Be ($\sigma_{thermal} = 0.0088$ barn) [24]. Two examples are the Molten Salt Reactor Experiment (MSRE) test reactor [25] and MSBR [26] developed at ORNL in the 1960s and 1970s. MSBR utilized $^7LiF\text{-}BeF_2$ carrier salt with fertile (ThF_4) and fissile elements (UF_4) as the fuel salt while MSRE fuel salt contains additional 5 mol% ZrF_4 ($\sigma_{thermal} = 0.18$ barn) as oxygen getter. Recent molten salt fueled reactor designs focus on the nonmoderated concepts with intermediate/fast neutron spectrum, including the Molten Salt Actinide Recycler and Transmuter (MOSART) [27] designed in Russia, the Molten Salt Fast Reactor (MSFR) concept [28] proposed in France, and very recent Molten Chloride Fast Reactor (MCFR) concept [29] in the United States. These concepts are attractive because the fuel can be made from the spent oxide fuels produced in current pressurized water reactors, thus reducing the cost of fuel fabrication and reprocessing. For the salt selection of the nonmoderated concepts, fluorides of Na, K, Rb, and Ca can be considered as the components of the fuel carrier salt as their neutron absorption cross-sections are sufficiently low in fast spectrum [24]. One example is the MOSART, for which the candidate fuel carrier salt is $LiF\text{-}NaF\text{-}BeF_2$ or $LiF\text{-}BeF_2$. The neutron absorption cross-section of ^{35}Cl in fast spectrum is also comparatively less than in the thermal spectrum ($\sigma_{fast} = 0.0011$ barn, $\sigma_{thermal} = 43.63$ barn). Thus molten chloride salts have also been proposed for fast reactors such as MCFR and REBUS-3700 concepts [30].

In the salt-cooled reactor, the fuels are solid and isolated from the primary salt coolant. A wider choice of fluoride salts can be considered because some salt performance such as the adequate solubilities of fuel components and fission products are not required. ORNL recently recommended to consider two types of salts as the primary coolant [23]: (1) Salts that have been shown in the past to support the least corrosion (e.g., salts containing BeF_2 and ZrF_4 in the concentration range 25–40 mol%); (2) Salts that provide the opportunity for controlling corrosion by establishing a very reducing salt environment (e.g., the alkali-fluoride salts and the BeF_2 containing salts). Based on these considerations, the $LiF\text{-}BeF_2$ eutectic has been proposed for the FHR concept [31].

For the coolant salt used in the intermediate loop, additional salts can be considered since it is outside the neutron field. The alkali fluoride salt, LiF-NaF-KF, which has superior heat transfer properties but poor thermal neutronic performance is one of the most promising intermediate coolant candidates [24]. The alkali fluoroborates salts and chloride salts that meet the basic requirements (e.g., heat-transfer properties, thermochemical stability, chemical compatibility, etc.) have also been considered as the intermediate coolant candidates.

2.2. Physical property

Corrosion of metals in molten salt involves the electrochemical charge-transfer process on the metal-electrolyte interface and the mass-transfer of involved species such as oxidants across the diffusion boundary layer. The charge-transfer rate can be limited by the mass-transfer rate which has a maximum value for a given flowing system. The mass-transfer rate is the product of the concentration gradient of the corresponding species and its mass-transfer coefficient which depends on the diffusivity, flow velocity, fluid physical properties, and the flow geometry [32]:

$$Sh = \frac{k_m L}{D} = \mathrm{A} Re^{\alpha} Sc^{\beta} \tag{1}$$

where k_m is the mass-transfer coefficient, m/s; D is the diffusivity, m^2/s; Sh is the Sherwood number; Reynolds number $Re = \rho v L/\mu$; Schmidt number $Sc = \mu/\rho D$; L is the characteristic dimension, m; v is the flow velocity, m/s; ρ is the density of the fluid, kg/m^3; μ is the dynamic viscosity of the fluid, Pa·s; and α, β, and A are the empirical factors depending on the flow pattern and the system geometry.

Eq. (1) indicates $k_m \propto (\rho/\mu)^{\alpha-\beta}$ where the value of $\alpha - \beta$ is 0.53 for turbulent flow in round pipe. This means that a larger ratio of the salt density to viscosity may lead to higher corrosion rate in mass-transfer-controlled case. Physical properties of some molten salts used in the nuclear field are summarized in Table 1. As the temperature increases, the density of the molten salt decreases linearly while the viscosity decreases exponentially. The density and viscosity of all fluoride salts except $LiF\text{-}CaF_2$ are recommended from Ref. [24]. The density correlations for LiCl-KCl, NaCl-KCl, and $LiF\text{-}CaF_2$ are obtained from the available data summarized in Refs. [33–35]. The viscosity correlation for LiCl-KCl is from Ref. [36], while the viscosity correlation for NaCl-KCl is based on the data

Table 1
Physical properties of the salts [24,33 – 36].

Properties	Composition (mol%)	Melting point (°C)	Density[a] (kg/m^3)	Viscosity[a] (mPa·s)
LiCl-KCl	59.5–40.5	350	2023.3–0.5238T	0.0861exp(2517/T)
NaCl-KCl	50–50	658	2132.9–0.5679T	0.0273exp(4055/T)
$LiF\text{-}BeF_2$	67–33	460	2146.3–0.4884T	0.116exp(3755/T)
LiF-NaF-KF	46.5–11.5–42	454	2579.3–0.6240T	0.0249exp(4476/T)
$LiF\text{-}BeF_2\text{-}ThF_4$	71.7–16–12.3	498	4124.3–0.8690T	0.062exp(4636/T)
$LiF\text{-}NaF\text{-}BeF_2\text{-}PuF_3$	20.3–57.1–21.2–1.3	502	2759.9–0.5730T	0.0996exp(3724/T)
$LiF\text{-}CaF_2$	80–20	769	2450.5–0.3683T	–

[a] T in Kelvin.

summarized in Ref. [35]. Based on current knowledge, there is no data on viscosity for LiF-CaF_2. The 2LiF-BeF_2 and 46.5LiF-11.5NaF-42KF salts are often named FLiBe and FLiNaK respectively. Experimental results from ORNL's flow loop showed generally more severe corrosion in FLiNaK compared to other fluoride salts including FLiBe and LiF-BeF_2 based salts [23]. One possible reason that might have been ignored in the past is the higher mass transfer coefficients in FLiNaK. Based on the correlations in Table 1, the ratio of ρ/μ of FLiNaK is about 1.7–2.6 times greater than FLiBe, LiF-BeF_2-ThF_4, and LiF-NaF-BeF_2-PuF_3 salts at 700 °C, indicating a higher mass transfer rate in FLiNaK.

2.3. Thermodynamic properties

The major cations in the molten salt may act as oxidants to cause metal corrosion, depending on their reduction potentials. To calculate the reduction potential, the activity of the corresponding species must be known. In this section, the methods to obtain the activity of the salt constituents are introduced and available experimental correlations for typical salts are summarized.

For ideal mixtures, the mixing enthalpy is zero, that is $\Delta H^{i,m} = 0$, while the entropy can be expressed by:

$$\Delta S^{i,m} = -R\sum_j n_j \ln N_j \tag{2}$$

where n_j is the molar number of component j; N_j is the corresponding molar fraction. If the total molar number of the mixture is 1, $n_j = N_j$. The mixing free energy for the ideal mixture can be calculated by:

$$\Delta G^{i,m} = -\Delta S^{i,m}T = RT\sum_j n_j \ln N_j \tag{3}$$

which depends on the mixing temperature and mixture composition. For the non-ideal molten salt mixture, the Gibbs free energy can be expressed by [37]:

$$\Delta G^{m} = RT\sum_j n_j \ln a_j \tag{4}$$

where a_j is the activity of the component j and $a_j = \gamma_j X_j$; γ and X are activity coefficient and molar fraction, respectively. Therefore, Eq. (4) can be rewritten as:

$$\Delta G^{m} = RT\sum_j n_j \ln X_j + RT\sum_j n_j \ln \gamma_j = \Delta G^{i,m} + \Delta G^{e,m} \tag{5}$$

Particularly, for a binary salt mixture with a molar number of one:

$$\Delta G^{i,m} = RT(X_1 \ln X_1 + X_2 \ln X_2) \tag{6}$$

For simple mixture without chemical compound formation, the mixing excess Gibbs energy can be expressed by [38]:

$$\Delta G^{e,m} = X_1 G_1^{e,m} + X_2 G_2^{e,m} \tag{7}$$

where $G_1^{e,m} = RT\ln\gamma_1 = H_1^{e,m} - S_1^{e,m}T$; $G_2^{e,m} = RT\ln\gamma_2 = H_2^{e,m} - S_2^{e,m}T$.

Therefore, the activity coefficient of each component of a binary mixture without chemical compound formation can be calculated if the mixing Gibbs energy is known.

For LiCl-KCl, the correlation for excess Gibbs energy was obtained by analyzing the available experimental data [38]:

$$\Delta G^{e,m}_{\mathrm{LiCl-KCl}}(\mathrm{J/mol}) = X_{\mathrm{LiCl}}X_{\mathrm{KCl}}[(-17570-377X_{\mathrm{LiCl}})-(-7.627+4.958X_{\mathrm{LiCl}})T] \tag{8}$$

For NaCl-KCl, the mixing entropy is found to be zero, and the mixing enthalpy can be written as [38]:

$$H^{e,m}(\mathrm{J/mol}) = X_{\mathrm{NaCl}}X_{\mathrm{KCl}}(-2050-272X_{\mathrm{KCl}}) \tag{9}$$

For LiF-CaF_2, the mixing entropy can also be neglected, and the mixing enthalpy was found to be [39]:

$$H^{e,m}(\mathrm{J/mol}) = X_{\mathrm{LiF}}X_{\mathrm{CaF_2}}(-5292-378X_{\mathrm{CaF_2}}) \tag{10}$$

The partial Gibbs excess energy (or the activity coefficient) of each component can be calculated by the integral Gibbs excess energy [40]:

$$RT\ln\gamma_i = q_i G^{e,m} + (q_1X_1 + q_2X_2)(1-X_i)\frac{dG^{e,m}}{dX_i} \tag{11}$$

where q_i is the cation charge number.

For LiF-BeF_2, the activity due to chemical reactions must be considered as a chemical compound $LiBeF_3$ is formed in the mixture [41]. Fortunately, correlations for calculating the integral activity (sum of activities due to physical mixing and chemical reactions) have been developed [42]. The correlations provided by Hitch and Baes [43] are given below:

$$\log_{10}\gamma_{\mathrm{BeF_2}} = A_2X_{\mathrm{LiF}}^2 + A_3X_{\mathrm{LiF}}^3 + A_4X_{\mathrm{LiF}}^4 + A_5X_{\mathrm{LiF}}^5 \tag{12}$$

$$\log_{10}\gamma_{\mathrm{LiF}} = B_0 + B_2X_{\mathrm{LiF}}^2 + B_3X_{\mathrm{LiF}}^3 + B_4X_{\mathrm{LiF}}^4 + B_5X_{\mathrm{LiF}}^5 \tag{13}$$

where $A_2 = 3.878{-}2354/T$, $A_3 = -40.738 + 36293/T$, $A_4 = 94.4{-}84871/T$, $A_5 = -67.418 + 52924/T$, $B_0 = 0.938/T$, $B_2 = -36.973 + 14653/T$, $B_3 = 126.1{-}74589/T$, $B_4 = -158.42 + 113592/T$, $B_5 = 67.42{-}52924/T$.

Except for the correlations based on experimental data, a modified quasi-chemical model has been developed to calculate the thermodynamic properties of multi-component salt mixtures [44]. The model has been successfully applied to study the fluoride mixtures [45] and chloride mixtures [46].

3. Molten salt corrosion fundamentals

3.1. Thermodynamic fundamental

Corrosion of structural materials in molten salts is an irreversible electrochemical process involving the anodic dissolution of metal and the cathodic evolution of the oxidant in the salt. The anodic dissolution of metal can be expressed as:

$$\mathrm{M} \rightarrow \mathrm{M}^{n+} + n\mathrm{e}^- \tag{14}$$

where M represents the metallic element such as Ni, Fe, Cr, Co in the structural material, n is the number of exchanged electrons.

The cathodic reduction of oxidant in the salt can be written as:

$$\mathrm{Ox} + n\mathrm{e}^- \rightarrow \mathrm{Red} \tag{15}$$

where Ox and Red represent the oxidant and its corresponding reductant, respectively.

The combination of the partial anodic reaction (14) and the partial cathodic reaction (15) yields the overall electrochemical corrosion reaction:

$$\mathrm{M} + \mathrm{Ox} \rightarrow \mathrm{M}^{n+} + \mathrm{Red} \tag{16}$$

To allow the corrosion reaction (16) to occur spontaneously, the Gibbs free energy change of the corrosion reaction must be negative. For an electrochemical reaction, the Gibbs free energy change can be expressed as:

$$\Delta G = -nF\Delta E \tag{17}$$

where ΔG is the Gibbs free energy change per mole of reaction, J/mol; F is Faraday constant, 96,485 C/mol; $\Delta E = E_c{-}E_a$ is the potential difference; E_a and E_c are the redox potential of the anodic electrode reaction (14) and cathodic electrode reaction (15) in V, respectively.

If E_c is more positive than E_a, i.e., $\Delta G < 0$, the metal in molten salt will be corroded spontaneously. The redox potential for the half-cell electrode reaction relates to the activity of the corresponding species according to the Nernst equation:

$$E_a = E_a^\circ + \frac{RT}{nF}\ln\frac{a_{\mathrm{M}^{n+}}}{a_\mathrm{M}} \tag{18}$$

$$E_c = E_c^\circ + \frac{RT}{nF}\ln\frac{a_\mathrm{Ox}}{a_\mathrm{Red}} \tag{19}$$

where E_a° and E_c° are the corresponding standard electrode potentials, V; R is the gas constant, 8.314 J/K/mol; $a_{\mathrm{M}^{n+}}$, a_Ox and a_Red are the activity for the relevant species; a_M can be assumed unity for pure metals.

The standard electrode potential E° can be calculated by the Gibbs free energy of formation of its reactants and products. To calculate the E° of $\mathrm{M}^{n+}/\mathrm{M}$ versus the standard $\mathrm{X}_2/\mathrm{X}^-$ reference (X is F for fluoride salts or Cl for chloride salts), the following two half-cell reactions are considered:

$$\mathrm{M} + n\mathrm{X}^- \leftrightarrow \mathrm{MX}_n + n\mathrm{e}^- \tag{20}$$

$$\frac{n}{2}\mathrm{X}_2 + n\mathrm{e}^- \leftrightarrow n\mathrm{X}^- \tag{21}$$

Combining the half-cell reactions (20) and (21) yields:

$$\mathrm{M} + \frac{n}{2}\mathrm{X}_2 \leftrightarrow \mathrm{MX}_n \tag{22}$$

The Gibbs free energy change per mole of reaction (22) equals to the standard Gibbs free energy of formation of MX_n, i.e., $\Delta G = \Delta G_f^\circ(\mathrm{MX}_n)$. According to Eq. (17), the standard electrode potential for the $\mathrm{M}^{n+}/\mathrm{M}$ electrode reaction can be calculated by:

$$E^\circ_{\mathrm{M}^{n+}/\mathrm{M}}(\text{vs. } \mathrm{X}_2/\mathrm{X}^-) = \Delta G_f^\circ(\mathrm{MX}_n)/nF \tag{23}$$

The value of $\Delta G_f^\circ(\mathrm{MX}_n)$ as a function of temperature can be found from the thermochemical properties tables. In many cases, the melting temperature of pure MX_n is higher than that of the molten salt mixture in which the MX_n is present as liquid. To calculate the Gibbs free energy of these fluorides or chlorides, the supercooled state should be used which is a summation of ΔG_f° at solid state and the Gibbs energy of fusion. The fusion energy can be calculated by the values of enthalpy, entropy, and heat capacity at liquid and solid states [47].

Once the standard electrode potential is known, the redox potential at given activities and temperatures can be calculated according to the Nernst equation. The calculated redox potential of typical $\mathrm{M}^{n+}/\mathrm{M}$ in molten fluoride and chloride salts are displayed as

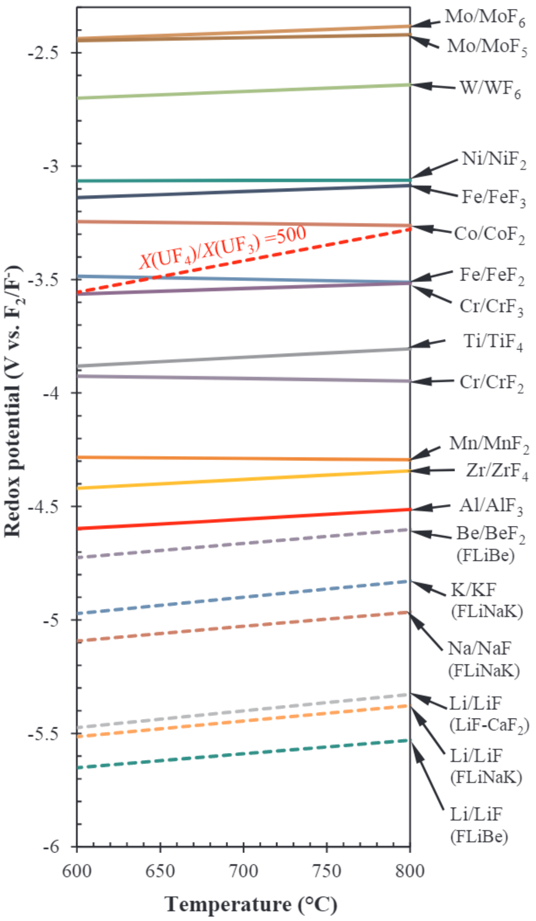

Fig. 1. Redox potentials of various redox couples as a function of temperature in fluoride salts. Solid line: metal dissolution at $a_{M^{n+}}$ of 10^{-6}; Dotted line: reduction of oxidants. Reproduced based on [47].

solid lines in Figs. 1 and 2, respectively. At the solid line, the metal M equilibrates with M^{n+} with an activity of 10^{-6} in the melt. At the potentials below the solid line, the metal is expected to be thermodynamically stable. However, if an oxidant with its reduction potential above the solid line is present in the melt, that is $E_{Ox/Red} > E_{M^{n+}/M}$, the metal will be corroded until the concentration of dissolved M^{n+} elevates to the equilibrium level at which $E_{M^{n+}/M} = E_{Ox/Red}$. The latent oxidants in the nuclear molten salt systems that may cause the corrosion of the metallic structural materials are introduced in the following subsection.

3.2. Oxidants, impurities, and salt purification

3.2.1. Major salt constituents

Metals may be corroded by the reduction of the cations of major salt constituents such as Li(I), K(I), and Be(II). The calculated redox potentials for the reduction of the major salt cations in several molten salts are displayed in Figs. 1 and 2. The activities of the corresponding cations such as Li(I) and Be(II) in FLiBe are calculated by the correlations summarized in Section 2.3. As shown in the plots, the reduction potentials of major salt cations are far below the oxidation potentials of structural metals, which indicates that the cations of alkaline and alkaline earth elements are not expected to cause considerable corrosion of metals. Be(II) and Mg(II) are thermodynamically more oxidizing than other major cations as indicated by their relatively higher reduction potentials in Figs. 1 and 2. The thermodynamically limited concentration of M^{n+} as a result of corrosion of metal by reduction of Be(II) in FLiBe can be calculated by setting $E_{M^{n+}/M} = E_{Be(II)/Be}$. Assuming the activity coefficient of MF_n is 0.01 in the melt, the limited mole fractions of the cations for pure metals in equilibrium with Be(II)/Be in FLiBe at 700 °C are 3×10^{-21} for Ni(II), 9×10^{-17} for Fe(II), 3×10^{-12} for Cr(II), 2×10^{-6} for Al(III), respectively. For alloys, these values are further scaled down by the activities of related elements in the alloy. Therefore, the corrosion of major alloy components (e.g., Ni, Fe, and Cr) by the cations of alkali and alkaline earth elements in molten fluoride and chloride salts is considered negligible.

3.2.2. Actinides and fission products

Actinides dissolved in the molten salts in the form of fluorides or chlorides can act as oxidants to cause metal corrosion depending

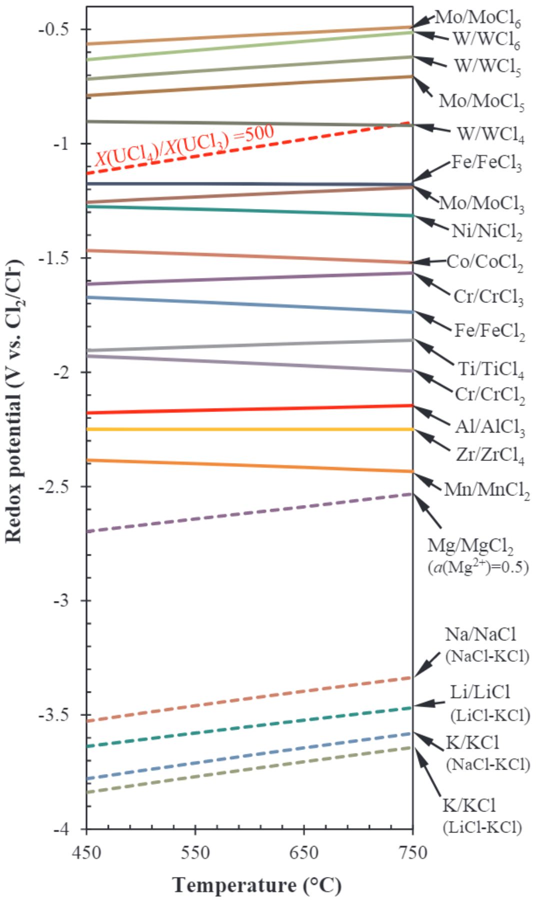

Fig. 2. Redox potentials of various redox couples as a function of temperature in chloride salts. Solid line: metal dissolution at $a_{\mathrm{M}^{n+}}$ of 10^{-6}; Dotted line: reduction of oxidants.

on their reduction potentials. For example, the fuel salt used for MSRE contains 0.13 mol% UF_4 fuel component initially [48]. Structural alloys can be corroded by the reduction of UF_4 to UF_3:

$$\mathrm{U(IV)} + e^- \rightarrow \mathrm{U(III)} \tag{24}$$

The reduction potential of U(IV) depends on the ratio of $a_{\mathrm{U(IV)}}/a_{\mathrm{U(III)}}$. By substituting $a = \gamma X$ in the Nernst equation, the redox potentials of U(IV)/U(III) and the metal dissolution couple $\mathrm{M}^{n+}/\mathrm{M}$ can be correlated with the mole fractions using following equations:

$$E_{\mathrm{U(IV)/U(III)}} = E^{*}_{\mathrm{U(IV)/U(III)}} + \frac{RT}{nF}\ln\frac{X_{\mathrm{U(IV)}}}{X_{\mathrm{U(III)}}} \tag{25}$$

$$E_{\mathrm{M}^{n+}/\mathrm{M}} = E^{*}_{\mathrm{M}^{n+}/\mathrm{M}} + \frac{RT}{nF}\ln\frac{X_{\mathrm{M}^{n+}}}{X_{\mathrm{M}}} \tag{26}$$

where $E^{*}_{\mathrm{U(IV)/U(III)}} = E^{\circ}_{\mathrm{U(IV)/U(III)}} + \frac{RT}{nF}\ln\frac{\gamma_{\mathrm{U(IV)}}}{\gamma_{\mathrm{U(III)}}}$ and $E^{*}_{\mathrm{M}^{n+}/\mathrm{M}} = E^{\circ}_{\mathrm{M}/\mathrm{M}^{n+}} + \frac{RT}{nF}\ln\frac{\gamma_{\mathrm{M}^{n+}}}{\gamma_{\mathrm{M}}}$ are defined as formal potentials.

The formal potentials for redox couples of uranium and other actinides in LiCl-KCl eutectic and FLiBe have been summarized in Refs. [49] and [50], respectively. The correlations for the formal potential as a function of temperature are provided in Table 2. The redox potentials of U(IV)/U(III) for a mole ratio of U(IV)/U(III) at 500 in FLiBe and LiCl-KCl eutectic are plotted in Figs. 1 and 2. It is seen that the reduction potential of U(IV)/U(III) in FLiBe at the more ratio of 500 is more positive than the oxidation potentials of Fe and Cr at 700 °C, indicating U(IV) as an effective oxidant to Fe and Cr under such conditions. Increasing the mole ratio of U(IV)/U(III) will make the salt more oxidizing. It should also be noted that the oxidizing capability of the same species in various molten salts can be quite different due to the difference in formal potential. For example, under the U(IV)/U(III) mole ratio of 500, U(IV) is relatively more oxidizing in molten chlorides compared to fluorides as indicated by the comparisons with oxidation potentials of nickel.

The fission products generated from the nuclear fission may act as oxidants in molten salts. Except for the noble gases and metals, fission products are dissolved in the molten fluoride/chloride salts in the form of fluorides/chlorides or other stable chemical species such as CsI. Tritium fluoride can be produced predominately by irradiation of Li in $LiF\text{-}BeF_2$ salts which is highly corrosive [51]. The

Table 2
Formal potentials of actinides and fission products in molten chlorides and fluorides.

	E^{a} [V vs. Cl_2/Cl^-] in LiCl-KCl	E^{a} [V vs. F_2/F^-] In FLiBe
U(IV)/U(III)	$-1.669 + 2.1 \times 10^{-4}T$ [59]	$-4.766 + 8.51 \times 10^{-4}T$ [50]
U(III)/U	$-2.943 + 5.87 \times 10^{-4}T$ [49]	$-4.955 + 6.74 \times 10^{-4}T$ [50]
Th(IV)/Th	$-2.985 + 5.56 \times 10^{-4}T$ [49]	$-5.413 + 7.64 \times 10^{-4}T$ [60,61]
Pu(III)/Pu	$-3.337 + 7.54 \times 10^{-4}T$ [49]	–
Pa(IV)/Pa	$-2.754 + 6.0 \times 10^{-4}T$ [60]	–
Np(IV)/Np(III)	$-1.250 + 6.64 \times 10^{-4}T$ [62]	–
Np(III)/Np	$-3.230 + 7.19 \times 10^{-4}T$ [49]	–
Y(III)/Y	$-3.603 + 6.88 \times 10^{-4}T$ [49]	–
Zr(IV)/Zr(II)	−2.118 at 723 K [63]	–
Zr(II)/Zr	$-2.298 + 4.12 \times 10^{-4}T$ [49]	–
Zr(IV)/Zr	−2.068 at 723 K [63]	$-4.986 + 7.99 \times 10^{-4}T$ [50]
La(III)/La	$-3.575 + 6.06 \times 10^{-4}T$ [49]	$-5.946 + 8.65 \times 10^{-4}T$ [50]
Ce(III)/Ce	$-3.534 + 5.92 \times 10^{-4}T$ [49]	$-5.872 + 8.61 \times 10^{-4}T$ [50]
Pr(III)/Pr	$-3.541 + 6.30 \times 10^{-4}T$ [49]	–
Nd(III)/Nd	$-3.567 + 6.28 \times 10^{-4}T$ [49]	–
Sm(III)/Sm(II)	$-2.618 + 7.76 \times 10^{-4}T$ [49]	~ −3.5 at 812 K [57]
Sm(II)/Sm	–	< Be(II)/Be [57]
Eu(III)/Eu(II)	$-1.356 + 7.2 \times 10^{-4}T$ [49]	$-4.741 + 1.040 \times 10^{-3}T$ [47][a]
Gd(III)/Gd	$-3.514 + 7.32 \times 10^{-4}T$ [64]	–

[a] Formal potentials obtained in FLiNaK salt.

gaseous fluorine/chlorine is also generated during the nuclear fission [17] which are very oxidizing as indicated by the standard potentials in Figs. 1 and 2. Lanthanides are typically dissolved in the form of trifluorides/trichlorides in the melt while some of them (e.g., europium, samarium, and neodymium) can also present as difluorides/dichlorides. Zr may exist in the melt at the oxidation states of +IV and/or +II. The reduction of lanthanides and Zr from the higher oxidation states to more negative ones may cause corrosion of metals. The formal potentials of these fission products in molten LiCl-KCl salt have been extensively investigated due to the motivation for electrorefining the spent metallic fuels. The data have been analyzed previously by Zhang [49], and the recommended correlations are summarized in Table 2. The correlations for the temperature dependence of formal potentials of La(III)/La, Ce(III)/Ce, and Zr(IV)/Zr in FLiBe are also included in Table 2 which are based on the early work done for MSRE [50]. While for other molten fluoride and chloride salts, the data on formal potentials for fission products are still scarce. In recent years, the electrochemical behaviors of many lanthanides have been investigated in molten LiF-CaF_2 [22,52–55], FLiBe [56,57], and FLiNaK [47,58]. However, for most of them, only rough estimations of the formal potentials can be derived as the potentials were measured against a platinum quasi-reference electrode whose potential is sensitive to the O^{2-} impurity level in the melt. The results show the reduction potentials of Gd(III) and Nd(III) are very close to that of Li(I), while formal potentials of Eu(III)/Eu(II) and Sm(III)/Sm(II) are about 0.8–1.3 V more positive than the reduction potential of Be(II), Li(I), or K(I) in the fluoride salts. According to these findings and formal potentials calculated from Table 2, the cations such as U(IV), Np(IV), Zr(IV), Sm(III), and Eu(III) are thermodynamically more oxidizing than other elements.

While it does not contribute to metal dissolution, some fission products such as tellurium cause intergranular cracking (IGC) in Ni-based alloys. Te is in the same group with O and S and may act as an oxidant against metals [65]. Te-induced IGC is caused by the preferential diffusion of Te along the grain boundaries and subsequent formation of brittle intermetallic compounds and corrosion products [17,66,67].

3.2.3. Structural metal impurities

The structural metal impurities may arise from the starting materials, the corrosion of structural components in MSRs and EChem salt containers, and from the salt preparation and processing facilities. The dissolved Ni(II), Fe(III), Fe(II), and Cr(III) cations in the molten salt are potential oxidants that may cause the corrosion of metals [68–70]. Although the redox potential depends on the concentrations, the cation of a less noble element is typically nonoxidizing to relatively inert alloying elements. For example, the formal potentials of Ni(II)/Ni, Fe(II)/Fe, and Cr(II)/Cr in FLiBe at 700 °C are −2.42 V, −2.90 V, and −3.28 V versus F_2/F^-, respectively [50]. To oxidize Fe and Ni metals, the concentration of Cr(II) in the salt must be about four orders of magnitude larger than Fe(II) concentration and nine orders of magnitude larger than Ni(II) concentration, respectively. Such conditions are uncommon in practice. Hence, Ni(II) and Fe(II) typically are oxidants to cause Cr dissolution. Fe and Cr are also stable at trivalence state in fluoride and chloride melts. The redox potentials of Fe(III)/Fe(II) and Cr(III)/Cr(II) depend on the concentration ratios according to the Nernst equation. Thermodynamic calculations indicate that even small amounts of Cr(III) and Fe(III) are oxidizing to Cr, Fe, and Ni metals. For the equilibrium with M(II)/M at a M(II) fraction of 10^{-4}, the calculated concentration ratio of Cr(III)/Cr(II) are $\sim 2 \times 10^{-5}$ for Cr(II)/Cr, $\sim 2 \times 10^{-3}$ for Fe(II)/Fe, and 0.5 for Ni(II)/Ni, respectively. This means that metals can be oxidized by Cr(III) in FLiBe as long as the ratio of Cr(III)/Cr(II) is above the critical value, i.e., 0.5 for corrosion of Ni.

On the other hand, reduction rates of these structural-metal impurities not only depend on the overpotential but also their concentrations considering the concentration dependence of exchange current density and mass transfer rate. Therefore, if the amounts of these metallic impurities are small, the resulted corrosion might be smaller than that caused by other major oxidants such as U(IV) in fuel salts.

3.2.4. Water contaminant

One of the most common contaminants is moisture which is perhaps the most deleterious impurity in molten fluoride and chloride salts as it reacts with fluorine or chlorine ions in the melt to form oxide impurities and highly corrosive hydrofluoric or hydrochloric acid:

$$H_2O(g) + 2F^- \leftrightarrow O^{2-} + 2HF(g) \tag{27}$$

$$H_2O(g) + 2Cl^- \leftrightarrow O^{2-} + 2HCl(g) \tag{28}$$

The generation of HF by the reaction of water with fluoride salt is thermodynamically more favorable than HCl in chloride salt due to the more negative $\Delta G_f^\circ(\mathrm{HF})$ than $\Delta G_f^\circ(\mathrm{HCl})$ [71]. This is evidenced by the equilibrium constants $\frac{P_{HX}^2 [O^{2-} \text{in mol / kg}]}{P_{H_2O}}$ determined in several molten fluoride and chloride salts. Some examples of the reported values are $10^{-4.15}$ in FLiBe melt at 600 °C [61], $10^{-14.0}$ in NaCl-KCl eutectic at 727 °C [72], and $10^{-16.23}$ in LiCl-KCl eutectic at 450 °C [73], respectively.

The gaseous HF or HCl is dissolved and strongly retained in the molten fluorides or chlorides. The solubilities of HF and HCl obey Henry's law, where the temperature dependence of the Henry's law constants for HF in FLiBe and HCl in LiCl-KCl eutectic can be expressed by the following correlations [74,75]:

$$\log K_{HF} = -6.496 + 1399.3/T \tag{29}$$

$$\log K_{HCl} = -5.094 - 631.1/T \tag{30}$$

where K_{HF} and K_{HCl} are the Henry's law constants, mol/cm^3/atm; T is temperature, K.

Hydrofluoric acid is a weak acid although it is very corrosive. In molten fluoride salts, HF is strongly associated with F^- to form HF_2^- rather than dissociating to H^+ and F^- [76,77]. The hydrogen evolution of HF in molten fluorides proceeds by the direct reduction of HF, as evidenced by the polarization measurements [76]:

$$HF + e^- \rightarrow \frac{1}{2}H_2 + F^- \tag{31}$$

To account for the observed Tafel slope and limiting currents, a reaction mechanism for HF reduction was proposed by Pizzini et al. [76,78] in which the rate-determining step (RDS) is the slow chemical reaction:

$$HF_2^- \rightarrow HF + F^- \tag{32}$$

In the presence of water, the second hydrogen evolution reaction in addition to the HF reduction was identified which was attributed to the direct reduction of H_2O [76]:

$$H_2O + e^- \rightarrow \frac{1}{2}H_2 + OH^- \tag{33}$$

or the reduction of H_3O^+ which may become non-negligible for higher amount of water [77,78]:

$$H_2O + HF \leftrightarrow H_3O^+ + F^- \tag{34}$$

$$H_3O^+ + e^- \rightarrow \frac{1}{2}H_2 + H_2O \tag{35}$$

Compared to the reduction rate of HF, the reduction of H_2O or H_3O^+ only becomes pronounced at more negative overpotentials or beyond the limiting current of HF reduction.

HCl is assumed to be fully dissociated in molten chloride salts as Cl^- is an exceedingly weak conjugate base. Thus, the hydrogen evolution reaction of HCl is by the reduction of the dissociated H^+ as identified by the voltammetric measurement in molten LiCl-KCl eutectic containing anhydrous hydrogen chloride [79].

$$H^+ + e^- \rightarrow \frac{1}{2}H_2 \tag{36}$$

With the presence of water, a bi-electrode behavior representing the simultaneous reduction of H^+ and H_2O occurs. For the chloride melt containing large amount of water and oxide impurities, higher concentration of OH^- is expected in which case the hydrogen evolution can also proceed by the reduction of OH^- [79]:

$$H_2O + O^{2-} \rightarrow 2OH^- \tag{37}$$

$$OH^- + e^- \rightarrow \frac{1}{2}H_2 + O^{2-} \tag{38}$$

It is acknowledged that the corrosion rate of metals in acidic aqueous solution increases with the decrease in pH primarily due to the accelerated cathodic reduction rate of dissociated H^+ [80]. Similarly, the increase of the amount of water and HF/HCl in the melt may cause the increase of the reduction rates of water and HF/HCl on the metal surface. On the other side, water and acids may also influence the anodic metal dissolution reactions in molten halide salts. It is well accepted that the anodic metal dissolution in aqueous solution is accelerated by OH^- ions by the intermediate formation of hydroxylated metal compound. A well-known mechanism proposed for iron dissolution reaction in acidic aqueous solutions follows the path of: $Fe + OH^- \leftrightarrow FeOH + e^-$; $FeOH\underset{\rightarrow}{RDS}FeOH^+ + e^-$; $FeOH^+ \leftrightarrow Fe^{2+} + OH^-$ [80]. Later in Section 4.2.1, we will see the experimental evidence of the accelerated anodic metal dissolution rate due to water additions in molten salts. Hence, the metal dissolution mechanism in aqueous solutions might still be applicable for the molten fluoride and chloride salts that contain sufficient amount of water or/and OH^-. However, the mechanism of metal dissolution in dehydrated molten salts may be more important which is unclear so far.

3.2.5. Oxide impurities

The oxide impurities in molten salts are present as O^{2-} which can be introduced by the oxygen and water contaminations. Although O^{2-} is not oxidizing towards metals, it can still influence the corrosion of structural materials because of the formation of oxide corrosion products:

$$M + \frac{n}{2}O^{2-} \leftrightarrow MO_{\frac{n}{2}} + ne^- \tag{39}$$

The standard electrode potential of reaction (39) can be calculated by:

$$E^\circ_{M/MO_{\frac{n}{2}}}(\text{vs. } X_2/X^-) = -\frac{\Delta G^\circ_f\left(MO_{\frac{n}{2}}\right) - \frac{n}{2}\Delta G^\circ_f(O^{2-})}{nF} \tag{40}$$

Assuming that the salt is an ideal mixture and the system is isothermal with a constant vapor pressure, the standard Gibbs free energy of O^{2-} in the salt such as LiCl-KCl can be evaluated by [81]:

$$\Delta G^\circ_f(O^{2-})_{LiCl-KCl} = X_{LiCl}\Delta G^\circ_f(O^{2-})_{LiCl} + X_{KCl}\Delta G^\circ_f(O^{2-})_{KCl} \tag{41}$$

where $\Delta G^\circ_f(O^{2-})_{LiCl} = \Delta G^\circ_f(Li_2O) - 2\Delta G^\circ_f(LiCl)$ and $\Delta G^\circ_f(O^{2-})_{KCl} = \Delta G^\circ_f(K_2O) - 2\Delta G^\circ_f(KCl)$ are the standard free energy in pure LiCl and KCl salt, respectively.

The formed oxide corrosion product $MO_{\frac{n}{2}}$ might be dissolved in the fluoride or chloride salt:

$$MO_{\frac{n}{2}} + nX^- \leftrightarrow MX_n + \frac{n}{2}O^{2-} \tag{42}$$

The equilibrium constant of reaction (42) can be calculated from the standard Gibbs free energy change of reaction:

$$\Delta G = -RT\ln K \tag{43}$$

where $K = \frac{a_{MX_n} a_{O^{2-}}^{n/2}}{a_{X^-}^{n}}$.

For a given activity of MX_n, the equilibrium potentials of related electrochemical reactions can be calculated as a function of $a_{O^{2-}}$ according to Eqs. (23) and (40) while the equilibrium of the chemical dissolution of $MO_{\frac{n}{2}}$ can be calculated by Eq. (43). The calculated equilibrium lines for Ni, Fe and Cr in FLiBe at 700° are plotted in the E-pO^{2-} diagrams (Fig. 3). The E-pO^{2-} diagram indicates the stability domains of a metal, of its fluorides and its oxides as function of potential and pO^{2-} ($pO^{2-} = -\log_{10}a_{O^{2-}}$). The lines for the MF_n domain in Fig. 3 represent the dissolved M^{n+} equilibrates with the metal M or $MO_{\frac{n}{2}}$ at a M^{n+} activity of 10^{-6}. The figure shows that Ni is immune to corrosion at more positive potential than Fe and Cr. Cr has a wider oxide formation window than Ni which means the Cr_2O_3 can be formed at relatively lower O^{2-} concentration (i.e., higher pO^{2-}) than NiO. Although Cr_2O_3 are thermodynamically more stable, formation of a dense and protective oxide layer is typically unrealistic in molten fluorides and chlorides as indicated by the experimental results in Sections 4 and 5. Hence, rather than relying on the oxide layer, the structural alloys exposed to molten fluoride and chloride salts need to be thermodynamically stable. Therefore, the redox potential of the salt needs to be controlled in the metal stability domain to prevent metal corrosion which leads to the development of redox control techniques (see Section 6).

3.2.6. Salt purification

The halide salts provided by most of the suppliers cannot be used directly due to the residual impurities [18]. The residual moisture and metallic impurities must be removed to prevent the severe corrosion of materials in molten fluoride and chloride salts. The O^{2-} impurity also needs to be reduced to avoid the formation of metallic oxides especially UO_2 [17]. Many methods to remove these impurities in molten fluoride and chloride salts have been applied, including thermal treatment under flowing Ar gas or vacuum condition, dry HF or HCl gas sparging, solid ammonium hydrofluoride, carbochlorination by CCl_4 vapor, contacting with a reductive metal, and electrochemical separation.

The majority of the water contamination in the salt can be removed by thermal treatment under flowing Ar gas or vacuum condition. It is recommended to heat the salt to the temperatures above its operation temperature in a stepwise manner to minimize the oxide impurities generated by the accelerated reaction of residual water with salt during the heating process.

The removal of the oxide impurities in the salt can be performed by bubbling gaseous HF or HCl into the fluoride or chloride molten salts. The reverse of reactions (27) and (28) indicates that HF or HCl reacts with the oxides to form fluorine or chlorine ions and water vapor. The generated water vapor can be swept out by the following Ar sparging in the melt. ORNL experience showed that the O^{2-} impurity concentration could be reduced to less than 200 wppm (i.e., 10^{-2} mol oxygen per kilogram salt) by HF/H_2 (ratio ≈ 1) sparging [82]. Use of a mixture of HF/H_2 or $HF/H_2/Ar$ instead of pure HF is recommended as H_2 makes the salt less oxidizing. It was found that the amount of sulfur contaminants in the FLiBe was also reduced by the HF/H_2 sparging [82].

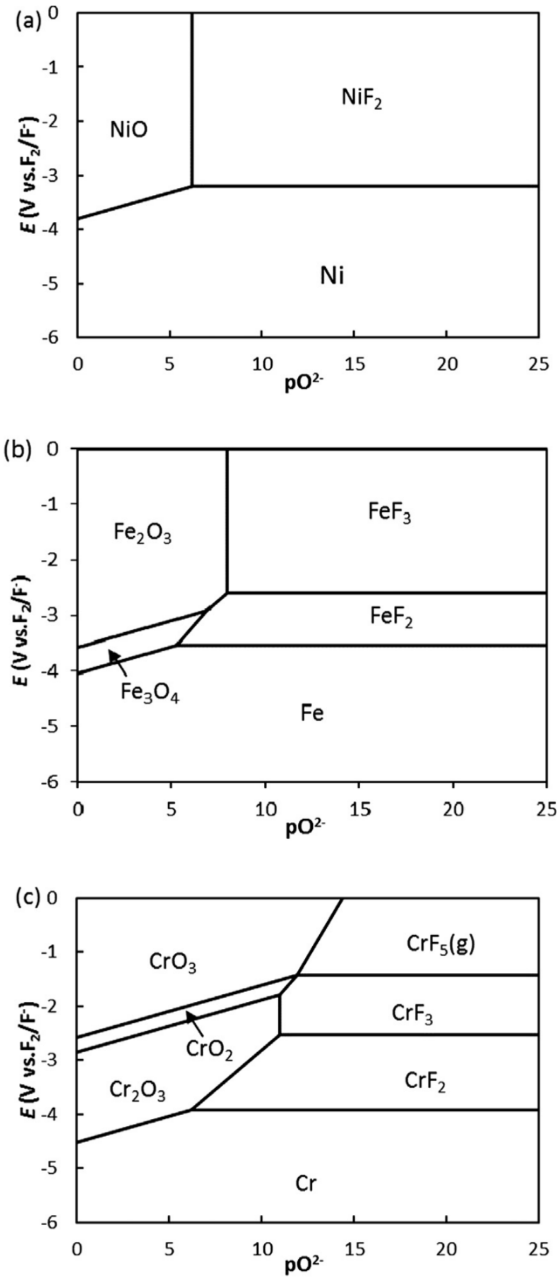

Fig. 3. E-pO^{2-} diagrams calculated at 700 °C for Ni, Fe, and Cr in FLiBe. a_{MF_n} of 10^{-6} is used for the calculation of related equilibrium lines.

For the removal of oxides in molten chlorides, it was claimed that HCl sparging was not effective and the remaining oxygen content in the molten chlorides could be up to a few weight percent [18]. However, the removal of oxides in chloride melt by HCl sparging should be more thermodynamically favorable as the equilibrium constant of HCl sparging reaction (27) is several orders of magnitude larger than that of HF sparging reaction (28). Laboratory experiments at 450 °C showed that the O^{2-} concentration in molten LiCl-KCl eutectic was rapidly reduced to about $10^{-12.3}$ mol/kg during the HCl bubbling and maintained at 10^{-6} mol/kg during the following argon bubbling process [73]. The rising of O^{2-} concentration during Ar bubbling might be due to the remaining water vapor after HCl sparging. Nevertheless, the final O^{2-} concentration is still about four orders of magnitude lower than that after HF sparging in fluoride salts. The carbochlorination by bubbling the carbon tetrachloride (CCl_4) vapor through the chloride salt is an alternative method to remove the oxide impurity:

$$CCl_4(g) + 2O^{2-} \rightarrow CO_2(g) + 4Cl^- \tag{44}$$

$$CCl_4(g) + O^{2-} \rightarrow COCl_2(g) + 2Cl^- \tag{45}$$

The experimental results showed that the purification 'threshold' of carbochlorination in LiCl-KCl at 700–800 °C was about 2×10^{-4} mol O^{2-} per kilogram of the melt [83]. It seems less effective than HCl sparging, but the O^{2-} concentration is still low compared to the HF sparging in fluoride salts.

Solid ammonium bifluoride NH_4HF_2 was also recommended to remove the metallic oxide impurities in fluoride salts [84]. NH_4HF_2 is safer and more convenient in use than the gaseous HF. Heating the mixture of solid ammonium bifluoride and fluoride salts will result in the conversion of oxides to fluorides, accompanied with the release of NH_4F gas and water vapor, as described by reaction (46). Further purification can be performed by zone melting and filtration of the melts through a nickel filter [84].

$$2NH_4HF_2 + O^{2-} \rightarrow 2NH_4F(g) + H_2O(g) + 2F^- \tag{46}$$

The metallic impurities and other oxidizing impurities such as remaining HF and water moisture after HF sparging can be reduced by contacting the salt with reductive metals. The reductive metals corresponding the major salt constituents such as beryllium in BeF_2-based salt [82] and magnesium in $MgCl_2$-based salt [85] are recommended to avoid the ingress of any additional impurities. An alternative option is to electrodeposit the oxidizing metallic impurities on the cathode. It is also possible to remove the water and oxide impurities using electrochemical separation techniques. Purification results in molten FLiNaK showed that the water contamination in the melt was reduced from 169,000 wppm to 42.6 wppm by applying a potential of 2.35 V between the cathode and anode electrodes [86]. During this process, hydrogen gas was generated on the cathode due to the reduction of H_2O and OH^- while O^{2-} and OH^- were oxidized to oxygen gas on the anode. When graphite anode is used, CO or/and CO_2 are produced instead:

$$C + O^{2-} \rightarrow CO(g) + 2e^- \tag{47}$$

$$C + 2O^{2-} \rightarrow CO_2(g) + 4e^- \tag{48}$$

3.3. Electrochemical kinetics of alloy corrosion

The rate for an electrode reaction can be represented by the current density according to the Faraday's law. According to the mixed potential theory [87], corrosion occurs at the corrosion potential E_{corr} where the net current for all electrode reactions on the metal surface is zero. At this potential, the electrode reactions for both metal oxidation and oxidant reduction are driven by the potential differences between the corrosion potential and their corresponding equilibrium potentials. With the assumption of no mass-transfer effect, the relation of current density and potential for an electrode reaction is characterized by the Butler-Volmer equation [88]:

$$i = i_0\left\{\exp\left[\frac{(1-\alpha)nF}{RT}\eta\right]-\exp\left(-\frac{\alpha nF}{RT}\eta\right)\right\} \tag{49}$$

where i is current density, A/cm^2; i_0 is the exchange current density, A/cm^2; α is the charge transfer coefficient; overpential $\eta = E-E^{\mathrm{eq}}$; E and E^{eq} are the electrode potential and the equilibrium potential respectively, V.

At the corrosion potential, the rates of the reverse reactions for both the metal dissolution and oxidant reduction are typically negligible. This leads to the elimination of the second exponential term in Eq. (49) for metal dissolution as well as the first exponential term for the reduction of oxidants. The reduction rate of an oxidant can be limited by its mass-transfer rate from the bulk solution to the metal surface, i.e., the oxidant in the solution adjacent to the metal surface is depleted by the faster charge-transfer rate. In such situation, the cathodic current density i_{c} representing the reduction rate of oxidant can be expressed as:

$$i_{\mathrm{c}} = -i_{\mathrm{c}0}\frac{c_{\mathrm{Ox}}^{\mathrm{s}}}{c_{\mathrm{Ox}}^{\mathrm{b}}}\exp\left(-\frac{\alpha_{\mathrm{c}}nF}{RT}\eta_{\mathrm{c}}\right) \tag{50}$$

where c^{s} and c^{b} represent the concentration on the electrode surface and in bulk solution respectively, mol/cm^3.

By considering $i_{\mathrm{c}} = nFk_{\mathrm{m}}(c_{\mathrm{Ox}}^{\mathrm{b}}-c_{\mathrm{Ox}}^{\mathrm{s}})$ and the definition of the limiting current density $i_{\mathrm{L}}^{\mathrm{Ox}} = nFk_{\mathrm{m}}c_{\mathrm{Ox}}^{\mathrm{b}}$, the concentration ratio can be correlated with the limiting current density:

$$\frac{c_{\mathrm{Ox}}^{\mathrm{s}}}{c_{\mathrm{Ox}}^{\mathrm{b}}} = \frac{i_{\mathrm{L}}^{\mathrm{Ox}}-i_{\mathrm{c}}}{i_{\mathrm{L}}^{\mathrm{Ox}}} \tag{51}$$

Insertion of Eq. (51) in Eq. (50) derives the following expression for the reduction rate of oxidant when the mass-transfer effect is involved:

$$i_{\mathrm{c}} = -\frac{i_0\exp\left(-\frac{\alpha nF}{RT}\eta\right)}{1-\frac{i_0}{i_L^{\mathrm{Ox}}}\exp\left(-\frac{\alpha nF}{RT}\eta\right)} \tag{52}$$

Rather than the homogeneous dissolution, the structural alloys in molten fluorides and chlorides typically suffered from the selective dissolution of the less noble element Cr, as observed from the experimental results. This can be interpreted by the schematic simulation of corrosion of alloys in molten fluoride salts at 700 °C as shown in Fig. 4. Three model alloys 71Fe-17Cr-12Ni, 73Ni-17Cr-10Fe, and 71Ni-16Mo-7Cr-5Fe that have similar contents of major alloying elements as stainless steel 316L, Inconel 600, and Hastelloy N were chosen. The current-potential curves for the electrode reactions were calculated by Eqs. (49) and (52). In the

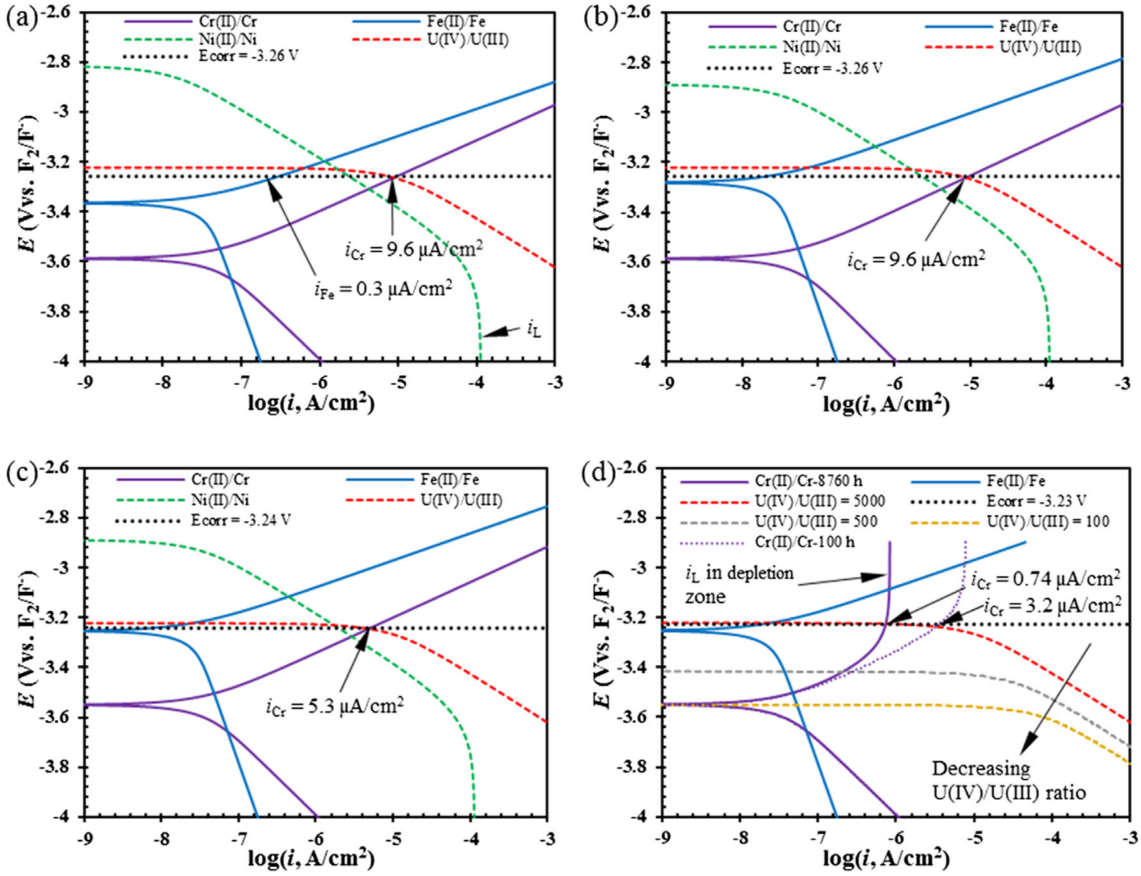

Fig. 4. Schematic polarization curves for alloy corrosion in molten fluoride salts at 700 °C (a) 71Fe-17Cr-12Ni alloy, (b) 73Ni-17Cr-10Fe alloy, (c) 71Ni-16Mo-7Cr-5Fe alloy, (d) 71Ni-16Mo-7Cr-5Fe alloy after 1 year of Cr selective dissolution.

simulation, the equilibrium potentials of Cr(II)/Cr, Fe(II)/Fe, and Ni(II)/Ni on the alloys were calculated based on the formal potential values reported in FLiBe [50] and mole fractions of 10^{-4} for Cr(II) and 10^{-5} for Fe(II) and Ni(II) cations in the molten salt. By considering the correlation $i_0 = nFk^0 {C^{\mathrm{b}}_{\mathrm{M(n)}}}^{1-\alpha} X_{\mathrm{M}}^{\alpha}$ [88], the exchange current densities of Cr(II)/Cr and Fe(II)/Fe at the simulated cation fractions were calculated by the reaction rate constant k^0 derived from the i_0 and α values measured in FLiNaK [89]. The value of k^0 for Ni(II)/Ni was assumed equal to Fe(II)/Fe and an α value of 0.5 was used. The dissolution of molybdenum was considered negligible. The reduction kinetics of an intrinsic oxidant U(IV) redox in the fuel salt was simulated at a U(IV)/U(III) concentration ratio of 5000 with a total uranium concentration of 0.13 mol%. The current-potential curve was then calculated based on the formal potential of U(IV)/U(III) given in Table 2, and the assumptions of $\alpha = 0.5$ and $k^0 = 10^{-3}$ cm/s as estimated in molten chloride salts [90]. The reduction kinetics of U(IV) was assumed to be the same on the three model alloys, which in fact may vary with the materials and the surface conditions. The oxidation kinetics of U(III) and Ni(II) were not plotted in Fig. 4 as they act as oxidants. The maximum transfer rates of metal cations to alloy surface, i.e., the limiting current densities i_{L}, at simulated flow velocity of 3 m/s and 0.1 m pipe diameter were calculated by Eq. (1) using the physical properties of FLiBe summarized in Table 1 and the reported diffusion coefficients for related cations [91–93].

The corrosion potentials at zero net current are indicated by the horizontal lines in Fig. 4. As shown in Fig. 4a–c, the corrosion of three model alloys in the simulated condition are predominated by the dissolution of Cr. Negligible corrosion of iron is expected for the two modeled Ni-based alloys. Iron dissolution is observed for modeled Fe-based alloy (Fig. 4a) but remains nearly two orders of magnitude smaller than the chromium dissolution rate. Fe-based alloy 71Fe-17Cr-12Ni and Ni-based alloy 73Ni-17Cr-10Fe with same Cr content show similar Cr dissolution rate of ~9.6 μA/cm^2, while for lower Cr content alloy 71Ni-16Mo-7Cr-5Fe it is decreased by 45%. It seems that the corrosion resistance of alloy is primarily determined by the content of the least noble element Cr in the alloy rather than the base metal at simulated redox conditions. However, if significant amounts of oxidizing impurities such as water, HF, or Ni ions presents in the salt, iron content may become important as well because corrosion of alloys may occur at higher potentials where rate of iron dissolution will approach chromium dissolution. In this simulation, the nickel ion concentration is very low (10^{-5} mole fraction) and its exchange current density is much smaller compared to U(IV)/U(III). Hence, the contribution of Ni(II) reduction to Cr dissolution is much less than the reduction of U(IV) although Ni(II) is thermodynamically more oxidizing.

As the corrosion of alloy is predominated by the selective dissolution of Cr, the depletion of Cr in the alloy region near the alloy/molten salt interface is expected. The Cr depletion zone in the alloy will grow deeper with time by the outward diffusion of Cr. The increase of Cr depletion layer thickness will result in the lower diffusion rate of Cr from the alloy matrix to the alloy/molten interface, thus limiting the Cr dissolution rate. Similar to the diffusion of ions in the molten salt, the limiting current density representing the maximum diffusion rate of Cr in the alloy matrix can be defined by [94]:

$$i_{\mathrm{L}}^{\mathrm{M}} = nFc_{\mathrm{b}}^{\mathrm{M}}D_{\mathrm{eff}}^{\mathrm{M}}/\delta_{\mathrm{M}} \tag{53}$$

where $i_{\mathrm{L}}^{\mathrm{M}}$ is the maximum diffusion current density of M in the alloy, A/cm^2; $c_{\mathrm{b}}^{\mathrm{M}}$ is the concentration of M in the bulk alloy, mol/cm^3; δ_{M} is the diffusion length, cm; $D_{\mathrm{eff}}^{\mathrm{M}} = D_{\mathrm{tra}}^{\mathrm{M}}(1-f) + D_{\mathrm{int}}^{\mathrm{M}}f$ [95] is the effective diffusion coefficient of M in the alloy, cm^2/s; $D_{\mathrm{tra}}^{\mathrm{M}}$ and $D_{\mathrm{int}}^{\mathrm{M}}$ are the transgranular and intergranular diffusion coefficients respectively; and f represents the fraction of diffusion sites in the grain boundaries.

The effective diffusion coefficient strongly depends on the grain size. As $D_{\mathrm{int}}^{\mathrm{M}}$ is normally 10^4–10^6 times higher than $D_{\mathrm{tra}}^{\mathrm{M}}$ [95], the effective diffusion coefficient can be lowered by increasing the size of grain, i.e., minimizing the grain boundaries [95,96]. The estimated effective diffusion coefficient of Cr in the Hastelloy N is 2.51×10^{-15} cm^2/s [97] or 8.72×10^{-15} cm^2/s [98] at 700 °C. The value for Fe in Hastelloy N is about double of Cr, i.e., 5.56×10^{-12} cm^2/s for Fe diffusion compared to 2.81×10^{-12} cm^2/s for Cr at 850 °C [99]. The value of 2.51×10^{-15} cm^2/s for Cr diffusion will be used for 71Ni-16Mo-7Cr-5Fe model alloy in the later simulation.

The diffusion length in Eq. (53) can be conservatively estimated by $D_{\mathrm{eff}}^{\mathrm{M}}$ and time t[96,97]:

$$\delta_{\mathrm{M}} = \sqrt{D_{\mathrm{eff}}^{\mathrm{M}}t} \tag{54}$$

Then the anodic dissolution rate of the less noble metal alloy element considering the diffusion through the depletion zone can be obtained:

$$i_{\mathrm{a}} = \frac{i_0\exp\left[\frac{(1-\alpha)nF}{RT}(E-E^{eq})\right]}{1+\frac{i_0}{i_L^M}\exp\left[\frac{(1-\alpha)nF}{RT}(E-E^{eq})\right]} \tag{55}$$

Fig. 4d shows the simulated corrosion kinetics of 88Ni-7Cr-5Fe with a Cr depletion zone at 700 °C. The limiting current density for Cr diffusion through the depletion zone was calculated according to Eqs. (53) and (54) at two exposure durations. As shown in Fig. 4d, the limiting current density decreased with time, significantly slowing down the Cr dissolution rate at 8760 h (i.e., one year). The initial Ni(II) impurity in the salt should be exhausted and was not considered at 8760 h. The indicated Cr corrosion current density after one year was decreased by seven times compared to its initial condition without depletion zone (Fig. 4c). This is attributed to the Cr depletion effect which can also be understood by considering the following equation for selective dissolution of alloying element $i = nFk_0\exp\left[X_{\mathrm{Cr}}^{\mathrm{s}}\frac{(1-\alpha)nF}{RT}(E-E^{*})\right]$ [88]. It is obvious that the Cr depletion decreases the Cr atoms on the alloy surface $X_{\mathrm{Cr}}^{\mathrm{s}}$, resulting in the decrease of Cr dissolution rate. It should be mentioned that the metal dissolution is normally predominated by the dissolution of kink atoms as their removal requires much less activation energy than terrace atoms. However, the dissolution of atoms from terrace sites may become considerable when the dissolution rate of kink atoms is limited by the diffusion rate through the depletion zone [100]. The other reason that can further decrease the corrosion rate is the decrease of U(IV)/U(III) concentration ratio with time due to consumption of U(IV) ions. As shown in Fig. 4d, the dissolution of Cr in the alloy will be decreased with the decrease of U(IV)/U(III) concentration ratio. At U(IV)/U(III) ratio below 100, the redox potential of U(IV)/U(III) will be balanced with Cr(II)/Cr, indicating the termination of corrosion. However, if the dissolved Cr(II) is continually deposited at cold sections of the coolant loop, thermal gradient-driven corrosion will occur at hot sections. Regardless of the simplification of the above corrosion simulation, the predictions indicate an initial corrosion rates of ~50–110 μm/year which are in the same order of magnitude with the test results of 300 series stainless steels and Inconel alloys in fluoride fuel salts with initial U(IV)/U(III) concentration ratio of $\sim 5 \times 10^3$–10^4 [101,102]. The corrosion rates of Hastelloy N determined from ORNL's loop tests were about 0.5–2.2 μm/year in the time scale of 10^3–10^4 h [101,102], which are lower than the predicted value (~8 μm/year) in Fig. 4d. This might be due to the decrease of U(IV)/U(III) concentration ratio with time in the loop tests. The simulation of corrosion in molten chloride salt is more difficult compared to molten fluoride corrosion since porous oxide layers are typically formed in chloride salts. Although these oxide layers are not passivating, it may still provide some protection to the metal underneath. The resistance of the oxide layer is strongly dependent on the environmental and metallurgical factors which are discussed in Section 5.

4. Materials corrosion in molten fluoride salts

Many MSR concepts use molten fluorides as the fuel and/or coolant salts. Considering the operating lifetime of a reactor (30–50 years), the metallic material used to construct the primary circuit of an MSR must be compatible with the fluoride fuel/coolant salts at high temperatures. The structural materials used for MSR structural components should exhibit good mechanical properties under irradiation, sufficient resistance to the oxidation of the air outside the loop at high temperatures, and good fabrication capabilities. Among various proposed fluoride fuel salts, the compatibility of materials have been most thoroughly studied for LiF-BeF$_2$-based fuel salts. The FLiBe and FLiNaK salts have also been extensively studied as they are the promising coolant candidates for MSRs. Both FLiBe and FLiNaK are also proposed as blanket coolants and tritium breeding materials for fusion reactors in which the container materials are exposed to higher concentrations of the corrosive tritium fluoride than fission reactors [86,103,104]. The studies related to the compatibility of materials with LiF-CaF$_2$ salt is scarce and only limited data can be found from the aerospace field [105] where the LiF-CaF$_2$ salt was selected as the thermal storage material for the solar dynamic space power system in the

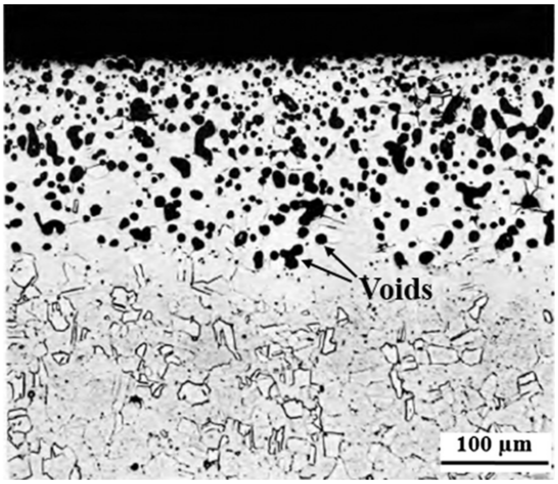

Fig. 5. Typical photomicrograph of Inconel 600 after exposure to molten fluorides [113].

satellite.

4.1. *Historical development of corrosion resistant alloys*

Selection of appropriate structural materials for MSRs dates back to the late 1940s when the first MSR concept was proposed in the United States for aircraft propulsion [106]. Numerous corrosion tests were performed to screen the existing alloys that were compatible with the molten fluorides during the Aircraft Nuclear Propulsion (ANP) program at ORNL. The pure metals made of Mo and Ni showed outstanding corrosion resistance but were eliminated due to the poor physical properties and fabrication difficulties. Of the existing alloys, only the corrosion resistance of Hastelloy B (Ni-28Mo-5Fe) and Hastelloy W (Ni-25Mo-5Cr-5Fe) was satisfactory in molten fluorides [107,108]. However, both cannot be used as structural materials for MSRs as they age at the MSR operating temperatures and become brittle due to the formation of Ni-Mo intermetallic compounds [109]. In consideration of the corrosion resistance, mechanical properties, and the fabrication capability, Inconel 600 (Ni-15Cr-7Fe) was selected as the structural material for the Aircraft Reactor Experiment (ARE) which was a 2.5 MW reactor with $NaF\text{-}ZrF_4\text{-}UF_4$ as the fuel salt. The ARE operated successfully for nine days in 1954 at salt temperatures approaching 900 °C without any mechanical or chemical problems [110]. However, the postoperative examination of the ARE structural components showed a depth of corrosion attack up to ~100 µm [111], indicating the corrosion resistance of Inconel 600 might be inadequate at the design temperature for long-term use.

The evolution of corrosion with time was observed from the Inconel 600 flow loop tests. Most tests were operated at about 870 °C which showed corrosion depths of ~120–180 µm at 1000 h, ~350 µm at 3000 h, and ~630 µm at 8300 h, respectively [112]. The typical attack of Inconel 600 in molten fluorides is illustrated in Fig. 5 [113]. The attack was attributed to the selective dissolution of Cr as indicated by the depletion of Cr in the corrosion attack layer. The outward diffusion of Cr from the alloy was by vacancy exchange mechanism during which voids could be formed by the precipitation of the excess vacancies in grain boundaries and inclusions in the grain matrix [113]. The corrosion mechanism of Ni-Mo alloys containing less Cr and Fe followed the same pattern as Inconel 600, but the corrosion depth of these alloys was less than 50 µm [112]. The superior corrosion resistance of Ni-Mo alloys led to the development of Hastelloy N during the ANP program [112]. Compared to Hastelloy B and Hastelloy W, the Mo content in Hastelloy N was reduced to 15–17 wt% to preclude the aging embrittlement. Considering the resistance to molten fluoride corrosion alone, the content of less noble Cr in the alloy should be minimized. However, high-temperature air oxidation tests showed a minimum concentration of Cr was necessary to provide sufficient resistance to air oxidation. Thus, the optimized Cr content for Hastelloy N turned out to be 6–8 wt%.

In the late 1950s, the molten salt fuel technology was transferred to the civilian nuclear program. An attractive concept was the thermal breeding of uranium from thorium designed at ORNL [106]. The maximum salt temperature in the thermal breeder reactor concepts was around 700 °C which was less than ARE condition and might cause less corrosion damage. From 1958 to 1964, hundreds of loop tests were carried out to examine the corrosion resistance of Hastelloy N (Ni-16Mo-7Cr-4.5Fe) and Inconel 600 in various molten fluorides with a time duration up to one year. Extensive loop tests were conducted in $^7LiF\text{-}BeF_2$ based fuel salts as $^7LiF\text{-}BeF_2$ was the most preferred fuel carrier salt. The results of these loop tests are summarized in Tables 3–5. The entire loop was made of the investigated alloy, i.e., Hastelloy N or Inconel 600, and the wall of the loop was cut for post-test microstructural examination. The loop included a hot leg and a cold leg to simulate the temperature gradient in the primary loop of MSR. The flow of the molten salt in the thermal-convection loop was driven by the temperature difference yielding an estimated flow velocity ranging from 0.006 to 0.025 m/s. The molten salt in the forced-circulation loops was pumped to target the flow velocities of 2.3–5 m/s that are more representative in MSRs. The temperature gradient in the thermal-convection loop and forced-circulation loop was 77 °C and 93 °C, respectively. Tables 3 and 4 show that the corrosion of both alloys was highly dependent on the temperature, and the localized attack became more severe with the increase of exposure time. Although the corrosion depths of Inconel 600 under MSR temperatures were

Table 3

Results of Inconel 600 thermal convection loops operated with LiF-BeF$_2$ base salts at ORNL [114–117].

Salt composition (mol%)	Duration (h)	T_{max} (°C)	Corrosion attack at hot sections
71LiF-29BeF$_2$	1000	677	A few voids to a depth of less than 25 μm
71LiF-29BeF$_2$	8760	677	Light to moderate intergranular voids to 127 μm deep
71LiF-29BeF$_2$	8760	732	Moderate to heavy intergranular voids to 165 μm deep
53LiF-46BeF$_2$-1UF$_4$	1000	677	Subsurface voids to a depth of 64 μm
53LiF-46BeF$_2$-1UF$_4$	8760	677	Heavy intergranular voids to a depth of 178 μm
53LiF-46BeF$_2$-1UF$_4$	8760	732	Heavy intergranular voids to a depth of 381 μm
60LiF-36BeF$_2$-5UF$_4$	1000	677	Intergranular voids to a depth < 25 μm
62LiF-37BeF$_2$-1UF$_4$	1000	677	Intergranular attack to a depth < 25 μm
62LiF-37BeF$_2$-1UF$_4$	1000	732	Intergranular voids to a depth of 76 μm/102 μm/ < 54 μm[a]
62LiF-37BeF$_2$-1UF$_4$	8760	677	Heavy intergranular voids to a depth of 178 μm
62LiF-37BeF$_2$-1UF$_4$	8760	732	Heavy intergranular voids to a depth of 356 μm
58LiF-35BeF$_2$-7ThF$_4$	1000	677	Attack to a depth less than 25 μm
71LiF-16BeF$_2$-13ThF$_4$	1000	677	A few intergranular voids to a depth of 25 μm
71LiF-16BeF$_2$-13ThF$_4$	8760	677	A few intergranular voids to a depth of 102 μm
71LiF-16BeF$_2$-13ThF$_4$	8760	732	Moderate intergranular voids to a depth of 191 μm
62LiF-36.5BeF$_2$-1ThF$_4$-0.5UF$_4$	1000	677	Moderate intergranular voids to a depth of 76 μm
62LiF-36.5BeF$_2$-1ThF$_4$-0.5UF$_4$	8760	677	Moderate intergranular voids to a depth of 127 μm
62LiF-36.5BeF$_2$-1ThF$_4$-0.5UF$_4$	8760	732	Heavy intergranular voids to a depth of 305 μm

[a] Results from replicate tests.

Table 4

Results of Hastelloy N thermal convection loop operated with LiF-BeF$_2$ base salts at ORNL [114,116–118].

Salt composition (mol%)	Duration (h)	T_{max} (°C)	Corrosion attack at hot sections
71LiF-29BeF$_2$	1000	677	Light surface roughening
71LiF-29BeF$_2$	8760	677	Light surface roughening
71LiF-29BeF$_2$	8760	732	Heavy surface roughening
70LiF-10BeF$_2$-20UF$_4$	1000	677	No observable attack
70LiF-10BeF$_2$-20UF$_4$	1000	732	Moderate surface roughening
62LiF-37BeF$_2$-1UF$_4$	1000	677	No observable attack
62LiF-37BeF$_2$-1UF$_4$	8760	677	Light surface roughening
62LiF-37BeF$_2$-1UF$_4$	8760	732	Light surface roughening
60LiF-36BeF$_2$-4UF$_4$	1000	677	No observable attack
60LiF-36BeF$_2$-4UF$_4$	8760	677	Moderate surface roughening
53LiF-46BeF$_2$-1UF$_4$	1000	677	No observable attack
53LiF-46BeF$_2$-1UF$_4$	8760	677	No observable attack
53LiF-46BeF$_2$-1UF$_4$	8760	732	Light surface roughening
71LiF-16BeF$_2$-13ThF$_4$	1000	677	No observable attack
71LiF-16BeF$_2$-13ThF$_4$	8760	677	No observable attack
71LiF-16BeF$_2$-13ThF$_4$	8760	732	Light surface roughening
58LiF-35BeF$_2$-7ThF$_4$	8760	677	Light to moderate surface roughening with a few pits
58LiF-35BeF$_2$-7ThF$_4$	8760	732	Light scattered intergranular voids to < 51 μm deep
53LiF-46BeF$_2$-0.5ThF$_4$-0.5UF$_4$	8760	677	Moderate pits (< 25 μm deep)
53LiF-46BeF$_2$-0.5ThF$_4$-0.5UF$_4$	8760	732	Moderate surface roughening
62LiF-36.5BeF$_2$-1ThF$_4$-0.5UF$_4$	8760	677	Light surface roughening with pits < 12 μm deep
62LiF-36.5BeF$_2$-1ThF$_4$-0.5UF$_4$	8760	732	Light surface roughening

lower than that under ARE conditions, the corrosion resistance of Inconel 600 still might be inadequate considering the 40-year service time of the commercial reactors. In comparison, most Hastelloy N loop tests showed little corrosion attack, and only a few tests showed voids or pitting with relatively smaller corrosion depths (< 51 μm). The superior corrosion resistance of Hastelloy N to molten fluorides was also demonstrated from the MSRE operation experience. MSRE was an 8 MW graphite moderated reactor which was operated successfully from 1965 to 1969 [25]. In MSRE, all metal components exposed to the molten salt were made of Hastelloy N. The corrosion of Hastelloy N was found to be negligible as indicated by the examination of the MSRE surveillance specimens and the concentration of the dissolved Cr in the fuel salt [25]. However, two main problems of Hastelloy N were discovered during the construction and operation of MSRE: irradiation embrittlement and tellurium induced IGC.

The effects of neutron radiation on nickel-based alloys have been reviewed recently by Stopher [120]. One of the main causes for irradiation embrittlement of nickel-based alloys is the accumulation of helium in the grain boundaries, which is produced from the transmutation reactions of nickel and impurities such as boron. Considerable efforts were spent on the modification of Hastelloy N at ORNL, and alloy elements Ti and Nb were found to be beneficial [121]. With the additions of Ti and/or Nb, fine and dispersed carbides formed within the grain matrix which trapped the helium and prevented its migration to the grain boundaries. The other two alloying elements that improve the irradiation embrittlement of Ni-Mo-Cr alloys are Al and V, as discovered later by Kurchatov Institute (KI) [122]. Shallow intergranular cracks on Hastelloy N surveillance samples and the structural components of MSRE were

Table 5
Forced-circulation loop tests operated with LiF-BeF$_2$ salts at ORNL [116,117,119].

Material	Salt composition (mol%)	Duration (h)	T_{max} (°C)	Corrosion attack at hot sections
Inconel	53LiF-46BeF$_2$-1UF$_4$	3390	704	Intergranular voids to a depth of 178 µm
Inconel	62LiF-37BeF$_2$-1UF$_4$	3046	704	Intergranular voids to a depth of 203 µm
Inconel	60LiF-36BeF$_2$-4UF$_4$	8746	704	Intergranular voids to a depth of 356 µm
Inconel	62LiF-37BeF$_2$-1UF$_4$	9574	704	Intergranular voids to a depth of 381 µm
Inconel	71LiF-16BeF$_2$-13ThF$_4$	13,155	704	Intergranular voids to a depth of 330 µm
Inconel	62LiF-36.5BeF$_2$-1ThF$_4$-0.5UF$_4$	15,038	704	Intergranular voids to a depth of 610 µm
Hastelloy N	53LiF-46BeF$_2$-1UF$_4$	14,563	704	Heavy surface roughening and pitting
Hastelloy N	62LiF-37BeF$_2$-1UF$_4$	15,140	704	Light surface roughening and pitting
Hastelloy N	62LiF-37BeF$_2$-1UF$_4$	14,503	704	No observable attack
Hastelloy N	70LiF-10BeF$_2$-20UF$_4$	14,498	704	No observable attack
Hastelloy N	71LiF-16BeF$_2$-13ThF$_4$	20,000	704	Pitted surface layer to 25 µm
Hastelloy N	62LiF-36.5BeF$_2$-1ThF$_4$-0.5UF$_4$	14,498	704	No observable attack
Hastelloy N	62LiF-36.5BeF$_2$-1ThF$_4$-0.5UF$_4$	20,000	704	Pitted surface layer to 51 µm
Hastelloy N	62LiF-36.5BeF$_2$-1ThF$_4$-0.5UF$_4$	9687	704	No observable attack

observed which was attributed to the fission product tellurium. Research efforts at the very end of the MSR program at ORNL showed additions of Nb alone improved the resistance to Te-induced IGC and a minimum cracking severity was observed in alloys containing from 1 to 2% Nb [121]. However, the long-term performance of Nb-modified alloys was still concerned as the persistent increase rate of cracking severity with time was observed from tests up to 2500 h.

To demonstrate the long-term performance of Hastelloy N alloys, several Hastelloy N loop tests with inserted specimens made of standard Hastelloy N and the Ti- and Nb-modified Hastelloy N alloys were carried out [101,102,123]. In general, the modified Hastelloy N alloys showed equivalent or less corrosion compared to the standard Hastelloy N. One Hastelloy N thermal convection loop was operated with the MSRE fuel salt (70LiF-23BeF$_2$-5ZrF$_4$-1ThF$_4$-1UF$_4$, mol%) at a maximum temperature of 704 °C for 9.2 years. The examination of metallographic samples from various sections of the loop showed only uniform subsurface voids attack to a depth less than 76 µm [123].

Due to the concern on the tellurium embrittlement of Hastelloy N, the corrosion resistance of several alloys with better resistance to Te-induced IGC were evaluated in LiF-BeF$_2$-based fuel salts. These alloys include the 300 series stainless steels, and nickel-based alloys with Cr content of about 23 wt% [121]. A thermal-convection loop made of Hastelloy N was operated for 2776 h at 690 °C with inserted Monel (65Ni-35Cu), Hastelloy N, Inconel 600, Inconel 606 (Ni-20Cr-2Fe), Inconel 601 (Ni-23Cr-14Fe), Inconel 690 (Ni-30Cr-15Fe), and Incoloy 811E (Fe-23Cr-30Ni) specimens [101]. The weight change results and the attack information are listed in Table 6. The results showed that increase in Cr and Fe contents were detrimental on both total weight change and localized attacks. Compared to the predictions in Fig. 4, the effects of Cr content were more pronounced in this loop test especially for these alloys containing more than 20 wt% Cr. It is not clear if the galvanic coupling of dissimilar alloys accidentally occurred which can cause the accelerated corrosion of higher Cr containing alloys and simultaneous deposit on more noble Monel alloy specimen (see Table 6). It needs to be noted that, there are also experimental results showing that corrosion rates of Hastelloy N, Inconel 600 and other low Cr alloy such as Haynes 242 were only ~1.5–5 times lower than the corrosion rates of Fe- or Ni-based alloys containing 20 wt% Cr [124–126]. A type 304 stainless steel thermal-convection loop with 70LiF-23BeF$_2$-5ZrF$_4$-1ThF$_4$-1UF$_4$ fuel salt was operated at a maximum temperature of 677 °C for 9.5 years. The weight loss results of the inserted type 304 SS specimen corresponded to a corrosion rate of ~50 µm/year in the first 2244 h [101], which is in the same order of magnitude with the prediction for 71Fe-17Cr-12Ni model alloy. In the last 5700 h of this test, a new set of specimens were inserted for comparison which showed a corrosion rate of ~28 µm/year 304 SS, ~14 µm/year maraging steel (12Ni-5Cr-3Mo), and 1.5 µm/year for Hastelloy N alloy. Compared to the 9.2-year Hastelloy N loop test results mentioned before (i.e., voids attack of less than 76 µm), the localized attack on 304 SS was far more severe which showed intergranular voids attack to a depth of 254 µm after 5.2-year exposure in the same fuel salt [101]. These results indicated the resistance of stainless steels and nickel-based alloys with more than 20 wt% Cr might be inadequate for MSRs although they showed improved resistance to Te-induced IGC.

In Russia, the program on the molten salt-fueled reactors was started at KI in the late 1970s [122]. The interest was initially

Table 6
Corrosion rates of various alloys in 68LiF-20BeF$_2$-11.7ThF$_4$-0.3UF$_4$ (mol%) at 690 °C for 2776 h [101].

Alloy	Cr content (wt%)	Fe content (wt%)	Corrosion rate[a] (µm/year)	Localized attack
Monel (65Ni-35Cu)	–	–	Weight gain	Deposit layer with voids underneath
Hastelloy N	7	5	0.5	No attack
Inconel 600	15	7	1.8	Little attack
Inconel 606	20	2	24.7	Partial heavy attack
Inconel 601	23	14	62.3	127 µm deep voids
Inconel 690	30	15	213.8	381 µm deep voids
Incoloy 811E	21	47	463.2	457 µm deep voids

[a] Converted from weight loss by assuming a uniform corrosion.

Table 7
Chemical composition of the nickel-base alloys (wt%) [101,121 – 123].

Element	Hastelloy N	Hastelloy N Ti-mod.	Hastelloy N Nb-mod.	HN80MT	HN80M-VI	HN80MTY
Ni	Base	Base	Base	Base	Base	Base
Mo	16–17	11–14	11–13	12.1	12.2	13.2
Cr	7.1	6–8	6–8	7.02	7.61	6.81
Fe	4–5	0.1	0.1	< 0.33	0.28	0.15
Mn	0.55	0.15–0.25	0.15–0.25	< 0.1	0.22	0.013
Ti	< 0.01	0.5–2	–	1.72	0.001	0.93
Nb	–	0–2	1–2	–	1.48	0.01
Al	0.03	–	–	–	0.038	1.12
Si	0.57	0.1	0.1	< 0.05	0.04	0.04
W	0.14	–	–	–	0.21	0.072
Co	0.03	–	–	–	0.003	0.003
Cu	–	–	–	< 0.01	0.12	0.02
C	0.06	0.05	0.05	0.004	0.02	0.025

directed to the MSBR concepts but switched to the single stream MOSART after 2001. The development of the structural materials exposed to the fluoride fuel salts was based on the data accumulated during the MSR program at ORNL. A Ni-based alloy HN80MT with similar composition as Ti-modified Hastelloy N was chosen as a base. About 70 modified HN80MT with various amount of alloying elements W, Nb, Re, V, Al, Mn, and Cu were tested to find the optimized composition that has sufficient resistance to both corrosion and Te embrittlement. Corrosion tests were carried out in flow loops and static isothermal capsules. The main finding was that the decrease of titanium content by 0.5 wt% significantly improved the corrosion resistance of HN80MT, and the extent of the selective chromium dissolution and intergranular corrosion was minimized at an Al content of ~2.5 wt% [122]. The chemical compositions of the representative HN80MT alloys and the Hastelloy N alloys are given in Table 7.

4.2. *Key factors influencing corrosion in molten fluorides*

The materials corrosion in molten fluorides is influenced by a number of factors, including environmental and metallurgical variables. The main parameters found in published sources are summarized in this section.

4.2.1. *Oxidants in the salt*

(1) Fuel component UF_4

The fuel component UF_4 is an inherent oxidant in fluoride fuel salts. As evidenced by the results of the ORNL's loop tests (Table 3), the voids attack on Inconel 600 in UF_4 containing molten salts were more severe and generally deeper than the attacks in the same base salts without UF_4 additions. Direct evidence of the metal corrosion by UF_4 can be found from several loop tests that equipped electrochemical probes to determine the concentration ratio of U(IV)/U(III) in the salt. The decrease of U(IV)/U(III) concentration ratio with time was observed which was attributed to the reduction of UF_4 during metal corrossion. The time scale for the drop of U (IV)/U(III) concentration ratio from $\sim 10^4$ to $\sim 10^2$ in Hastelloy N loops was about thousands of hours but only a few days for the less resistant Inconel 601 [101,102], indicating the consistency of the metal dissolution rate and reduction rate of U(IV).

The driving force of the corrosion by UF_4 is the relatively more positive potential of U(IV)/U(III) than the oxidation potential of less noble metals such as Cr. On the kinetics aspect, the exchange current density or the rate constant of the U(IV)/U(III) reaction is several orders of magnitude greater than that of metal dissolution reactions (Fig. 4). Hence, the metal will be polarized to a more positive potential that is closer to U(IV)/U(III) potential, resulting in relatively larger metal dissolution rate. To mitigate the corrosion of Cr, the concentration ratio of U(IV)/U(III) needs to be lowered which is able to reduce the overpotential of Cr dissolution reaction. This lead to the development of redox control using U(IV)/U(III) which are discussed in Section 6.

(2) Structural metal impurities

The significant influence of FeF_2 impurities was initially recognized during the MSR program at ORNL [114]. A Hastelloy N loop test with circulating $65.5LiF\text{-}34BeF_2\text{-}0.5UF_4$ fuel salt was operated at a maximum temperature of 704 °C for 37,942 h. The initial 500 ppm FeF_2 was added at 29,500 h, and additional 500 ppm FeF_2 was added at 1100 h after the first addition. The weight change of Hastelloy N specimens in the next 2900 h following the first addition of FeF_2 was about six times of that in the initial 29,500 h. In other word, the corrosion rate was increased by a factor of ~59 after additions of FeF_2. The local attack also became more severe due to the addition of FeF_2. Some grain boundary attack started to appear after the initial addition of FeF_2, and shallow cracks to a depth of 13 μm in the Cr depleted zone as well as voids were observed in the next few thousands of hours. Another evidence of metal corrosion by the reduction of structural metal cations is the deposition of these cations on the metal surface. Ye et al. [99] applied electro-probe micro-analyzer (EPMA) mapping technique and observed a 1–2 μm thick Fe deposition layer on the surface of Hastelloy N which was attributed to the reduction of Fe ions impurities (~150 ppm) in the FLiNaK salt.

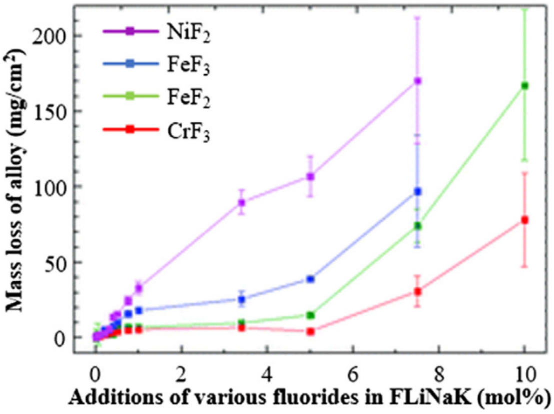

Fig. 6. Mass loss of Incoloy 800H/HT in FLiNaK with additions of various fluorides. Test duration: 8 h; Temperature: 650 °C [68].

A more comprehensive study on structural metal impurities was performed by Pavlik et al. [68] in which the effects of CrF_3, FeF_3, FeF_2, and NiF_2 concentrations on the corrosion of Incoloy 800H/HT in molten FLiNaK were investigated. Tests were carried out in alumina crucibles at 650 °C. The salt was vacuum-treated at 130 °C for 48 h, and then corrosion tests were performed under Ar atmosphere. The test duration was 8 h, attempting to identify the initial corrosion rate using weight loss method. The weight loss results are summarized in Fig. 6. The increase of mass loss with the increase in impurity concentrations was attributed to the increase of the redox potential and the exchange current density for the reduction reaction of the added metal cation. The dependence of mass loss upon concentrations of FeF_3, FeF_2, and CrF_3 showed some irregularities as a gradual decline of the slope is expected based on the kinetics simulation. This might be related to the change of activity coefficients of cations in the salt. Nevertheless, corrosiveness of the structural-metal impurities at the same concentrations increased in the following sequence: Cr(III) < Fe(II) < Fe(III) < Ni(II). Pavlik et al. [68] indicated that the observed sequence was consistent with elements' standard potential order: Cr(III)/Cr < Fe(II)/Fe < Fe(III)/Fe < Ni(II)/Ni. However, it should be noticed that Cr(III) is reduced to Cr(II) rather than Cr during corrosion. The standard potential of Cr(III)/Cr(II) and its redox potentials at these experimental concentrations are actually more positive compared to Fe(II)/Fe. This indicates that the differences in kinetic parameters play important roles.

Corrosion by CrF_3 is more concerned as CrF_3 can be generated from the disproportionation reaction of CrF_2 which is a major corrosion product in molten fluoride salts [127]. Wang et al. [69,70] further investigated the effect of CrF_3 additive using electrochemical techniques. The salt was preheated at 200 °C under vacuum conditions for at least 20 h and then tests were carried out at 700 °C under argon atmosphere. Test materials included pure Ni, Fe, Cr metals, and Hastelloy N. The initial corrosion kinetics of pure metals and Hastelloy N were characterized by the potentiodynamic polarization curves, as shown in Fig. 7. In general, under the same conditions, corrosion current density increased in the following order: Ni < Hastelloy N ≈ Fe < Cr. Compared to pure nickel, the influence of CrF_3 on the corrosion of less noble materials (i.e., chromium, iron, and Hastelloy N) was more pronounced. The effect of CrF_3 was attributed to the accelerated reduction rate of CrF_3 on the metal surface as indicated by the positive shift of the cathodic polarization curve with the increase in CrF_3 concentration. Such an increase resulted in the rising of the corrosion potential and the increase of corrosion current density especially for the less noble materials. Considering the selective dissolution of alloy, with the increase of exposure time the corrosion of Hastelloy N would be slowed down by the diffusion rate of Cr through the depletion zone. The evolution of corrosion resistance of Hastelloy N with time during the 100 h corrosion tests was characterized by electrochemical impedance spectroscopy. However, the results in systems with and without CrF_3 additions indicated minor changes of corrosion rate with time. As predicted at 100 h and 8760 h in Fig. 4d, this might be attributed to the relatively small time scale in which the limiting current density likely remained high. The posttest samples were examined by the scanning electron microscope (SEM) and energy-dispersive X-ray spectroscopy (EDS) analysis. The depletion of Cr/Fe and the formation of sublayer voids in Hastelloy N after 100 h of corrosion were observed. The thickness of the depletion or voids attack layer were 80 μm and 150 μm in salt containing 0.08 M and 0.18 M CrF_3 respectively, compared to the 30 μm in CrF_3-free condition.

(3) Water impurity

The detrimental effects of water moisture on the corrosion in molten fluorides have been reported by many researchers. Ouyang et al. [124] investigated the corrosion characteristics of Hastelloy N and Hastelloy B3 in FLiNaK salt containing different moisture contents at 700 °C. Tests were carried out in static nickel containers with dry argon gas flowing through the cover gas space. Prior to the tests, the salt mixture was pre-heated to 300 °C for 12 h and 150 °C for 3 h respectively, corresponding to moisture contents of 1.91 wt% and 3.19 wt% in the FLiNaK salts. The weight loss results of the two alloys were quite similar at 100 h and 200 h. The general corrosion rates indicated by the weight loss were 4–5 $\text{mg cm}^{-2}\,\text{day}^{-1}$ under 1.91 wt% water moisture, and 14–15 $\text{mg cm}^{-2}\,\text{day}^{-1}$ under 3.19 wt% water moisture, respectively. Hence, the corrosion rate was tripled by increasing the water content. The SEM examinations also indicated a more severe intergranular and pitting corrosion at higher moisture content. Sona et al. [126] investigated the corrosion of SS 316L, Inconel 625, and Hastelloy B in FLiNaK with and without 3-hour salt dehydration at

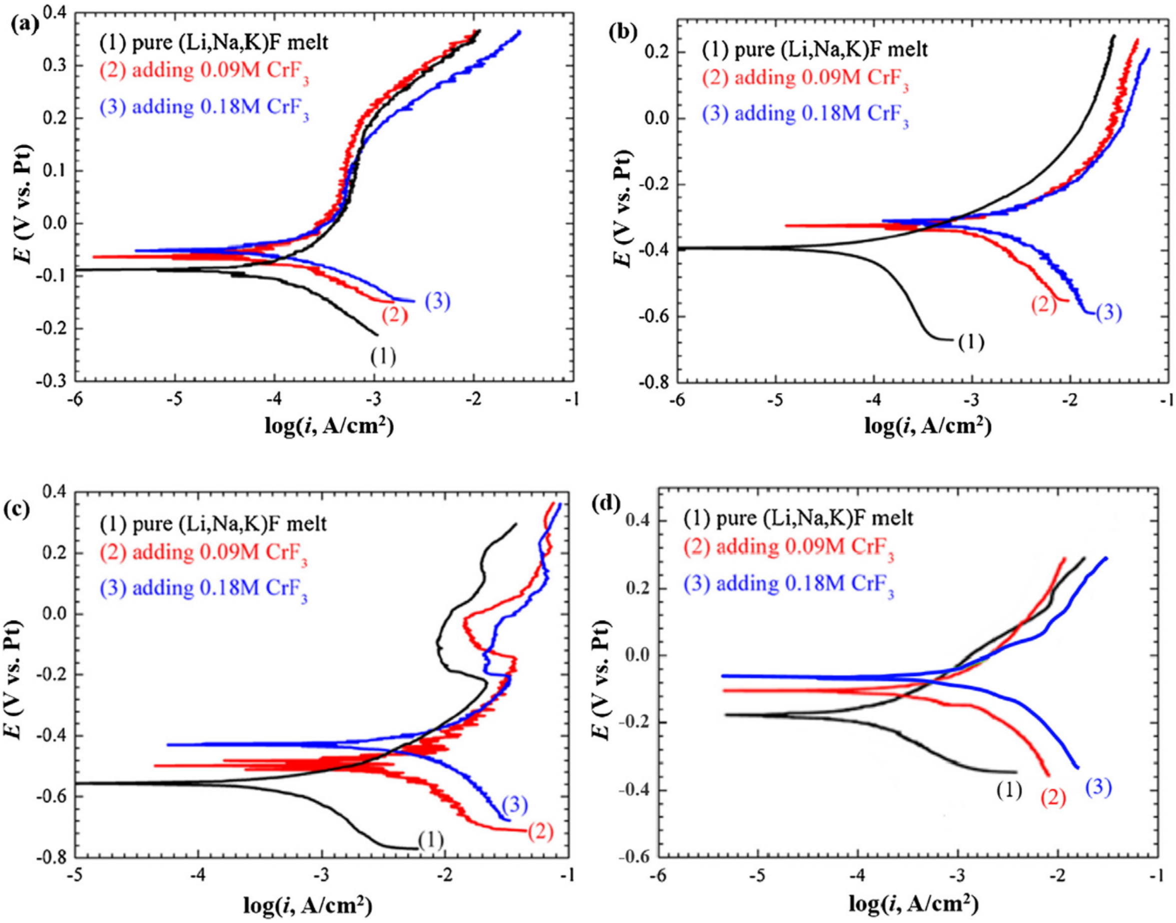

Fig. 7. Potentiodynamic polarization curves of (a) pure Ni, (b) pure Fe, (c) pure Cr, and (d) Hastelloy N in FLiNaK with and without additions of CrF_3 at 700 °C. Reproduced based on [69,70].

130 °C. Static tests were conducted in graphite containers at 650 °C under a nitrogen atmosphere for 60 h. The weight loss results indicated the corrosion rates were decreased by factors of 1.7–5 for the three tested alloys after the dehydration treatment. The enhanced corrosion by water moisture was also characterized by Wang et al. [69,70] using electrochemical techniques. The experiments were conducted at 700 °C in a stainless steel chamber with gaseous Ar or Ar-H_2O flowing through the cover gas zone. Vacuum treatment of the FLiNaK salt at 200 °C was performed before the tests. Fig. 8 shows the potentiodynamic polarization curves of pure metals and Hastelloy N under Ar and Ar-H_2O environments. Compared to the CrF_3 effects in Fig. 7, the presence of water moisture not only increased the cathodic reaction current densities but also the anodic metal dissolution current densities. The corrosion current densities determined for pure Cr, Fe, and Ni metals were 3.715, 1.425, and 0.150 mA/cm^2 under Ar-2%H_2O atmosphere, compared to 0.494, 0.261, and 0.0193 mA/cm^2 under Ar atmosphere. For Hastelloy N, the corrosion current densities were 0.108 and 0.374 mA/cm^2 under Ar and Ar-5%H_2O atmosphere, respectively. The presence of 5% water moisture in the gas phase also enhanced the Cr depletion and voids attack in Hastelloy N, e.g., the thickness of the Cr depletion layer increased by ~10 μm after corrosion of 100 h in FLiNaK.

A significant increase in anodic current density by the presence of water in the salt is indicated in Fig. 8. This recalls the question on the mechanism of metal dissolution reactions in molten fluoride salt that was proposed in Section 3.2.4. This experiment supports the idea that OH^- in molten fluoride salts is involved in the metal dissolution reactions by forming hydroxylated metal compounds. Thus, like aqueous solutions, the anodic metal dissolution reaction rate in molten fluorides is also accelerated by increasing the OH^- concentration. It will be beneficial to further characterize the dependence of anodic dissolution kinetics of metals on water concentrations in molten fluoride salts as it improves the understanding on the metal dissolution mechanism and more importantly the model simulation.

Figs. 7 and 8 also indicate the character of active metal dissolution in molten fluoride salts. Some narrow distortion of the Cr polarization curves above −0.2 V were observed in Figs. 7c and 8c which might be related to the formation of passivating oxide layer. However, the passivating current densities were still high, and the passivation occurred at significantly more positive potentials rather than the corrosion potential. Hence, the metal was still under active dissolution. This was supported by the microstructural analysis of the posttest samples from all experimental results in Section 4 which showed no presence of oxide layers on the metal

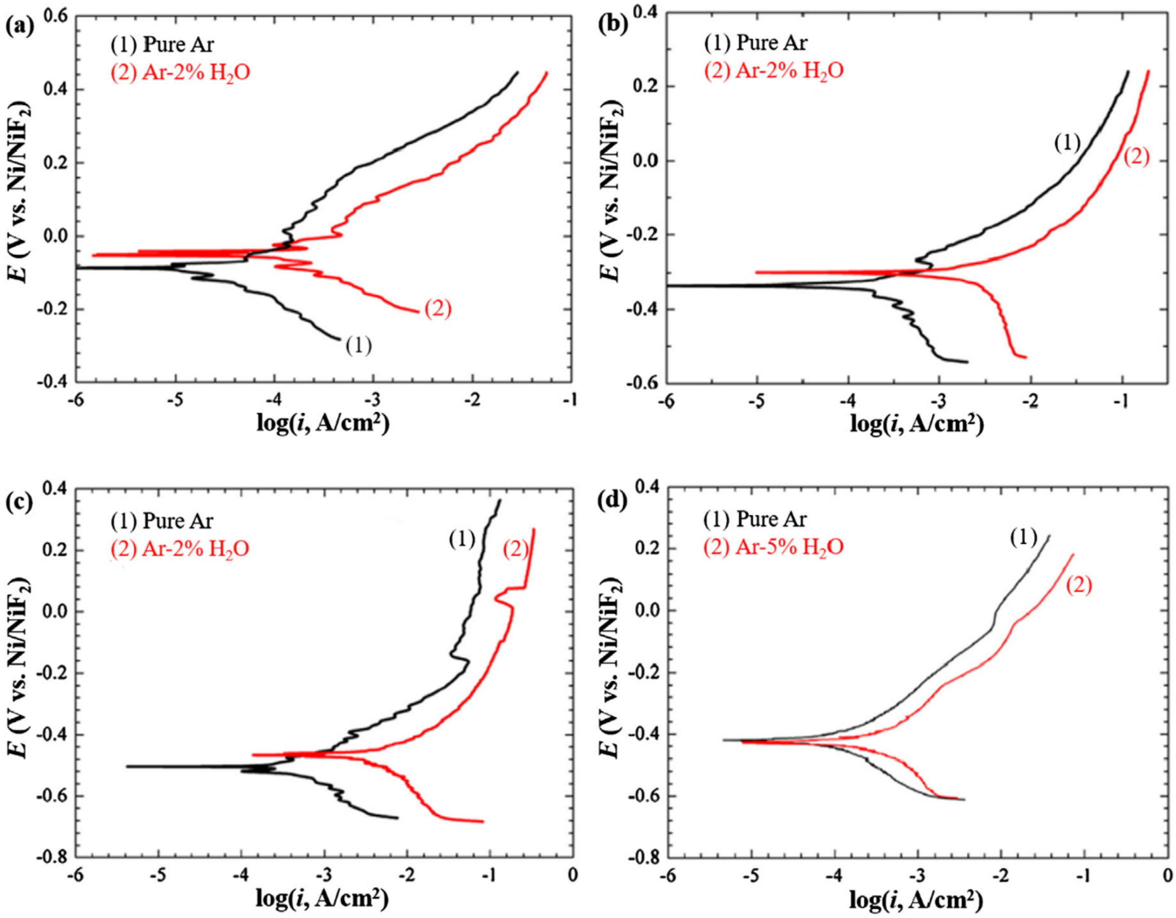

Fig. 8. Potentiodynamic polarization curves of (a) pure Ni, (b) pure Fe, (c) pure Cr, and (d) Hastelloy N in FLiNaK under Ar and Ar-H_2O environments at 700 °C. Reproduced based on [69,70].

surface in molten fluoride salts. Therefore, the formation of oxide layers is very challenged in molten fluorides even in salts with relatively higher water contamination, leading to the active dissolution of bare metals or alloys.

4.2.2. Tellurium induced intergranular cracking (IGC)

Tellurium is one of the most harmful fission products to the structural material. During the operation of MSRE, the shallow IGC induced by Te was observed in Hastelloy N exposed to the fuel salt [121]. The auger spectroscopy analysis of the Hastelloy N surveillance sample from MSRE showed that only Te was present in the brittle grain boundary and the concentration was about 25 at.% [121]. Such high concentration of Te is adequate to form considerable amounts of brittle intermetallic compound Ni_3Te_2 at MSRE service temperature as indicated by the Ni-Te binary phase diagram [128]. In fact, the segregated solute Te at the grain boundaries also increases the embrittlement tendency [129]. Numerous demonstrative tests were carried out at ORNL which showed similar IGC character on the alloys exposed to the molten fluoride salt containing Te, or Cr_3Te_4, or Cr_5Te_6 [121]. The addition of Te, Cr_3Te_4, or Cr_5Te_6 in the salt was used to simulate the tellurium flux reaching the metal in the reactor conditions. Thus, it was believed the tellurium caused the IGC during MSRE operation.

Cheng et al. [66,130] characterized the brittle telluride compounds formed by the reaction of Te vapor with Hastelloy N at 700 °C. The X-ray diffraction (XRD) analysis identified that the telluride compounds formed on the surface and grain boundaries of the Hastelloy N consisted of Ni_3Te_2, CrTe, and $MoTe_2$. The EPMA and scanning transmission electron microscope (STEM) found that the Te predominantly diffused along the grain boundaries, and the CrTe compound was primarily formed on the grain boundaries and the interfaces between the Mo-rich intergranular carbides and the alloy matrix [66]. Ignatiev et al. [122] found the extent of the IGC induced by Te was related to the distribution and character of the carbides. The addition of Al in HN80MT significantly improved the resistance to IGC because the carbide phase in the grain boundaries decreased and appeared as separated round particles. These are somewhat consistent with Cheng et al.'s finding [66], as fewer carbides in the grain boundaries provided fewer sites for the formation of brittle telluride compounds. The discontinuous intergranular carbides might also reduce the possibility of forming a continuous brittle telluride film along the grain boundary.

The diffusion behavior of Te into nickel was characterized by Jia et al. [67] at various temperatures. The nickel specimens with an

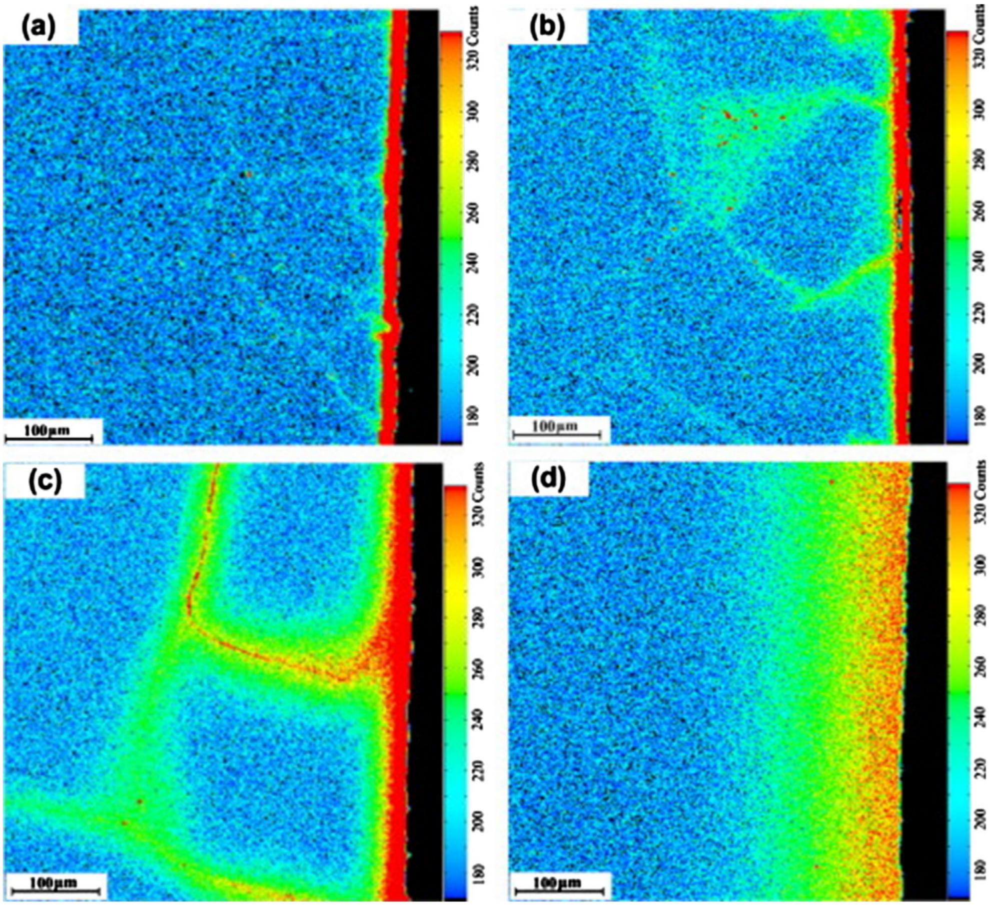

Fig. 9. Electron probe microanalysis (EPMA) mapping showing the distribution of Te for the sample annealed at (a) 700 °C, (b) 800 °C, (c) 900 °C, and (d) 1000 °C [67].

electroplated Te layer were annealed at each temperature for 100 h. As shown in Fig. 9, the diffusion of Te into nickel was primarily by grain boundary diffusion below 900 °C and switched to lattice diffusion above 1000 °C. The existence of Ni_3Te_2 accompanied with trace $Ni_3Te_{2.07}$ was identified by XRD at temperatures ranging from 500 to 900 °C. No intermetallic compound was detected at 1000 °C because no intermetallic is stable at such high temperature [128].

According to above results, the Te-induced IGC was caused by the preferential diffusion of Te along the grain boundaries followed by the formation of the brittle telluride compounds. Delpech et al. [17] thought that tellurides such as Ni_xTe_y and Cr_xTe_y could be formed by the corrosion reaction of the structural metals with Te in the molten salts. Depending on the salt redox conditions, tellurium may present in the salt in its metallic form and cause metal corrosion by reduction to its negative oxidation states Te(-I) and Te(-II). Two pieces of evidence were found supporting this proposed mechanism. The first is the mitigation of Te-induced IGC by decreasing the concentration ratio of the U(IV)/U(III) in the fluoride fuel salts as found by ORNL [131] and KI [132]. By keeping the salt sufficiently reducing, Te in the salt was probably reduced to its negative valences by the oxidation of U(III) to U(IV) in the salt. The tests at ORNL were carried out at 700 °C in a static vessel containing MSBR fuel salt ($72LiF\text{-}16BeF_2\text{-}11.7ThF_4\text{-}0.3UF_3$) with Cr_3Te_4 and Cr_5Te_6. The cross-sectional examination of the standard Hastelloy N specimens showed very little cracking at U(IV)/U(III) concentration ratios of 10, 30 and 60, compared to the extensive cracks at ratios of 85 and 300. Tests were also conducted at KI in the $LiF\text{-}BeF_2$ molten salt containing 20 mol% of ThF_4, 2 mol% of UF_4 and additives of Cr_3Te_4. Test alloys were HN80MTY, HN80M-VI, HN80MTW (Ni-9.4Mo-7.6Cr-1.7Ti-5.5W), and EM-721 (Ni-5.7Cr-0.17Ti-25.2W). It was found that all test alloys suffered from Te-induced IGC attack at a U(IV)/U(III) concentration ratio of 500. With a decrease of U(IV)/U(III) ratio to 100, the IGC attack was completely absent on HN80MTY and HN80M-VI alloys while tellurium was detected on the grain boundaries of HN80MTB and EM-721 alloys which might be a sign of the incipient IGC. In the fuel salt with U(IV)/U(III) concentration ratios of 0.7, 4 and 20, no IGC attack was found on all tested alloys.

Further evidence is the mitigation of Te-induced IGC by applying the cathodic polarization to the alloy, as recently found by Fabre et al. [94]. As shown in Fig. 10, the alloy C22 suffered severe IGC attack when small amounts of liquid Te was added in the molten salt. However, the IGC attack disappeared when the alloy C22 was polarized to a more negative potential, −3.4 V versus F_2/F^-.

The computed $E\text{-}pO^{2-}$ diagram of Zr-Te-O-F system is shown in Fig. 11. The red lines for Ni_2Te_3/Ni and Mo_3Te_4/Mo were also plotted, above which the corresponding metal tellurides are stable. The stability domains for the metal tellurides overlapped with the

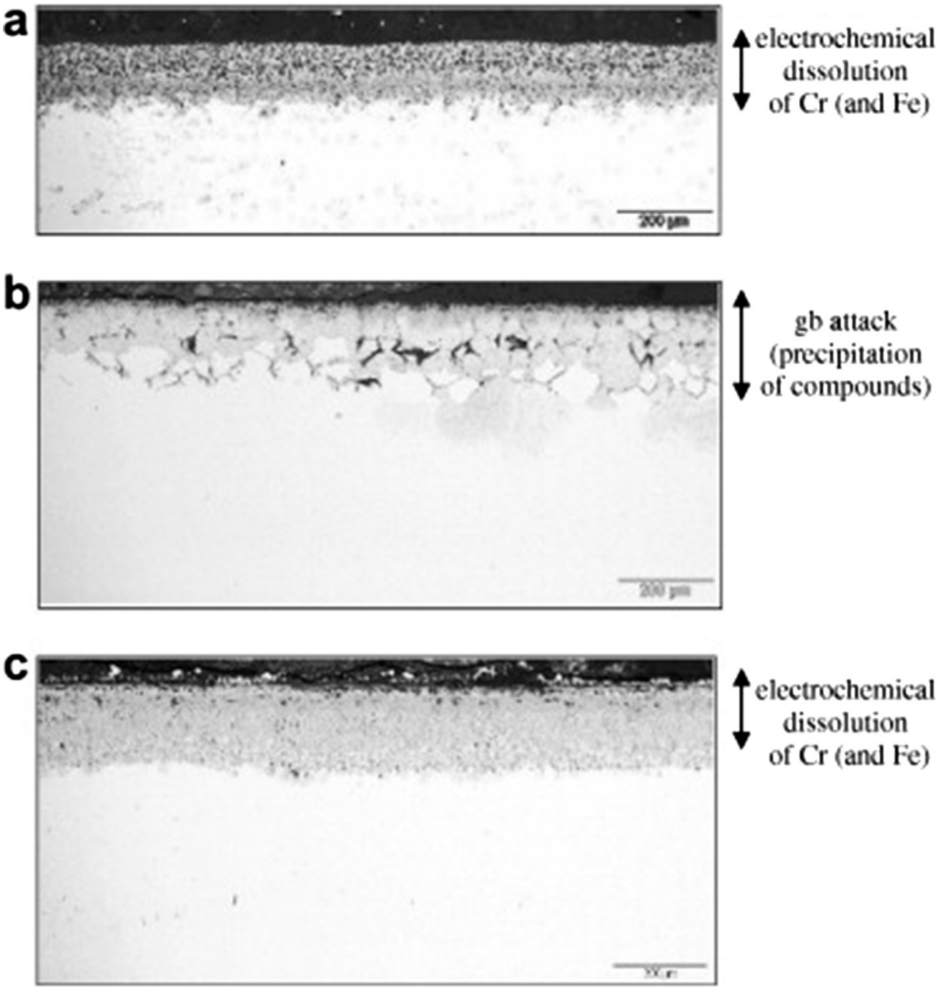

Fig. 10. Cross-sectional micrographs of alloy C22 (Ni-22Cr-14Mo-3W-3Fe) immersed for 2 weeks in LiF-CaF_2-MgF_2-ZrF_4 at 953 K: (a) without Te in salt, (b) with Te in salt, (c) with Te in salt and polarization of alloy to −3.4 V versus F_2/F^- [94].

Te(0) stability domain, indicating the formation of tellurides by Te(0) at these potential regions. It was observed that, $ZrTe_2$ was stable at the applied potential −3.4 V versus F_2/F^-. This indicated that tellurium was probably reduced to Te(-II) at −3.4 V, forming $ZrTe_2$ compound with zirconium cations in the molten salt. Thus, like the control of salt redox condition through U(IV)/U(III), the cathodic polarization also mitigates the Te-induced IGC by reducing the Te to its negative oxidation states. In addition to making tellurium not oxidizing, formation of Te anions or $ZrTe_2$ compound in the molten salts, as forced by these two techniques, also slowed down or disabled the diffusion of tellurium along the grain boundaries, thus preventing the Te-induced IGC.

4.2.3. *Interaction with dissimilar materials*

The impact of dissimilar materials on the corrosion of the metallic materials in molten FLiNaK salt was observed in Refs. [103,127,133,134]. Tests were carried out under argon atmosphere in static and isothermal containers made of various materials. In all these tests, the testing specimens were in electrical contact with the containers. The results of these tests are summarized in Table 8. In general, corrosion was largely accelerated in nickel and graphite containers and was accompanied by the formation of carbides or Ni-Cr alloy layer on the containers. The details of the results are discussed below.

Kondo et al. [103] investigated the corrosion behaviors of JLF-1 steel (Fe-8.92Cr-2W) in JLF-1, Ni, and Nb containers. Compared to the test in JLF-1 container, the corrosion of JLF-1 was significantly increased by coupling with Ni container, and a deposited Ni-Fe alloy layer on the Ni container was observed from SEM/EDS analysis. For the test in Nb crucible, weight gain of JLF-1 was found due to deposited Nb particles on the JLF-1 surface. Only 11 ppm Cr and 29 ppm Fe were detected in the salt after the test while the dissolved Nb in the salt was 940 ppm, indicating the Nb was preferentially corroded when coupled with JLF-1 steel. Olsen et al. [127] found that the corrosion rates of Incoloy 800H (45.3Fe-31.6Ni-20.4Cr) in the graphite and nickel containers were greatly increased compared to containers made of the same material or pyrolytic boron nitride (PyBN). The accelerated corrosion in graphite or nickel container was accompanied with the formation of the carbide layer on the graphite container, or Ni-Cr alloy layer on nickel container. The carbide layer consisted primarily of Cr_7C_3 with trace $Cr_{23}C_6$, as identified by XRD and X-ray photoelectron spectroscopy (XPS)

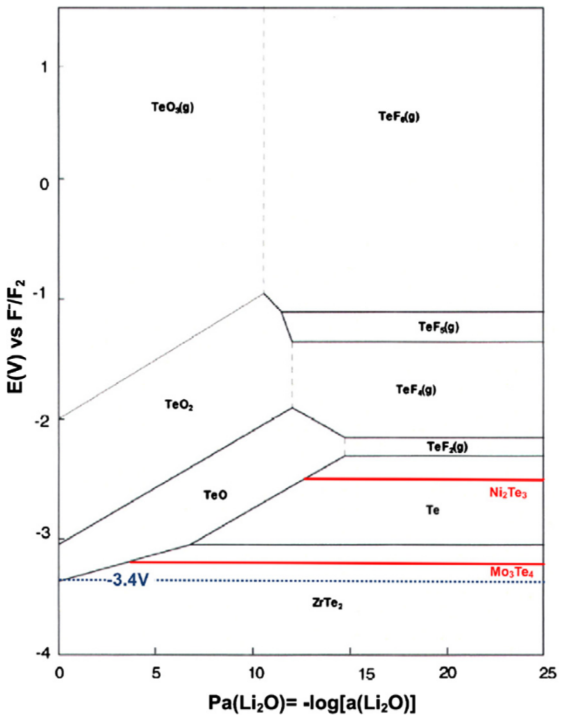

Fig. 11. E-pO^{2-} diagram of system Zr-Te-O-F at 953 K with lines for Ni_2Te_3/Ni and Mo_3Te_4/Mo [94].

Table 8

Corrosion of materials in contact with dissimilar materials in molten FLiNaK.

Specimen	Container	Temp. (°C)	Time (h)	Corrosion rate[a] (μm/year)	Observed deposit	Ref.
Incoloy 800H	Graphite	850	500	630.3 ± 57.3	Cr_7C_3 layer on Graphite	[127]
Incoloy 800H	Ni	850	500	727.2	Ni-Cr alloy layer on Ni	[127]
Incoloy 800H	PyBN	850	500	22.0	No	[127]
Incoloy 800H	Incoloy 800H	850	500	4.4	No	[127]
Hastelloy N	Graphite	850	500	45.5 ± 4.0	No	[127]
Hastelloy N	Ni	850	500	15.8	–	[127]
Cr	Graphite	700	500	1616.4 ± 317.3	Cr_7C_3 layer on Graphite	[133]
Cr	Ni	700	500	1027.5 ± 120.0	Ni-Cr alloy layer on Ni	[133]
JLF-1	JLF-1	600	1000	50.6	No	[103]
JLF-1	Ni	600	1000	208.7	Ni-Fe alloy layer on Ni	[103]
JLF-1	Nb	600	1000	−0.7	Nb particles on JLF-1	[103]

[a] Converted from weight loss of specimen by assuming uniform corrosion.

[127,133]. The concentration of Cr gradually decreased in the Ni-Cr layer from the surface to the inward, indicating the thermal diffusion of Cr into Ni container. Additionally, Cr_7C_3 on the graphite container was only detected from the tests with pure Cr metal [133] and higher Cr content alloys including Hastelloy X (Ni-21Cr-19Fe-9Mo), Haynes 230 (Ni-22.5Cr-14W-2Fe), and Inconel 617 (Ni-22Cr-12Co-10Mo-1Fe) [134], while no carbide layer was observed from the tests using lower Cr content Hastelloy N specimens [133,134].

All these experimental observations indicated that the enhanced corrosion of structural alloys and the simultaneous degradation of graphite or nickel components in the system may be caused by the interactions between structural alloys and graphite or nickel. Understanding the interaction mechanisms is important as structural alloys and graphite are the main components exposed to the primary salt in many MSR concepts (e.g., MSBR, MOSART, FHR, etc.). The plated Ni surface on structural alloys has also been proposed for the mitigation of material corrosion in molten fluorides [96]. The mechanisms that might be involved in this corrosion phenomenon are galvanic corrosion, direct reduction of corrosion products, and the disproportionation of Cr(II) to Cr(III) and metallic Cr. These three mechanisms are interpreted as follows:

(a) Galvanic corrosion

Galvanic corrosion may occur when a metallic material in an electrolyte (e.g., molten salt) is in contact with another dissimilar material. The metal with lower electrode potential acts as anode while the other acts as cathode. Both anode and cathode materials

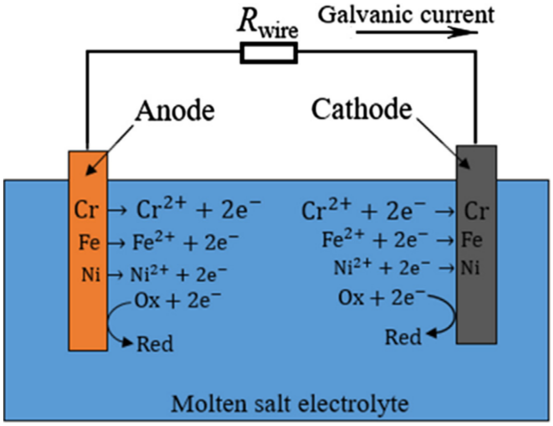

Fig. 12. Schematic of the direct reduction of the corrosion products on the cathode during galvanic corrosion. Ox represents the original oxidant impurities.

will be polarized to the same potential (if the resistance in metals is negligible) when they are in electrical contact. Thus, the corrosion of anode material will be accelerated due to the anodic polarization, i.e., positive overpotential. Meanwhile, the cathode material is cathodically polarized, increasing the reduction rate of the oxidants on the cathode material. For the metals with lower redox potential than the oxidants in the salt, the electrode potential is the corrosion potential of the metal in the salt. The corrosion potential of pure Ni in molten FLiNaK at 700 °C was found to be about 0.25 V and 0.5 V more positive than pure Fe and Cr, respectively [135]. For inert materials that have higher potential than the oxidant, the electrode potential is the redox potential of the oxidant in the salt. In most cases, graphite can be considered as a conductive inert material as its oxidation potential is higher than Ni in molten fluorides (e.g., the formal potential of $C/CF_4(g)$ is 0.32 V versus Ni/Ni^{2+} in FLiBe at 600 °C [61]). Thus, when the steels and Cr-bearing alloys are in contact with nickel or graphite, they will be polarized to a more positive potential. The polarization causes extra anodic dissolution of the steels and Cr-bearing alloys and simultaneously additional cathodic reduction of oxidant on the nickel or graphite, resulting in the generation of the galvanic current between the two materials. Wang et al. [135] found the corrosion current density of the Cr specimen in molten FLiNaK was increased by a factor of 81 when coupled with the same surface area Ni specimen. The factor for the increase of iron corrosion in Fe/Ni galvanic couple was 57 [135]. Therefore, the increased corrosion rate of pure Cr, Incoloy 800H, and JLF-1 steel specimens in the presence of graphite or nickel is at least partially attributed to the galvanic coupling effect. The Nb acts as the anode material when coupled with JLF-1 steel due to the lower oxidation potential of Nb (e.g., the formal potential of $NbO_2{}^+/Nb$ is −0.58 V versus Fe(II)/Fe in FLiBe at 600 °C).

(b) Corrosion of Cr by the direct reduction of Cr(II) on the cathode

The initial salt may contain some oxidizing impurities such as NiF_2, FeF_2, H_2O, and HF. In the galvanic corrosion case, these original impurities (Ox in Fig. 12) can be reduced on the cathode container. Considering the small amounts of salt used in these tests, these impurities should be exhausted quickly. Afterward, the corrosion would be ceased. However, the corrosion products such as Cr (II) released from the anode material can also be reduced on the cathode, causing persistent galvanic corrosion of Cr at the anode. The oxidation of Cr by Cr(II) sounds unlikely, but it occurs when the redox potential of Cr(II)/Cr is more positive at the cathode than at the anode. In the case of nickel cathode, the potential difference of Cr(II)/Cr can be expressed as $E^{\text{cathode}}_{\text{Cr(II)/Cr}} - E^{\text{anode}}_{\text{Cr(II)/Cr}} = \frac{RT}{nF}\ln\frac{a^{\text{anode}}_{\text{Cr}}}{a^{\text{cathode}}_{\text{Cr}}}$ according to Eq. (18). Hence, the reduction of Cr(II) to Cr at the nickel cathode is possible when the activity of Cr in the anode metal or alloy is greater than the activity of Cr in the cathode alloy. This agrees with the experimental finding of the Incoloy 800H/Ni couple observed from Olsen et al. [127], and the Cr/Ni couple observed from Qiu et al. [133]. The Cr fraction of anode materials Incoloy 800H and pure Cr were 0.225 and 1 respectively, which are significantly higher than the corresponding Cr fraction of 0.07 [127] and 0.16 [133] on the deposited Cr-Ni alloy layer on Ni containers. Although the activity coefficients of Cr in the cathode Ni-Cr alloys are unknown, it is reasonable to assume that the Cr activities in the cathodes were lower, based on the fraction comparisons.

In the case of graphite cathode, the reduction of Cr(II) to Cr_7C_3 at the cathode can be written as:

$$\text{Cathode: Cr(II)} + \frac{3}{7}\text{C} + 2e^- \rightarrow \frac{1}{7}\text{Cr}_7\text{C}_3 \tag{56}$$

At 700 °C, $\Delta G_f^\circ(CrF_2) = -648.1$ kJ/mol [71], and $\Delta G_f^\circ(Cr_7C_3) = -190.2$ kJ/mol [133]. The standard electrode potential of reaction (56) against standard F_2/F^- reference potential can be calculated by $\frac{1}{14F}\Delta G_f^\circ(Cr_7C_3) - \frac{1}{2F}\Delta G_f^\circ(CrF_2) = -3.22$ V at 700 °C. This is slightly positive than the standard electrode potential of Cr(II)/Cr which is $\frac{1}{2F}\Delta G_f^\circ(CrF_2) = -3.36$ V at 700 °C. Then, the actual potential difference can be expressed as $E^{\text{cathode}}_{\text{Cr(II)/Cr}_7\text{C}_3} - E^{\text{anode}}_{\text{Cr(II)/Cr}} = 0.14 + \frac{RT}{2F}\ln a^{\text{anode}}_{\text{Cr}}$ if the activity of Cr_7C_3 is assumed unity. Clearly, there exists a critical value of $a^{\text{anode}}_{\text{Cr}}$ above which Cr(II)/Cr_7C_3 potential at the cathode becomes more positive than the Cr(II)/Cr potential at the anode. Thus, the reduction of Cr(II) to Cr_7C_3 can occur on the graphite cathode when the activity of Cr in the anode material is higher than the critical value of 0.035 at 700 °C. This is supported by the emergence of Cr_7C_3 carbide layer on the graphite container that was coupled with pure Cr [133] and higher Cr content alloys such as Incoloy 800H, Hastelloy X, Haynes 230, Inconel 617, and Incoloy 800H [127,134], while no carbides were detected on the graphite container coupled with low Cr content Hastelloy N [134].

Therefore, in the case of galvanic coupling with graphite or nickel, a potential difference for Cr dissolution at anode and deposition at graphite or nickel cathode can be established, leading to a continuous reduction of Cr(II) at the cathode and dissolution of Cr at the anode metals or higher Cr content alloys. This allows the galvanic corrosion to proceed after the depletion of original oxidant impurities in the salt. The reduction of Fe(II) at the nickel container and dissolution of Fe in JLF-1 steel can occur in the same way.

(c) The disproportionation of Cr(II) to Cr(III) and metallic Cr

Carbides on graphite and Ni-Cr alloy on nickel may also be formed by the disproportionation reaction [136] in which the cation of the multivalent element with lower oxidant status may disproportionate to form the higher valence cation and metal:

$$3\mathrm{Cr(II)} \rightarrow 2\mathrm{Cr(III)} + \mathrm{Cr} \tag{57}$$

At 700 °C, $\Delta_r G = 40.5$ kJ/mol for reaction (57) [71], corresponding to $a_{cr}\,[a_{\mathrm{Cr(III)}}]^2/[a_{\mathrm{Cr(II)}}]^3 = 0.007$ at equilibrium. This indicates that the conversion of Cr(II) to Cr(III) and pure Cr is very low. However, if the Cr-Ni alloy or chromium carbides is formed instead of pure chromium as displayed by the reactions (58) and (59), the conversion ratio can be largely increased. At 700 °C, the ratio of $[a_{\mathrm{Cr(III)}}]^2/[a_{\mathrm{Cr(II)}}]^3$ becomes 0.1 for Cr-Ni alloy with Cr activity of 0.07. The $\Delta_r G$ is 13.2 kJ/mol for reaction (59) at 700 °C and the ratio of $(a_{\mathrm{Cr}^{3+}})^2/(a_{\mathrm{Cr}^{2+}})^3$ becomes 0.2 if Cr_7C_3 is formed instead of Cr.

$$\text{Ni cathode: } 3\mathrm{Cr(II)} \rightarrow 2\mathrm{Cr(III)} + \mathrm{Cr(Ni)_{alloy}} \tag{58}$$

$$\text{Graphite cathode: } 3\mathrm{Cr(II)} + \frac{3}{7}\mathrm{C} \rightarrow 2\mathrm{Cr(III)} + \frac{1}{7}\mathrm{Cr_7C_3} \tag{59}$$

In fact, the Cr deposition on nickel crucible [137] and vitreous carbon crucible [138] have been observed in molten FLiNaK with the addition of CrF_2. Peng et al. [138] reported 86.71–88.23% of the added CrF_2 (600–1300 ppm) in FLiNaK in vitreous carbon crucible was converted to CrF_3 as indicated by cyclic voltammetry. Hence, considerable amounts of Cr(II) may disproportionate to Cr (III) and Cr-Ni alloy or chromium carbides in nickel or graphite container.

Therefore, disproportion reaction of Cr(II) may occur on the graphite or nickel container surface, and the generated Cr(III) oxidant can then be transferred back to the specimen surface, causing the corrosion of alloy. This hypothesis was first proposed by Ozeryanaya [136] in molten chlorides and later adopted by Olsen et al. [127] in molten fluorides. Unlike the galvanic corrosion mechanism, the corrosion can still be accelerated by the disproportionation reaction mechanism in the case that alloy is isolated from the graphite or nickel. In the galvanic coupling case, Cr(III) produced by the disproportionation reaction can also be reduced to Cr(II) on the graphite or nickel container, further accelerating the galvanic corrosion rate.

4.2.4. Temperature gradient

Along the coolant circuit of a nuclear power conversion system, heat transfer from the primary coolant to the intermediate coolant induces a significant temperature gradient which may drive persistent long-term corrosion in the hotter region. The dependence of corrosion on temperature was observed from many ORNL loop tests. An example given in Fig. 13 shows the difference of corrosion attack at various temperature sections along the loop [123]. Typically, weight loss and severe void attacks occurred in the hot leg while weight gain during long-term exposure was observed in the cold leg.

More importantly, the weight gains at the cold sections were nearly equal to the weight losses at the hot sections, as shown in Fig. 14. As discussed earlier, the corrosion is expected to be terminated when the concentration of dissolved metal ions become sufficiently large, i.e., M^{n+}/M equilibrates with Ox/Red. However, the equilibrium concentrations of dissolved metal cations are dependent on temperature. The ORNL loop test results indicated the equilibrium concentration of chromium in a LiF-BeF_2-based fuel salt decreased from 2260 ppm at 800 °C to 1470 ppm at 600 °C [23]. It is expected that by prolonging the corrosion time, the dissolved metal ions such as Cr(II) in the melt will first reach equilibrium at the colder section. At this point, the corrosion of Cr at hot sections continues, and the released Cr(II) will be transferred within the molten salt fluid to cold sections. When Cr(II) exceeds the equilibrium concentrations at cold sections, deposition of Cr(II) to metallic Cr will occur, thus causing weight gains there. Considering the gradual decrease of Cr dissolution rate with time at hot sections, the system will be eventually balanced in a situation where the deposition rate at cold sections equals to the dissolution rate at hot sections. Then the corrosion rates and hot sections and deposition rates at cold sections might be maintained up to years as observed from the ORNL's long-term loop tests [19,101].

4.2.5. Flow velocity

During the ANP program, the flow velocity effects were investigated in forced-circulation loops under identical conditions with flow velocities of 1.06, 1.98, and 2.93 m/s, respectively [108]. The test material was Inconel 600, and the fuel salt was $50NaF$-$46ZrF_4$-$4UF_4$. The maximum depths of corrosion attack were ~100 at 1.06 m/s, ~75 at 1.98 m/s, and ~150 μm at 2.93 m/s, respectively. Hence, the effect of flow velocity on corrosion in molten fluorides appears to be insignificant. Comparison of the corrosion results of Inconel 600 obtained from the thermal-convection loops (Table 3) with the data collected from the forced-circulation loops (Table 5),

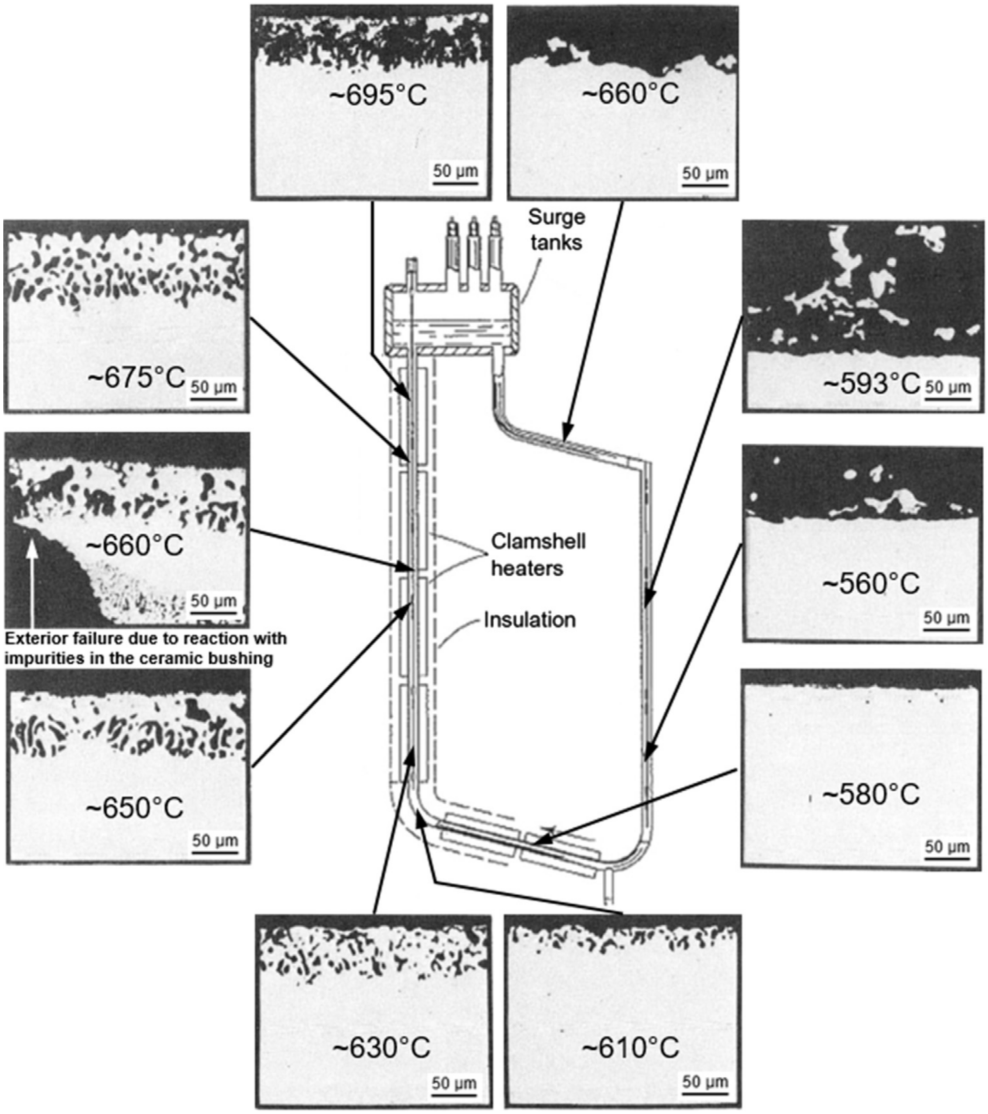

Fig. 13. Micrographs of Hastelloy N exposed to 70LiF-23BeF$_2$-5ZrF$_4$-1ThF$_4$-1UF$_4$ molten salt in a thermal convection loop after 9.2 years. Reproduced based on [123].

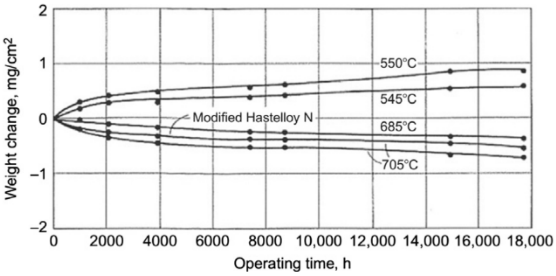

Fig. 14. Weight changes of Hastelloy N specimen at the hot and cold sections of one thermal convection loop [101].

also indicates that the influence of flow velocity seems to be minor. The flow velocity effect on corrosion of steel JLF-1 (Fe-9Cr-2W-0.1C) in FLiNaK was also investigated by Kondo et al. [86]. Tests were conducted in a static capsule and a container equipped with an impeller. The molten salt was stirred by the impeller at an estimated flow velocity of 0.17 m/s on the specimen surface. Under the dynamic condition, the weight loss of the specimen was similar to that in the static condition, but pitting corrosion was less intense. It was proposed that the flow suppressed the local condensation of oxidant impurities, thus reducing the localized attack.

4.2.6. Radiation

The radiation may interact with the corrosion process to cause further damage to the alloys. Neutron radiation damages the materials in two principal mechanisms [120]. First is the direct displacement of atoms caused by the collision with fast neutrons. Due to the high neutron energy of the fast neutron, its collision with a metal atom can kick off the metal atom, which will then strike many neighboring atoms out of their lattice position, generating vacancies and interstitials. Depending on the recoil energy of the kicked atoms, the collision cascade can occur, resulting in concentrated point defects in the local area. For the thermal neutron, the neutron energy is too low to cause direct displacements. However, the absorbed thermal neutron can generate impurity atoms by transmutation which then cause atomic displacement. The second mechanism specifically happens for the nickel-base alloys rather than nickel-free materials due to the transmutation of ^{58}Ni to ^{59}Ni (reaction (60)) and the subsequent (n, alpha) reaction (61) or (n, proton) reaction (62). The total number of atomic displacements produced from (n, alpha) and (n, proton) reactions are 1762 [139] and 222 [140] per neutron capture for ^{59}Ni, respectively. Thus, with the high thermal neutron absorption cross-section of ^{59}Ni [120], the atomic displacement damage from the thermal neutron capture is quite significant.

$$^{58}\text{Ni} + n \rightarrow {}^{59}\text{Ni} + \gamma \tag{60}$$

$$^{59}\text{Ni} + n \rightarrow {}^{56}\text{Fe} + {}^{4}\text{He} \tag{61}$$

$$^{59}\text{Ni} + n \rightarrow {}^{56}\text{Co} + \text{H} \tag{62}$$

Few reports investigate the effects of radiation on corrosion in molten fluorides. Zhu et al. [141] studied the influence of helium ion radiation on the corrosion of Hastelloy N (Ni-16Mo-6.4Cr-3.6Fe) in molten FLiNaK. One set of samples were exposed to a total flux of 0.5–1 × 10^{21} He-ions m^{-2} at approximately 0.2 × 10^{20} He-ions $\text{m}^{-2}\,\text{s}^{-1}$, while the other set had no helium ion irradiation treatment. Corrosion tests were then performed at 750 °C under argon atmosphere for 200 h. It was found that the irradiated samples suffered more severe intergranular corrosion attack and showed many small cavities in the grain matrix. The thickness of the depleted Cr/Fe zone increased to ~700 nm for the irradiated and corroded sample, compared to the value of ~20 nm for the corroded-only sample. Hence, it was evident that the existing damages of the samples caused by helium ion radiation significantly enhanced molten salt corrosion. Three aspects may account for the radiation-accelerated corrosion phenomenon: (a) the transmutation reactions of Ni decrease Ni content and also relatively increase the contents of less noble elements such as Fe and Cr in the alloy; (b) the radiation-induced surface cavities and ruptured cavities during recession of corroded surface increase the contact surface area with molten salt; (c) corrosion cavities can nucleate from the radiation-induced defects and defect clusters, and its growth can be accelerated by coalition with helium bubbles and diffusion of radiation defects. Therefore, the radiation can greatly accelerate the corrosion damage to the alloys. More experimental evidence, especially simultaneous corrosion and neutron radiation testing, are still needed.

4.2.7. Alloying elements and grain size

Corrosion resistance of existing alloys and the modified alloys with various element additives in molten fluorides has been compared by many researchers [101,105,122,124–126,142–144]. The major corrosion attacks on the tested alloys include the depletion of Cr sometimes together with Fe, the subsurface and intergranular voids, and IGC. The corrosion rate and the extent of localized attacks are subject to the alloy constituents and grain size. The resistance to Te-induced IGC was also related to the alloying element additives [121,122]. These effects are summarized as follows:

Chromium had a detrimental effect on the corrosion resistance as Cr is corroded more readily than Fe and Ni in molten fluorides. The increase in corrosion rate with the Cr content in the alloy is shown in Table 6, as well as the experimental results from Ouyang et al. [124], Sona et al. [126], DeVan [142], and Olsen et al. [143]. Generally, Ni-Mo alloy with less than 8 wt% Cr such as Hastelloy N, Hastelloy B, and Haynes 242 showed superior corrosion resistance on both weight loss and localized attack compared to the Inconel alloys, Hastelloy alloys, and stainless steels containing more than 15 wt% Cr. For these alloys containing > 15 wt% Cr, the dependence of corrosion attacks [124,143] especially the void attack depth on Cr content [105] became largely scattered, which might be attributed to the influence of other alloying elements. In comparison, DeVan [142] found the presence of other alloy constituents such as ≤3.1 mol% Al, ≤1.9 mol% Ti, ≤2.9 mol% Nb, and ≤5.6 mol% Fe had little influence on the Cr dissolution rate of Ni-17Mo alloys containing 3.2–11.0 mol% Cr. On the other hand, Cr content in the alloy influenced the resistance to Te-induced IGC. Additions of about 23 wt% Cr to nickel-base alloys reduced the Te-IGC attack, but additions of 15 wt% was not effective [121]. For example, Hastelloy S, Inconel 600 and Alloy 506 were cracked as severely as Hastelloy N [121].

Aluminum additions could be beneficial if the content was appropriate. DeVan [142] found the corrosion susceptibility of alloying additions increased in the order of Fe < Nb < V < Cr < W < Ti < Al. The dissolution rate of Al in Ni-Mo alloys containing more than 3 at% Al was about 1 order of magnitude higher than the dissolution rate of Cr in Ni-Mo alloys containing similar fractions of Cr. This is expected due to the more negative oxidation potential of Al than Cr. Experimental results from Misra et al. [105] also found the corrosion depth of the Inconel 702 containing 5.9 wt% Al was about 2–3 times larger than the Inconel 718 containing 1.3 wt% Al. However, if the Al content was less than 2 at%, little dissolution of Al was found because most Al additions formed highly stable compounds with interstitial contaminants in the Ni-Mo alloys [142]. The optimization of HN80MT at KI found the extent of the selective dissolution of Cr and the intergranular corrosion was minimized at an Al content of ~2.5 wt% [122]. The appropriate addition of Al with Ti could also improve the resistance to Te-induced IGC, and the optimized content for HN80MT alloy is 1–2 wt% of Al with 0.8–1.0 wt% of Ti [122]. The positive effect of Al on IGC resistance was because the carbide phase in the grain boundaries became less and discontinuous with the addition of Al, thus reducing the formation sites for the brittle intermetallic compounds.

Niobium additions to Hastelloy N were beneficial in reducing the tellurium embrittlement. The crack severity (described by the product of crack intensity and crack depth) highly depended on the Nb content. The least severe cracking was observed in alloys containing 1–2 wt% Nb [121]. Pure Nb corroded more readily than Cr in molten fluorides as demonstrated by the experiment results [103,144]. However, the comparison of Nb-modified Hastelloy N or HN80MT with their standard versions suggested the addition of approximately 2 wt% Nb did not increase the corrosion rate [121,122]. It appeared that the dissolution rate of Nb in Ni-Mo alloys containing less than 3.6 at% Nb was effectively inhibited by additions of Cr, Al, and Ti alloying elements [142].

Titanium fraction should be limited. The addition of Ti alone or with Al in Hastelloy N showed some beneficial influence on the resistance to radiation embrittlement and Te-induced IGC due to its influence on carbides formation. However, the content of free Ti in the alloy must be minimized. The oxidation potential of Ti is more negative than Cr (Fig. 1). Ni-Mo alloys with more than 2 at% Ti showed higher dissolution rate of Ti than the Cr dissolution rate in Ni-Mo alloys containing 5 at% Cr [142]. Unlike Nb, the dissolution rate of Ti was not decreased by presence of other alloying additives [142].

Small iron additions to nickel-based alloys were not harmful. ORNL and KI experience indicated the total removal of 2–5 wt% Fe from Hastelloy N or MONICR alloy [122] did not bring any detrimental effect. DeVan [142] found the dissolution rate of Fe in Ni-Mo alloys containing ~4–5.6 at% Fe was greatly inhibited by the presence of more reactive alloying elements such as Cr and Al in the alloy. However, the role of Fe became complex at higher contents of Cr. Table 6 shows the increase in corrosion rate with Fe fraction. Misra et al. [105] showed some iron-based alloys suffered less corrosion attack than the nickel-based alloys with similar Cr content and much less Fe content which contradicts the data in Table 6.

Cobalt-based alloys were more resistant than iron-based alloys probably due to the higher oxidation potential of Co (Fig. 1). Less corrosion attack of Co-based alloys H25 (Co-24.1Cr-10.7Ni-3.4Fe) and Haynes 188 (Co-28.2Cr-24.1Ni-1.7Fe) than the stainless steels with similar Cr and Ni content was observed [105]. However, replacing Fe additions by Co in Ni-based alloys was detrimental. Olson et al. [143] found the weight loss of Inconel 617 (Ni-22.1Cr-9.6Mo-12.4Co-1.1Fe) was two times more than that of Hastelloy X (Ni-21.3Cr-8.8Mo-19.3Fe-1.4Co).

Yttrium additions could increase the resistance to molten fluoride corrosion, Te-induced IGC, and air oxidation. The addition of appropriate amount of Y improved the corrosion resistance of Hastelloy N in molten FLiNaK [145]. The corrosion rate decreased by ~20% with the addition of 0.05 wt% Y, but increasing it above 0.10 wt% proved detrimental. The improved corrosion resistance at 0.05 wt% Y addition was attributed to the formation of a Y-rich layer near the alloy surface which probably acted as a barrier layer for the outward diffusion of Cr and Fe. At higher Y contents, most Y was consumed to form intermetallic $Ni_{17}Y_2$ and the Y-rich layer became absent. The addition of 0.01 wt% Y showed little effect on the resistant to Te-induced IGC [122]. But the addition of 0.05 wt% may have some impact, because the carbides (mainly MC_6) were dispersed more homogeneously in the form of small discrete particles on grain boundaries and grain matrix [146]. Further increasing of Y may become harmful as the MC_6 phase would change to coarse clusters. The addition of 0.05 wt% Y provided better resistance to air oxidation as well. Therefore, 0.05 wt% Y seemed an optimized content in considerations of resistance to molten fluoride corrosion, Te embrittlement, and air oxidation.

Molybdenum might have some beneficial effect. Liu et al. [125] found the corrosion attack of Inconel 600 was about 7 times deeper than that of Hastelloy C-2 which had similar Cr content but additional 15.49 wt% Mo. Ouyang et al. [124] found the pure Mo specimen suffered more weight loss than other Ni-Mo based alloys in molten FLiNaK, and depletion of Mo was observed from Hastelloy B3 [97]. This phenomenon was unexpected based on the higher oxidation potential of Mo than Ni and from the ORNL's findings during the ANP program. Considering the specimen was in contact with the nickel container or sample holder made of pure nickel, there might be a possibility that the contact caused the diffusion of Mo from pure Mo and high Mo-containing Hastelloy B3 to nickel container.

Tungsten might have no beneficial effect. Although the oxidation potential of W is more positive than Ni, Fe, and Cr, it was found W had a higher dissolution rate in Ni-Mo-W ternary alloys than Cr in Ni-Mo-Cr ternary alloys [142]. However, in the presence of other alloying elements such as Cr, Al, and Ti, the dissolution rate of W could be decreased by an order of magnitude [142]. The increase of W content with simultaneous decrease of Mo content showed no positive effect on resistance to both general corrosion [143] and Te-induced IGC [122].

Carbon probably had no effect on either the general corrosion or intergranular corrosion in molten fluorides. Olsen et al. [143] found a linear correlation between carbon content and the weight loss of several Ni-based alloys and Incoloy 800H possibly indicating that the intergranular corrosion in molten fluorides can be mitigated by decreasing C content or adding strong carbide forming elements. However, a careful review of the published corrosion data found no dependence on the C content. It is acknowledged that decrease of the carbon content or addition of strong carbide forming elements can improve the resistance of stainless steels and nickel-based alloys against intergranular corrosion in aqueous solutions. This is because the formation of the oxide layer is favored in aqueous solutions and Cr is beneficial to form the protective oxide layer. Hence, increasing the Cr content in the alloy improves the resistance of alloys to aqueous corrosion. As the formation of chromium carbides at the grain boundaries causes the depletion of Cr solute nearby (known as sensitization process), these Cr depleted zones become less corrosion resistant, resulting in severe intergranular corrosion. However, the corrosion in molten fluorides is active dissolution without the presence of oxide layers and increasing Cr content proves detrimental. This means the sensitization effect for intergranular corrosion in aqueous solution is not applicable for molten fluoride corrosion. Therefore, the resistance of intergranular corrosion in molten fluorides is likely not attributed to the C content in the alloy, and at least unrelated to the sensitization effect.

Effects of other elements including vanadium, manganese, rhenium, and silicon were considered. The dissolution rate of V in Ni-Mo alloys was higher than Fe but lower than Cr, and the selective dissolution and voids formation occurred in the same manner as Cr [142]. The addition of trace Mn significantly improved the IGC resistance, while the addition of Re showed little effect [122]. The addition of Si increased the amount of M_6C carbide in Hastelloy N [147] and the Si-enriched M_6C carbide particles offered more crack origins, resulting in reduced grain boundary strength.

The grain size also showed influence on the corrosion in molten fluorides. Wang et al. [95] refined grains of the Ni-Cr binary alloys (5–10 at% Cr) to ~3 μm by laser-remelting, from its original grain size ranging between 800 μm and 1500 μm. The weight loss after 100 h of exposure found that the grain refinement accelerated the corrosion rate by factors of 2–4. More subsurface voids and deeper Cr depletion zone were observed on the fine grain alloys. This was attributed to the higher effective diffusion rate of Cr with the decrease in grain size or increase in grain boundaries. The corrosion resistance of monocrystal and polycrystal N5 superalloy (Ni-7Cr-1.5Mo-5W-6.5Ta-6.2Al-3Re-0.15Hf) in molten FLiNaK salt were also investigated and compared [148]. The exposure of 100 h in FLiNaK resulted in a weight loss of ~17.0 mg/cm^2 and the 175 μm deep Cr/Al depletion zone for polycrystal N5 superalloy, compared to the values of 11.34 mg/cm^2 and 125 μm for monocrystal N5 superalloy. This indicated that both the general corrosion and localized attack depth were accelerated by the existence of grain boundaries in polycrystal N5 superalloy. ORNL's early study [108] showed little difference in the depth of the voids attack between the Inconel 600 consisted of grains in diameter of 22–90 μm (ASTM grain size 4–8) and the annealed Inconel 600 with grain diameter of 64–254 μm (ASTM grain size 1–5). Conversely, the voids in the coarse-grained alloy were more concentrated. A few relatively deeper intergranular voids were present in the coarsely grained alloy which might be related to the grain boundary orientations. Above results indicate that molten fluoride corrosion can be accelerated by the grain refining but remains largely unaffected for the smaller difference in grain size.

5. Materials corrosion in molten chloride salts

In the field of nuclear fuel recycling, molten chlorides are used as the process media for the EChem of the SNF. Recent molten salt fast reactor concepts also considered to use molten chlorides as fuel and coolant salts [149,150]. In addition to nuclear applications, molten chloride salts were also proposed as the thermal energy storage and heat-transfer fluids for next-generation concentrating solar power (CSP) [4,151–153]. Like fluoride salts, the corrosion of metals in molten chlorides is mainly driven by the oxidant impurities. In general, concentrations of impurities in the chloride salts used for EChem processes are higher than the salt coolants used for MSRs. During some of the EChem processes, strong oxidants such as O_2 and Cl_2 are generated or introduced into the system which cause the corrosion of structural materials. Their interactions with other impurities like water, oxides, and fission products make the system more complicated.

5.1. Major salt impurities during the EChem of SNF

The electrorefining technology is originally used for processing the spent metallic fuels. The electrolyte used for the electrorefining is LiCl-KCl eutectic salt. A metal basket containing chopped metallic fuel segments serves as the anode in the electrochemical cell. During the electrorefining, the applied current flows between the anode and cathode, resulting in the anodic dissolution of uranium at the anode and deposition of metallic uranium at the cathode:

$$\text{Anode: U} \rightarrow \text{U(III)} + 3e^- \tag{63}$$

$$\text{Cathode: U(III)} + 3e^- \rightarrow \text{U} \tag{64}$$

During electrorefining, impurities such as rare earth fission products in the spent metallic fuel are dissolved as soluble chlorides in the LiCl-KCl melt, which may serve as oxidants to the container metals.

For the spent oxide fuel (SOF) from the commercial light water reactors, recycling of the SOF can be performed by the electrowinning processing or the combination of electrolytic reduction and electrorefining. The electrolytic reduction was used to convert the SOF to its metallic form which can be further processed by electrorefining. The electrolytic reduction is typically operated in a LiCl molten salt with a low concentration of Li_2O at 650 °C [154]. Similarly, the spent oxide fuels are chopped and put in an inert metallic basket. The basket with spent oxide fuels works as a cathode while an inert material such as platinum can be used as the anode [155]. As a current is applied between the anode and cathode, actinide oxides are reduced to their metallic form at the cathode while O_2 is generated at the anode:

$$\text{Cathode: } MO_2 + 4e^- \rightarrow M + 2O^{2-} \tag{65}$$

$$\text{Anode(Pt): } 2O^{2-} \rightarrow O_2 + 4e^- \tag{66}$$

During the electrolytic reduction process, oxides of noble metal fission products and cladding are also converted to their metallic form along with actinide oxides while oxides of alkali metals, alkaline earth metals, and lanthanides will be dissolved as soluble chlorides in the electrolyte salt. The gaseous oxygen produced at the anode is a strong oxidant, and some lanthanides released from the SOF may act as oxidants to container metals.

Electrowinning is an alternative way to process SOF in which the final separated products are the oxides of U and Pu. In this process, the SOF is immersed into NaCl-KCl melt. The actinide oxides are separated from the SOF in several steps [9]: (1) Anodic dissolution of part of the UO_2 from SOF and simultaneous collection of UO_2 at the cathode by electrolysis; (2) Chemical dissolution of all remaining SOF by introducing Cl_2 gas in the molten salt; (3) Electrochemical reduction of noble metal fission products from the salt; (4) Final electro-deposition of UO_2 and PuO_2 with blowing $O_2/Cl_2/Ar$ mixture gas. Obviously, strong oxidants Cl_2 and O_2 are introduced in the salt during the electrowinning process.

The chloride salts after either electrorefining or electrowinning will be treated by the actinide drawdown and lanthanide drawdown. In the drawdown processes, the actinides and lanthanides are electrodeposited at the cathode, and oxidant Cl_2 is produced at the anode.

5.2. Influence of salt constituents and impurities

Disregarding the specific impurities during EChem, water is perhaps the most common oxidizing impurity in molten salts. Comparison of corrosion results in dry and moist molten chloride salts revealed that the corrosion was enhanced in the presence of moisture [150,156]. The reduction of water in molten chloride salts occurs according to reaction (33) [79]. The limiting cathodic current densities representing the maximum diffusion rates of H_2O from the bulk molten salt to the metal surface were identified from the polarization curves of iron and nickel in NaCl-KCl salt at 700 °C under various partial pressures of H_2O [157]. The increase in H_2O partial pressure resulted in the proportional increase of the limiting cathodic current densities corresponding to water reduction. On the other hand, the increase of the water vapor partial pressure also caused the increase of HCl in the molten chloride salt according to reaction (28). The produced HCl would also accelerate the corrosion by the reduction of dissociated H^+ [79]. For chloride salt with higher concentrations of O^{2-} such as the LiCl-Li_2O melt used for electrolytic reduction of SOF, reduction of OH^- (reaction (38)) may become considerable in addition to water reduction. The determined standard electrode potentials (vs. Cl_2/Cl^-) for the hydrogen evolution of H^+, H_2O, and OH^- in LiCl-KCl eutectic at 450 °C are −1.016 V, −1.900 V, and −2.603 V, respectively [79].

Oxygen gas is a strong oxidant in molten chloride salt. Corrosion of stainless steels and Inconel alloys in molten chloride salts under reactive atmospheres such as air or Ar-10% O_2 were significantly enhanced in comparison with the corrosion of the same materials under argon atmosphere [158–162]. The reduction of O_2 can proceed in two ways depending on whether the water is present in the system. The measured cathodic polarization curves on platinum in a dehydrated NaCl-KCl molten salt at 700 °C revealed a limiting cathodic current which increased linearly with the partial pressure of oxygen. The reduction of oxygen is believed to follow a two-step process in the absence of water as expressed by reactions (67) and (68), while the oxygen reduction is a one-step reaction in the presence of water (reaction (69)) [157]. The produced O^{2-} can react with dissolved metal ions to form oxide layers on the metal surface which may reduce the corrosion.

$$O_2 + 2e^- \rightarrow O_2^{2-} \tag{67}$$

$$O_2^{2-} + 2e^- \rightarrow 2O^{2-} \tag{68}$$

$$O_2 + 2H_2O + 4e^- \rightarrow 4OH^- \tag{69}$$

Chlorine gas can cause metal corrosion at very low concentrations, as indicated by the much more positive standard potential of Cl_2/Cl^- than oxidation potentials of metals (Fig. 2). Additionally, the increase of Cl_2 partial pressure also destabilizes the oxide film as indicated by the thermodynamic stability diagrams of M-O_2-Cl_2 system [163,164]. The formation of oxides is favored at higher O_2 partial pressure while chlorides become thermodynamically stable at the higher partial pressure of Cl_2. The stabilities of oxides and chlorides of metallic alloy elements are in the order of Cr > Mo ≈ Fe > Ni and Cr > Fe > Ni ≈ Mo, respectively [164].

Like molten fluoride salts, metallic cations such as Fe(III) are also the potential oxidants in the chloride salts. Enhanced corrosion of iron in molten KCl-LiCl eutectic due to the addition of $FeCl_3$ was reported by Colom and Bodalo [156]. In that study, the cathodic current density increased dramatically with the increase of $FeCl_3$ concentration, and the limiting current density corresponding to the maximum diffusion rate of Fe(III) was identified.

Some actinides and fission products such as U(IV), Np(IV), and Eu(III) may act as oxidants in molten chloride salts to cause metal corrosion, as indicated by the formal potentials in Table 2. In addition to the oxidizing capability, the oxide layers formed on the metal surface could be destabilized by the presence of chlorides of actinides and lanthanides in the melt, leading to the accelerated corrosion.

Hosoya et al. [150] investigated the corrosion of nickel-based superalloy Hastelloy-X in 50$NdCl_3$-5NaCl-45KCl molten salt. It was found that the native oxide layer consisting of NiO, $NiCr_2O_4$, and $NiFe_2O_4$ was stripped off by the reaction with $NdCl_3$:

$$NiO + NdCl_3 \rightarrow NiCl_2 + NdOCl \tag{70}$$

$$NiCr_2O_4 + NdCl_3 \rightarrow NiCl_2 + Cr_2O_3 + NdOCl \tag{71}$$

$$NiFe_2O_4 + NdCl_3 \rightarrow NiCl_2 + Fe_2O_3 + NdOCl \tag{72}$$

Corrosive HCl can also be produced by the reaction of $NdCl_3$ with residual moisture in molten chloride salts at high temperature:

$$NdCl_3 + H_2O \rightarrow NdOCl + 2HCl \tag{73}$$

Like $NdCl_3$, actinides and other lanthanides may also cause destabilization of the oxide layers by forming more stable oxy-chlorides. The E-pO^{2-} diagrams for actinides and lanthanides in molten chloride salts [81,165] indicated large stability regions of PuOCl, LaOCl, PrOCl, GdOCl, TbOCl, and HoOCl. Hence, oxide layers may be destabilized by these elements in chloride salts with wide ranges of O^{2-} concentrations.

Compared to other alkali chlorides and alkaline earth chlorides, the reduction potential of $MgCl_2$ is relatively more positive, as shown in Fig. 2. Results from ORNL flow loop tests with maximum temperatures of 494–575 °C showed higher corrosion rates for 347 and 410 stainless steels in NaCl-KCl-$MgCl_2$ eutectic salt than in LiCl-KCl eutectic salt [36]. Moreover, the corrosion rates in NaCl-KCl-$MgCl_2$ might be even higher as the temperatures of the NaCl-KCl-$MgCl_2$ loop tests were 70–120 °C lower than that of LiCl-KCl tests. Ambrosek [166] investigated the corrosion performance of Hastelloy X, Hastelloy N, Haynes 230, Inconel 600, Inconel 617, Inconel 625, Inconel 718, Inconel 800H, Ni-201, and 316 SS in 68KCl-32$MgCl_2$ (mol%) at 850 °C and found most of these alloys suffered from severe Cr dissolution and intergranular attack up to millimeters per year, indicating the corrosiveness of the $MgCl_2$-based salt. Wang et al. [152] studied the corrosion behaviors of pure nickel and nickel-based alloys GH4033 and GH4169 in molten 40NaCl-60$MgCl_2$ (mol%) salt at 520 °C [152]. The results showed the major corrosion products on the metal surface were MgO and Ni, which was attributed to the reduction of Mg(II) to metallic Mg followed by the reaction of Mg with NiO layer. Therefore, $MgCl_2$ might act as oxidant and destabilize the native oxide layer, leading to more severe corrosion in $MgCl_2$ containing salts.

5.3. Influence of oxide layers and alloying elements

Different from the bare metal corrosion in molten fluorides, the oxide corrosion products were typically formed on the metal surface in molten chloride salts. Corrosion products such as Cr_2O_3, NiO, Fe_2O_3, FeO, Fe_3O_4, and spinel-type oxides of $NiCr_2O_4$, $NiFe_2O_4$, and $FeCr_2O_4$ were characterized in the oxide layers formed on stainless steels and nickel-based alloys [16,158,159,162,167–169]. The formation of these oxides are expected in chloride salts with very low levels of oxygen contamination (e.g., 10^{-16}–10^{-42} atm for oxides of nickel, iron, and chromium depending on temperature [163,164,170]). However, the formation of a passivating oxide layer is much more challenging in molten chloride salts compared to aqueous solutions. Many experimental results showed the formed oxide layers on alloy surfaces are porous and non-passivating even under air or O_2-containing atmosphere [158,160,162,167]. Testing of nickel and iron electrodes in pure NaCl-KCl molten salt under air atmosphere showed no signs of passivity [170]. Even with the addition of $NaNO_3$ up to 0.1 mol% in the NaCl-KCl melt, stable passivation was not achieved on iron although a tendency to passivate was observed as indicated by the fluctuation of open circuit potential over a range of 200–300 mV with time. The potential fluctuation was attributed to the continual spalling and reforming of the oxide layers on the metal surface which was evidenced by the large black oxide particles in the melts [170]. The formation of a stable passive oxide layer highly depends on the concentration of the dissolved O^{2-} in the salt. The polarization of Fe, Co, Ni, Cu and Mo in molten LiCl-KCl eutectic containing 0.5 M Li_2O under helium atmosphere observed the anodic passivation zone in which the metal dissolution currents were significantly reduced [171]. The significant decrease of the metal dissolution current indicates the formation of a stable protective oxide layer in the passivation zone. However, the passivation zone was about 200–400 mV more positive than the corrosion potential and the metals were still under active dissolution at corrosion potential. Nishikata et al. [157] investigated the effects of O^{2-} on the anodic dissolution of metals by adding Na_2CO_3 in the NaCl-KCl molten salt. The anodic polarization curves indicated the occurrence of active metal dissolution, while a gradual decrease of anodic dissolution rates of nickel, iron, copper, silver, and platinum metals with the increase in Na_2CO_3 concentration was also observed. The inhibition of dissolution was attributed to the formation of oxide layers which was more favorable at higher O^{2-} concentrations. Although the oxide layers were not dense enough to cause anodic passivation phenomenon, they might slow down the anodic dissolution to some extent. However, it was also found the addition of Li_2O in LiCl molten salt would accelerate the corrosion of Cr-containing alloys due to the basic fluxing of the Cr_2O_3 layer by the basic oxide Li_2O. Cho et al. [172] investigated the corrosion of Incoloy 800H, KSA-4 (Fe-36Ni-8Cr), and KSA-5 (Fe-32Ni-29Cr) alloys in molten LiCl and LiCl-25 wt% Li_2O. The results showed the corrosion rate of alloys was significantly accelerated by additions of Li_2O in the salt. This was attributed to the reaction of Li_2O with Cr_2O_3 in the oxide layer which forms soluble chromate ions in the molten salt.

$$Cr_2O_3 + \frac{3}{2}O_2 + 2Li_2O \rightarrow 2Li_2CrO_4 \tag{74}$$

Hence the oxide layer became porous due to the removal of Cr_2O_3 by reaction (74) and corrosion was accelerated by additions of Li_2O. Argonne National Laboratory also investigated the corrosion of various alloys in molten LiCl-Li_2O salt [162]. Tests were carried out under Ar-10% O_2 atmosphere in LiCl salt containing 3.5 wt% Li_2O. All the specimens including two stainless steel and two Inconel alloys were completely corroded and dissolved in the molten salt after 30 days of immersion at 725 °C. Results obtained at 650 °C with a shorter exposure time of 6 days showed porous oxide layers on the stainless steels and Inconel alloys. Therefore, in addition to lanthanides and magnesium, the formation of passivating oxide layers in molten chlorides might be further challenged by the presence of Li_2O. In summary, oxide layers formed on metal and alloy surfaces were normally porous and non-passivating in molten chloride salts under typical conditions but still provided some protection to the underlying metals.

Shankar et al. [158,167,173] found that the oxide layers displayed as separate Cr-rich and Ni-rich layers, according to the microstructural examination of oxide layers formed on SS 316L (Fe-18Cr-12Ni), Incoloy 800H (Fe-20Cr-31Ni-1.5Mn), Inconel 600 (Ni-17Cr-10Fe-1Mn), Inconel 625 (Ni-18Cr-4Fe-11Mo), and Inconel 690 (Ni-30Cr-9Fe) in molten LiCl-KCl eutectic. It was assumed that the Cr-rich oxide layer formed first on the alloy surface since the oxidation potential of Cr was lower and Cr_2O_3 was more stable. When the outward diffusion rate of Cr was slowed down in the Cr depletion zone, Ni-rich oxide layer was formed underneath the Cr-rich oxide layer. Then the Cr- and Ni-rich layers grew in cycles, during which the spallation of the outermost layer could occur. This interpretation was somewhat supported by the different stacking sequence of Cr-rich and Ni-rich layers observed on the same alloys in different tests [158,162,167]. Future studies on the in-situ characterization of oxide layer evolution with time are required to improve the understanding.

Alloy elements influence the formation of oxide layers and play vital roles in the corrosion behavior of alloys in molten chloride salts. The major corrosion attacks for both the stainless steels and Ni-based alloys in molten chlorides are the depletion of Cr/Fe and subsurface voids underneath the oxide layers [16,158,159,162,169,174]. In general, nickel-based alloys showed better corrosion resistance regarding both weight loss and localized attack than stainless steels, as observed from many experimental studies [4,16,158,162,167]. An example is the superior corrosion resistance of Inconel alloys compared to SS 304, SS 316L, SS 347 and Incoloy 800H which have similar alloy compositions except for Ni and Fe [4,158,162]. The difference here can be attributed to the base metals by two aspects. First, iron is less noble than nickel and is corroded more rapidly. The other is the destabilization of oxide layers by the volatile iron corrosion products. The evaporation of corrosion products was proven by the decrease of total mass of molten LiCl-KCl salt and specimen inside the salt with time, as measured by thermogravimetric analysis [160]. The mass change due to evaporation of LiCl-KCl salt itself was calibrated with the blank salt. Compared to $NiCl_2$ (T_m = 1001 °C), $CrCl_2$ (T_m = 824 °C) and $CrCl_3$ (T_m = 1152 °C), either $FeCl_2$ (T_m = 306 °C) or $FeCl_3$ (T_m = 677 °C) is highly volatile at operation temperatures for typical molten chloride salts. Hence the evaporation of more volatile iron chlorides underneath and within the oxide layers might break through the oxide layers and leave behind pores in the layer. The continue evaporation of iron chlorides would also shift the equilibrium of reaction (42) which might cause the dissolution of formed iron oxides.

Furthermore, under conditions that nickel-based alloys only suffered from uniform transgranular voids [16,162] and Cr depletion [158], additional intergranular attacks were observed on austenitic stainless steels [16,158,162,175]. The intergranular corrosion in molten chloride salts may follow the same mechanism as in aqueous solution. Polovov et al. [175] investigated the resistance of stainless steels to intergranular corrosion in molten NaCl-KCl equimolar salt. Three austenitic stainless steels were tested, and the intensity of the intergranular corrosion increased in the order of AISI 321 (< 0.12C, 0.5–0.8Ti, in wt%) > AISI 316Ti (< 0.1C, 0.5–0.7Ti, 2.0–3.0Mo, in wt%) > AISI 316L (< 0.03C, 2.2–2.8Mo, in wt%). The results indicated the resistance to intergranular corrosion was improved by decreasing the carbon content and increasing the content of strong carbide forming elements. Hence, the susceptibility of intergranular corrosion was probably caused by the precipitation of chromium carbides and subsequent Cr depletion at grain boundaries, i.e., sensitization effect. This is to say that, the decrease of Cr content reduces the corrosion resistance at the grain boundaries. Increasing Cr content may benefit the formation of the protective Cr-enriched layer, which is supported by the lower corrosion resistance of carbon steel Q235A, and 9Cr-1Mo steel in molten chlorides than the stainless steels with higher Cr content [160,176]. On the other hand, the increase of corrosion rate with the increase in Cr content in alloys due to the selective dissolution of less noble Cr from the alloys was also reported in molten $LiCl-Li_2O$ [172]. Therefore, Cr plays a dual role in the alloy corrosion in molten chlorides, i.e., the beneficial effect on the formation of protective oxide layers and the detrimental effect on the aspect of Cr depletion.

Considering the dual effects of chromium additions, selection of appropriate content of Cr is important for alloy corrosion in molten chloride salts. Corrosion tests in molten LiCl-KCl eutectic indicated that alloys with intermediate Cr content such as Inconel 600 (Ni-17Cr-10Fe-1Mn) and Inconel 625 (Ni-18Cr-4Fe-11Mo) showed superior corrosion resistance compared to Inconel 690 (Ni-30Cr-9Fe) and pure nickel [158,167]. Vignarooban et al. [151] investigated the corrosion resistance of Hastelloy C-22 (Ni-22Cr-13Mo-3W-3Fe-2.5Co), Hastelloy C-276 (Ni-16Cr-16Mo-4W-5Fe-1Co), and Hastelloy N (Ni-7Cr-16Mo-5Fe) in $NaCl-KCl-ZnCl_2$ molten salt for solar applications. The results showed that the corrosion rate of Hastelloy C-276 was 3 times lower than Hastelloy N and slightly lower than Hastelloy C-22, indicating the optimized Cr content for Ni-based alloys was approximately between 7 wt% and 22 wt%. The presence of 3–4 wt% W in Hastelloy C-22 and Hastelloy C-276 might also have beneficial effects. Investigations of corrosion of electroformed pure nickel with and without Ni-20%W coating in molten LiCl-KCl indicated a better corrosion resistance of nickel with Ni-W coating due to the formation of W-rich NiO films [167].

Molybdenum is also an inert element but is detrimental in the case of high-temperature molten chloride corrosion. Shankar et al. [158,162] found the corrosion rate of Inconel 625 (Ni-18Cr-4Fe-11Mo) was remarkably higher than Inconel 600 (Ni-17Cr-10Fe-1Mn) in molten LiCl-KCl eutectic due to the presence of Mo in Inconel 625. This was attributed to the formation of low-melting MoO_3 (melting temperature T_m = 795 °C) which might break away from the oxide films [159]. Considering the higher melting point of WO_3 (T_m = 1473 °C) and similar oxidation potential of W and Mo, replacement of Mo by W in the alloy may improve the resistance to molten chloride corrosion.

Aluminum and titanium additions inhibit the corrosion in $MgCl_2$-based chloride salts by forming more stable oxides. Wang et al. [152] studied the corrosion mechanisms of nickel-based alloys in $40NaCl-60MgCl_2$ (mol%) and revealed the superior corrosion resistance of GH4033 (Ni-20.5Cr-4Fe-2.6Ti-0.8Al) due to the formation of a Ti- and Al-enriched oxide layer. Compared to Ni, Fe, and Cr, Ti and Al were oxidized more readily and formed stable oxides, which inhibited the metal dissolution and attack on grain and δ phase boundaries. Studies of Fe-Al model alloys in molten KCl showed that the dense alumina layer acted as an effective barrier to the penetration of the aggressive components and was stable in molten chloride salts [177]. Pre-oxidation treatment of alumina-forming alloys was proposed by Gomez-Vidal et al. [153] to mitigate the corrosion in molten $64.41KCl-35.59MgCl_2$ (mol%) salt. Inconel 702 (Ni-14 ~ 17Cr-2Fe-2.75 ~ 3.75Al), Haynes 224 (Ni-20.5Cr-27.6Fe-3.2Al), and Kanthal APMT (Fe-21Cr-5Al) were pre-oxidized and then tested at 700 °C under argon atmosphere up to 505 h. Results indicated that dense and uniform α-Al_2O_3 enriched layers were formed during the pre-oxidation treatment which protected the alloys from the molten salt attack. Comparing the performance of the tested alloys under various pre-oxidation conditions, Inconel 702 pre-treated in N_2-20%O_2 atmosphere at 1050 °C for 4 h showed the lowest corrosion rates. The alumina layers formed in Ar atmosphere were generally too thin. Hence, it was suggested to perform the pre-oxidation under cost-effective air atmosphere.

The silicon content should be limited below the solubility in the alloy. Cho et al. [178] studied the effect of Si on corrosion of N101 and N102 alloys in $LiCl-Li_2O$ molten salt and found increase of Si additions above 2 wt% reduced the corrosion resistance. The Si solubility in pure nickel is about 5 wt% but can be decreased to 2 wt% by the presence of other alloying elements such as Al and Ti. The excessive Si induced extensive segregation phases which initiated cracks in the oxide layers, resulting in the acceleration of corrosion.

6. Redox control to mitigate the corrosion

Redox control technique has been proposed to prevent the corrosion of structural materials in molten fluoride and chloride salts. The idea of the redox control is to introduce another redox couple RA^{k+}/RA^{j+} ($k > j$, RA stands for redox buffering agent) to make

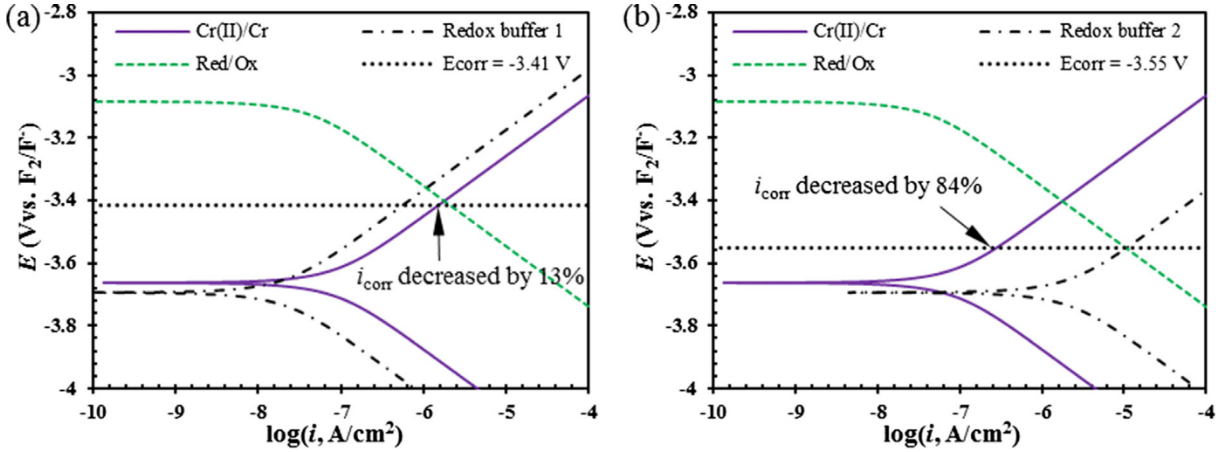

Fig. 15. Schematic polarization curves for chromium corrosion in the presence of a redox buffer with (a) low i_0 and (b) high i_0, respectively.

the salt less oxidizing. As discussed in Section 3.1, the corrosion of structural metals is an irreversible electrochemical process at a mixed/corrosion potential that deviates from the equilibrium potentials of the anodic and cathodic partial reactions. However, the equilibrium potentials of the partial electrode reactions will approach an intermediate value with the increase of the product concentrations and consumption of the oxidants with time. Hence the overall corrosion reaction tends to reach an equilibrium where corrosion will be stopped:

$$M + Ox \leftrightarrow M^{n+} + Red \tag{75}$$

If a redox buffering agent RA^{k+}/RA^{j+} is introduced in the system, the equilibrium of reaction (75) will be influenced by the following two reactions:

$$RA^{j+} + Ox \leftrightarrow RA^{k+} + Red \tag{76}$$

$$M + RA^{k+} \leftrightarrow M^{n+} + RA^{j+} \tag{77}$$

In the thermodynamic consideration, the equilibrium of reaction (75) can be pushed to the left by keeping the concentration ratio of RA^{k+}/RA^{j+} sufficiently low. Hence, the concentration of M^{n+} can be thermodynamically limited by controlling the concentration ratio or redox potential of RA^{k+}/RA^{j+}. However, the influence of RA^{k+}/RA^{j+} to reaction (75) could be very limited if the two RA^{k+}/RA^{j+} related reactions are relatively slow. Moreover, corrosion is an irreversible electrochemical process before reaching such equilibrium. Therefore, it is always valuable to consider the effects of redox control on metal corrosion from the kinetics aspect. Fig. 15 shows the kinetics of reactions occurring on a corroded metal surface in a redox control system that contains a metal M, an oxidizing impurity Ox, and a redox buffering agent RA^{k+}/RA^{j+}. All electrochemical parameters except the exchange current density of RA^{k+}/RA^{j+} are the same in Fig. 15a and b. The corrosion potential where the net current is zero is indicated by the horizontal line. It is seen that the inhibition of corrosion by introducing RA^{k+}/RA^{j+} with lower i_0 in the system is very limited. By increasing the i_0 of RA^{k+}/RA^{j+} (Fig. 15b), the negative shift of corrosion potential becomes more pronounced. At this corrosion potential, oxidation rate of RA^{j+} is several orders of magnitude higher than the dissolution rate of metal M. This means most oxidants will be consumed by the oxidation of RA^{j+} rather than the corrosion of metal. In other word, RA^{j+} acts as a sacrificial material to protect the metal. In addition to the exchange current density, charge-transfer coefficient and diffusion coefficient also affect the sacrificial effect of redox buffers. Back to the thermodynamic consideration, the redox potential of RA^{k+}/RA^{j+} should be controlled below the oxidation potential of M to avoid the corrosion by RA^{k+} after the consumption of the oxidizing impurities. Therefore, the redox control system requires a redox buffer RA^{k+}/RA^{j+} with higher i_0 and lower redox potential. The control of the redox potential can be performed by adjusting the concentration ratio of RA^{k+}/RA^{j+} which may change with time due to the reaction with oxidants in the molten salt.

Redox control can be performed through gas phase control (e.g., HF/H_2), major metal control (e.g., Be(II)/Be), and dissolved salt control (e.g., U(IV)/U(III)) [13]. Gas phase control was successfully used to change the salt redox conditions (i.e., salt purification in Section 3.2.6) but the application in the MSRs was challenged due to the impact on the tritium processing systems and potentially larger volume of radioactive waste. Compared to major metal control, dissolved salt control is relatively more attractive as the soluble RA is uniformly dispersed in the entire molten salt systems and will not cause the formation of intermetallic compounds with container metals.

In the MSRE, minor corrosion of the structural components was observed which might be attributed to the lower U(IV)/U(III) concentration ratio in the fuel salt. It was recommended to control the concentration ratio of U(IV)/U(III) in the ranges of 50–143 for MSRE fuel salt and 10–100 for $72LiF\text{-}16BeF_2\text{-}12ThF_4$ salt based on the thermodynamic calculations [48,61]. A concentration ratio above the upper limit would cause considerable corrosion of chromium while a ratio below the lower limit might form uranium carbides in systems containing graphite components [48,61]. From the aspect of electrode kinetics, U(IV)/U(III) is also feasible as a redox buffering agent due to its higher exchange current density than metal dissolution reactions (Fig. 4).

As UF_3 would be consumed by the reactions with oxidizing impurities, the ratio of UF_4/UF_3 in the MSRE fuel salt was maintained to values around 100 by contacting the salt with beryllium metal in the reactor's sample system on a weekly or monthly basis [48]. The redox potential of Be(II)/Be is more negative. Hence, the U(IV) can be reduced to U(III) by the oxidation of beryllium metal:

$$\mathrm{Be} + 2\mathrm{U(IV)} \rightarrow \mathrm{Be(II)} + 2\mathrm{U(III)} \tag{78}$$

The possibility of using metallic uranium instead of beryllium to control the concentration ratio of U(IV)/U(III) was recently investigated for the application of redox control in MSFR [179]. The evolution of U(IV)/U(III) concentration ratio after the immersion of U plate in LiF-CaF_2-UF_4 melt was monitored by cyclic voltammograms. The concentration ratio decreased from infinite to 1 in 2.5 h due to the 3U(IV) + U ↔ 4U(III) reaction, showing the feasibility of using U as reducing agent.

In MSRs' intermediate coolant systems, redox couple Eu(III)/Eu(II) was proposed to prevent the corrosion of structural metals [47]. It was found that the transformation between Eu(III) and Eu(II) was reversible, indicating higher reaction rate constants. The comparison of the measured formal standard potentials of Eu(III)/Eu(II) with oxidation potentials of Cr indicated that the corrosion of chromium can be mitigated by controlling the Eu(III)/Eu(II) concentration ratio below 0.05. Furthermore, the deposition of metallic Eu when the salt is over-reduced is not likely as the potential of Eu(II)/Eu was more negative than the potassium deposition potential of FLiNaK. In this study, the measurements of Eu(III)/Eu(II) concentration ratio using voltammograms and the dynamic reference electrode for the redox sensor were also demonstrated. Hence the online monitoring of the salt redox condition can be quickly performed by electrochemical measurements using the redox sensor. The approach of controlling of the Eu(III)/Eu(II) concentration ratio by contacting the fluoride melt with reductive metals was also validated [179]. Sm(III)/Sm(II) and Yb(III)/Yb(II) are also possible couples for dissolved salt control, as indicated by their formal potentials in Table 2. For the dissolved salt control in the primary coolant of salt-cooled reactors, candidates should also exhibit low neutron absorption, and no acceptable multivalent redox couple has been found so far [31].

The major metal control method was also studied in molten fluoride salts. ORNL investigated the corrosion rate of stainless steel 316 in FLiBe salt with and without additions of beryllium metal [180]. As shown in Fig. 16, without the addition of beryllium metal, the weight loss was decreased rapidly in the first 1000 h probably due to the impurities in the "as received" salt. This was followed by the thermal-gradient driven corrosion with a rate of ~8 µm/y after 3000 h. In comparison, the beryllium addition significantly reduced the corrosion rate to less than 2 µm/y as indicated by the upper curve.

Later during the JUPITER-II fusion program, beryllium metal control method was further studied for corrosion prevention in FLiBe blanket coolant [181–183]. In fusion blankets, corrosive tritium fluoride is generated by the reaction of neutrons with LiF. In these tests, He/H_2/HF gas mixture was bubbled through the molten salt in a sealed container with a simulated HF flow rate while the HF concentration in effluent gas was measured using an autotitrator. Calderoni et al. [181] investigated the effect of beryllium addition on the corrosion of reduced activation ferritic/martensitic steel JLF-1 (89Fe-9Cr-2W) in FLiBe. The ICP analysis of the salt showed the dissolved Cr and Fe in the salt were remarkably reduced during the short immersion of beryllium rod in the melt. This was attributed to the sacrificial effect of beryllium metal as indicated by the significant decrease of HF concentration in the effluent gas stream during beryllium addition and the substantial corrosion of beryllium rod. Even after the extraction of beryllium rod, it took a long period for the HF to recover to the original concentration. Depending on the immersion time and HF flow rate, this recovery time could vary from several hours to 50 h. One example of the lagging effect of HF recovery after beryllium addition is given in Fig. 17 [182]. A simple kinetic model was also developed to calculate the dissolution rate of beryllium and transformation rate of HF to H_2 [183]. The calculations indicated that the beryllium metal control would be able to keep the TF concentration in the melt below 0.02 ppb under which condition the corrosion of structural metals should be negligible [183].

Compared to the dissolved salt control, the buffering capability of the major metal control in the entire MSR coolant loop was questioned as the effect might be inadequate in locations far away from beryllium addition [13,23]. However, the presence of soluble Be^0 with adequate solubility in FLiBe was found during JUPITER-II. Hara et al. [184] dissolved the Be-rod-contacted FLiBe salt samples in acid solutions and measured the amount of hydrogen gas generated by the reaction of Be^0 with acid. The corresponding Be^0 concentration in FLiBe was in the range of 0.099–0.76 mol%. This concentration was in the same order of magnitude compared to

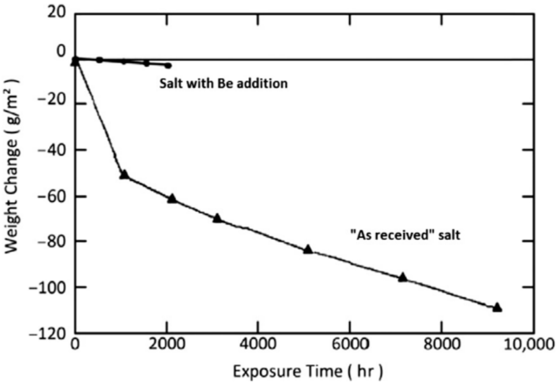

Fig. 16. Weight loss of 316 stainless steel at the hot section (650 °C) of a convection loop in FLiBe salt showing the corrosion inhibition by the addition of beryllium metal in the salt [180].

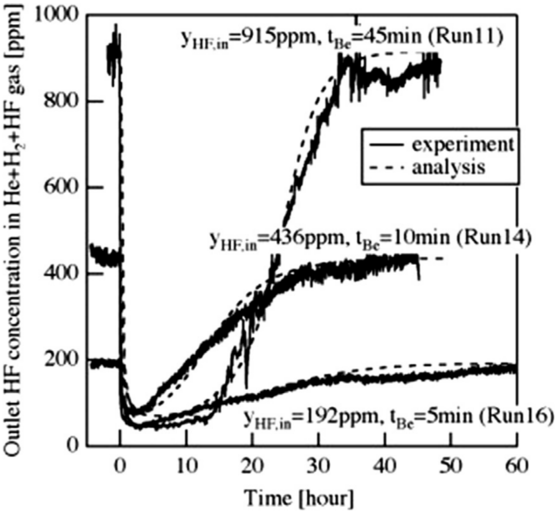

Fig. 17. Measured and calculated outlet HF concentration after various immersion times of beryllium metal in the FLiBe molten salt [182].

the total uranium fluorides in MSRE fuel salt. Hence, the solubility of Be^0 might be adequate for redox control. The application of major metal control in molten chloride salts such as Mg in $MgCl_2$-KCl salt [185] was also promoted by recent interest in the use of molten chloride salts in MSRs and solar applications. Zirconium metal was also proposed as redox buffering agent in non-beryllium fluoride salt systems. However, the formation of a coating composed of Ni/Zr intermetallic compounds was reported in FLiNaK system using zirconium metal as a redox buffer [186]. The salt might also become too reducing to cause the formation of ZrC particles in the presence of graphite [186]. Therefore, in addition to the corrosion control capability, the feasibility of using major metal control in the new salt systems should be carefully demonstrated to avoid other material compatibility problems.

7. Conclusions and outlook

This review covers key areas of materials corrosion and related materials issues in typical molten salts used in nuclear engineering fields. The roles of the alloy composition, salt chemistry, and environmental factors involved in various nuclear applications are discussed, based on which recommended areas for additional research to further understand the corrosion mechanisms and the development of corrosion-resistant alloys are proposed. The conclusions for the material corrosion in molten fluorides and chlorides are presented below.

Materials corrosion in molten fluorides is in the form of bare alloy dissolution driven by the oxidants in the salt. The thermal gradient driven corrosion is inevitable in the MSR circuits. Thus the corrosion rate at hot sections must be minimized to avoid the clogging problems at cold sections specifically for heat exchangers. Depletion of chromium with subsequent formation of voids in the regions near the alloy surface and along the grain boundaries are typical corrosion attacks on Cr-bearing alloys. As alloy corrosion is predominated via the selective dissolution of chromium, the chromium content in the alloys must be reduced. However, the decrease of Cr content also lowers the resistance to air oxidation. The optimized Cr content is 6–8 wt% in consideration of the resistance to both molten salt corrosion and high-temperature air oxidation. The Ni-Mo alloys with a major composition of Ni-11 ~ 13Mo-6 ~ 8Cr are promising candidate materials for molten fluoride salt reactor concepts. Future alloy metallurgical modifications aiming at the mitigation of Cr depletion should focus on lowering the Cr diffusion coefficient, especially the intergranular diffusion. There are current works on the surface treatment or multilayer composite with a diffusion barrier layer for Cr which is an alternative option [96,187]. Three other material degradation issues are Te-induced IGC, irradiation embrittlement, and radiation damages. For the salt-fueled MSRs, resistance to Te-induced IGC must be considered. Fission product Te diffuses preferentially along the grain boundaries and causes IGC by the formation of brittle metallic tellurides on grain boundaries. The formation of these telluride compounds is probably by the reactions of Te with the alloy elements Ni and Cr. Although the mechanisms still require further verification, there exist two options to reduce the Te-induced IGC. The first option is to minimize the preferential formation sites (e.g., intergranular carbides) for tellurides by alloy modifications. The improved resistance of Hastelloy N to the Te-induced IGC by adding 1.5 wt% Nb alone or 1–2 wt% of Al with 0.8–1.0 wt% of Ti is encouraged for the future development. The other option is to reduce the Te to its negative oxidation states in the salt by controlling the salt redox condition. To improve the resistance of Ni-based alloys against irradiation embrittlement, additions of alloying elements to form finely dispersed carbides within the grains have been found to be effective. Experiments have shown that the radiation damage greatly accelerates the corrosion of alloy exposed to molten fluoride salts. The resistance of Hastelloy N to damages caused by simultaneous thermal neutron radiation and molten salt corrosion seems adequate based on MSRE experience. However, related studies are very limited, and the synergistic effect of fast neutron radiation damage and molten salt corrosion attack must be investigated for recent fast spectrum MSR concepts.

Corrosion is significantly accelerated by the presence of oxidizing impurities in the fluoride salts. These impurities include the water contaminant, initial metallic impurities, residual HF after salt purification, ingress of impurities from the MSR environment, corrosion products, actinides as well as the fission and transmutation products. The potential erosion-corrosion of the structural alloys by the presence of solid oxides impurities in the flowing molten salt coolant in MSR loops is also a concern which has not been verified. Redox control is an online technique to mitigate the material corrosion by maintaining a reducing salt redox condition. The oxidizing impurities will be primarily consumed by the redox buffering agent. The dissolved salt control and major metal control are promising options for redox control in MSRs. Future efforts should be made on the aspects of kinetics and online measurements. Modeling the corrosion of structural materials in molten fluorides is important for the safe operation of MSRs. A simplified model by incorporating the electrochemical corrosion module with the heat and mass transfer simulation has been developed to predict the local corrosion rate in solar molten salt systems [188]. Compared to solar systems, nuclear molten salt systems are more complicated due to the variety of oxidants, radiation, and fission product embrittlement. A comprehensive model has not been developed because of the lack of fundamental data such as electrochemical parameters for typical oxidants in nuclear molten salt systems. The model should also be capable to predict the alloy depletion and voids formation in the alloy which might be simulated by molecular dynamics and kinetic Monte Carlo methods.

Material corrosion in molten chlorides highly depends on the salt impurities and alloy compositions. Due to the presence of chlorine ions and other species such as Li_2O and cations of magnesium and lanthanides, formation of passivating oxide layers as in the aqueous system is typically not practical in molten chlorides. The formed oxide layers on the alloy surface are normally porous and spalled in molten chloride salts. However, the oxide layers still provide some protection to the underlying metals. The corrosion attack appears as depletion of Cr in the alloy matrix underneath the oxide layer and the intergranular corrosion. Different from the alloy development strategy in molten fluorides, alloy modifications in molten chlorides should not only consider the alloy depletion but more importantly the influence on the oxide layer properties. Cr additions benefit the formation of protective oxide layers but accelerate the Cr depletion in the alloy. The optimized Cr content is approximately between 7 wt% and 22 wt%. Nickel-based alloys showed better corrosion resistance than iron-based alloys probably because iron forms highly volatile chlorides which destabilizes the oxide layers. Mo should also be minimized due to the formation of low-melting MoO_3. Si content should be limited below the solubility to avoid the formation of segregation phases which initiate cracks in the oxide layer. Al additions in the alloys form more protective and stable α-Al_2O_3 which improves the corrosion resistance. The resistance of alumina forming alloys can be further improved by high-temperature pre-oxidation treatment. The intergranular corrosion in molten chlorides perhaps follows the same mechanism as in aqueous solutions. Hence the resistance to the intergranular corrosion can be improved by the decrease of the C content and/or the addition of strong carbides forming elements.

Acknowledgements

This work was supported by NEUP Award Number DE-NE0008306. Any opinions, findings, conclusions, or recommendations expressed in this publication are those of the authors and do not necessarily reflect the views of the U.S. Department of Energy Office of Nuclear Energy. The authors thank Mr. Ryan Chesser at Virginia Tech for checking the English and providing useful comments.

References

[1] Giordani V, Tozier D, Tan H, Burke CM, Gallant BM, Uddin J, et al. J Am Chem Soc 2016;138:2656–63.
[2] Swinkels DAJ. Molten salt batteries and fuel cells. Braunstein J, Mamantov G, Smith GP, editors. Advances in molten salt chemistry, vol. 1. US: Springer; 1971. p. 165–223.
[3] Marcus Y. Liquid extraction from molten salts. Braunstein J, Mamantov G, Smith GP, editors. Advances in molten salt chemistry, vol. 1. US: Springer; 1971. p. 63–172.
[4] Gomez-Vidal JC, Tirawat R. Sol Energy Mater Sol Cells 2016;157:234–44.
[5] Goff M. Non-aqueous processes. Presentation at "Introduction to nuclear fuel cycle chemistry"; 2009.
[6] Nutt WM, Hill RN, Bulen DB. Waste Manage (Oxford) 1995;15:629–39.
[7] Li SX, Johnson TA, Westphal BR, Goff KM, Benedict RW. Electrorefining experience for pyrochemical reprocessing of spent EBR-II fuel. In: Proceeding of GLOBAL 2005, Tsukuba, Japan; 2005. Paper no. 487.
[8] Sakamura Y, Kurata M, Inoue T. J Electrochem Soc 2006;153:D31–9.
[9] Sato F, Fukushima M, Myochin M, Namba T, Kormilitsyn MV, Ishunin VS, et al. J Phys Chem Solids 2005;66:675–80.
[10] Assessment of Partitioning Processes for Transmutation of Actinides. IAEA-TECDOC-1648. Vienna, Austria: International Atomic Energy Agency; 2010.
[11] Williamson MA, Willit JL. Nucl Eng Tech 2011;43:329–34.
[12] Generation IV Roadmap Crosscutting Fuels and Materials R&D Scope Report, GIF-010-00, Issued by the Nuclear Energy Research Advisory Committee and the Generation IV International Forum; 2002.
[13] Olander D. J Nucl Mater 2002;300:270–2.
[14] Petti DA, Smolik GR, Simpson MF, Sharpe JP, Anderl RA, Fukada S, et al. Fusion Eng Des 2006;81:1439–49.
[15] Zhang J, Li N. J Nucl Mater 2008;373:351–77.
[16] Hofmeister M, Klein L, Miran H, Rettig R, Virtanen S, Singer RF. Corros Sci 2015;90:46–53.
[17] Delpech S, Cabet C, Slim C, Picard GS. Mater Today 2010;13:3–41.
[18] Ignatuev V, Surenkov A. Material performance in molten salts. In: Konings RJM, editor. Comprehensive nuclear materials, vol. 5. Elsevier Ltd.; 2012. p. 221 – 50.
[19] Sridharan K, Allen TR. Corrosion in molten salts. In: Lantelme F, Groult H, editors. Molten salts chemistry: from lab to applications. Elsevier Ltd.; 2013. p. 241 – 67.
[20] Nourry C, Souček P, Massot L, Malmbeck R, Chamelot P, Glatz J-P. J Nucl Mater 2012;430:58–63.
[21] Gibilaro M, Massot L, Chamelot P, Taxil P. J Nucl Mater 2008;382:39–45.
[22] Taxil P, Massot L, Nourry C, Gibilaro M, Chamelot P, Cassayre L. J Fluorine Chem 2009;130:94–101.
[23] Williams DF, Toth LM, Clarno KT. Assessment of candidate molten salt coolants for the advanced high-temperature reactor (AHTR), ORNL/TM-2006/12. Oak Ridge, TN, USA: Oak Ridge National Laboratory; 2006.
[24] Beneš O, Konings RJM. Molten salt reactor fuel and coolant. In: Konings RJM, editor. Comprehensive nuclear materials, vol. 3. Elsevier Ltd.; 2012. p. 359 – 89.
[25] Haubenreich PN, Engel J. Nucl Appl Technol 1970;8:118–36.

[26] Robertson RC. Conceptual design study of a single-fluid molten-salt breeder reactor, ORNL-4541. Oak Ridge, TN, USA: Oak Ridge National Laboratory; 1971.
[27] Ignatiev V, Feynberg O, Gnidoi I, Merzlyakov A, Surenkov A, Uglov V, et al. Ann Nucl Energy 2014;64:408–20.
[28] Doligez X, Heuer D, Merle-Lucotte E, Allibert M, Ghetta V. Ann Nucl Energy 2014;64:430–40.
[29] Southern Company subsidiary awarded grant to lead advanced nuclear technology development. <http://www.southerncompany.com/newsroom/2016/jan-2016/2016-01-15-so-nuclear-technology.html> [accessed 5/29/2018].
[30] Mourogov A, Bokov PM. Energy Convers Manage 2006;47:2761–71.
[31] Holcomb DE, Flanagan GF, Mays GT, Pointer WD, Robb KR, Yoder Jr GL. Fluoride salt-cooled high-temperature reactor technology development and demonstration roadmap, ORNL/TM-2013/401. Oak Ridge, TN, USA: ORNL; 2013.
[32] Poulson B. Corros Sci 1983;23:391–430.
[33] Janz GJ. Molten salt handbooks. New York-London: Academic Press; 1967.
[34] Janz GJ, Gardner GL, Krebs U, Tomkins RPT. J Phys Chem Ref Data 1974;3:1–115.
[35] Janz GJ, Tomkins RPT, Allen CB, Downey Jr JR, Garner GL, Krebs U, et al. J Phys Chem Ref Data 1975;4:871–1178.
[36] Williams DF. Assessment of candidate molten salt coolants for the NGNP/NHI heat-transfer loop, ORNL/TM-2006/69. Oak Ridge, TN, USA: Oak Ridge National Laboratory; 2006.
[37] Øye HA. Modeling of thermodynamic data. In: Gaune-Escard M, editor. Molten salts: from fundamentals to applications. Kluwer Academic Publishers; 2002. p. 179–211.
[38] Sangster J, Pelton Ad. J Phys Chem Ref Data 1987;16:510–61.
[39] Hong KC, Kleppa OJ. J Phys Chem 1978;82:1596–603.
[40] Gal IJ, Paligorić I. J Chem Soc, Faraday Trans 1982;78:1993–2003.
[41] Fukuda GT, Peterson PF, Olander DR, Prausnitz JM. Fluid Phase Equilib 2007;255:1–10.
[42] Olander DR, Fukuda GT, Bases Jr CF. Fusion Sci Technol 2002;41:141–50.
[43] Hitch BF, Baes Jr CF. Inorg Chem 1969;8:201–7.
[44] Pelton AD, Chartrand P. Metall Mater Trans A 2001;32:1355–60.
[45] Beneš O, Konings RJM. J Chem Thermodyn 2009;41:1086–95.
[46] Pelton AD, Chartrand P. Metall Mater Trans A 2001;32:1361–83.
[47] Guo S, Shay N, Wang Y, Zhou W, Zhang J. J Nucl Mater 2017;496:197–206.
[48] Toth LM, Del Cul GD, Dai S, Metcalf DH. AIP Conf Proc 1995;346:617–26. http://dx.doi.org/10.1063/1.49142.
[49] Zhang J. J Nucl Mater 2014;447:271–84.
[50] Baes Jr CF. The chemistry and thermodynamics of molten-salt-reactor fluoride solutions. In: Thermodynamics. vol. I. Proceedings of the symposium on thermodynamics with emphasis on nuclear materials and atomic transport in solids. Vienna, Austria: International Atomic Energy Agency; 1966. p. 427.
[51] Forsberg CW, Lam S, Carpenter DM, Whyte DG, Scarlat R, Contescu C, et al. Nucl Technol 2017;197:119–39.
[52] Massot L, Chamelot P, Taxil P. Electrochim Acta 2005;50:5510–7.
[53] Gibilaro M, Massot L, Chamelot P, Cassayre L, Taxil P. Electrochim Acta 2014;147:114–20.
[54] Nourry C, Massot L, Chamelot P, Taxil P. Electrochim Acta 2008;53:2650–5.
[55] Chamelot P, Massot L, Hamel C, Nourry C, Taxil P. J Nucl Mater 2007;360:64–74.
[56] Straka M, Szatmáry L. Procedia Chem 2012;7:804–13.
[57] Straka M, Korenko M, Lisý F, Szatmáry L. J Rare Earths 2011;29:798–803.
[58] Huang W, Tian L, She C, Jiang F, Zheng H, Li W, et al. Electrochim Acta 2014;147:114–20.
[59] Kuznetsov SA, Hayashi H, Minato K, Gaune-Escard M. J Electrochem Soc 2005;152:C203–12.
[60] Martinot L. Molten salt chemistry of actinides. In: Freeman AJ, Keller C, editors. Handbook on the physics and chemistry of the actinides, vol. 6. Elsevier Science B.V.; 1991. p. 241 – 79.
[61] Baes Jr CF. J Nucl Mater 1974;51:149–62.
[62] Masset P, Apostolidis C, Konings RJM, Malmbeck R, Rebizant J, Serp J, et al. J Electroanal Chem 2007;603:166–74.
[63] Babaian R, Hill DL, Bailey RA. J Electrochem Soc 1965;112:1221–4.
[64] Caravaca C, de Cordoba G, Tomas MJ, Rosado M. J Nucl Mater 2007;360:25–31.
[65] Delpech S, Merle-Lucotte E, Auger T, Doligez X, Heuer D, Picard G. MSFR: Material issues and the effect of chemistry control. In: GIF symposium proceeding, Paris, France; 2009. p. 201 – 8.
[66] Cheng H, Leng B, Chen K, Jia Y, Dong J, Li Z, et al. Corros Sci 2015;97:1–6.
[67] Jia Y, Cheng H, Qiu J, Han F, Zou Y, Li Z, et al. J Nucl Mater 2013;441:372–9.
[68] Pavlik V, Kontrik M, Boča M. New J Chem 2015;39:9841–7.
[69] Wang YL, Wang Q, Liu HL, Zeng CL. Corros Sci 2016;103:268–82.
[70] Wang Y, Liu H, Yu G, Hou J, Zeng C. J Fluorine Chem 2015;178:14–22.
[71] Pankratz LB. Thermodynamic properties of halides. Bureau of Mines: United States Department of the Interior; 1984.
[72] Combest R, Levelut MN, Tremillon B. Electrochim Acta 1978;23:1291–5.
[73] De Córdoba G, Caravaca C. J Phys Chem Solids 2006;67:1862–8.
[74] Field PE, Shaffer JH. J Phys Chem 1967;71:3218–22.
[75] Van Norman JD, Tivers RJ. J Electrochem Soc 1971;118:258–9.
[76] Pizzini S, Morlotti R. Electrochim Acta 1965;10:1033–41.
[77] Pizzini S, Sternheim G, Barbi GB. Electrochim Acta 1963;8:227–32.
[78] Pizzini S, Magistris A. Electrochim Acta 1964;9:1189–96.
[79] Kanzaki Y, Takahashi M. J Electroanal Chem Interfacial Electrochem 1975;58:349–56.
[80] Bockris JO'M, Drazic D, Despic AR. Electrochim Acta 1961;4:325 – 61.
[81] Brown LD, Abdulaziz R, Simons S, Inman D, Brett DJL, Shearing PR. J Appl Electrochem 2013;43:1235–41.
[82] Shaffer JH. Preparation and handling of salt mixtures for the molten salt reactor experiment, ORNL-4616. Oak Ridge, TN, USA: Oak Ridge National Laboratory; 1971.
[83] Cherginets VL, Rebrova TP. Electrochim Acta 1999;45:469–76.
[84] Afonichkin V, Bovet A, Shishkin V. J Nucl Mater 2011;419:347–52.
[85] Sohal MS, Ebner MA, Sabarwall P, Sharpe P. Engineering database of liquid salt thermophysical and thermochemical properties, INL/EXT-10-18297. Idoho Falls, ID, USA: Idoho National Laboratory; 2010.
[86] Kondo M, Nagasaka T, Tsisar V, Sagara A, Muroga T, Watanabe T, et al. Fusion Eng Des 2010;85:1430–6.
[87] Jones DA. Principles and prevention of corrosion. Prentice-Hall, Inc.; 1996. p. 86.
[88] Bard AJ, Faulkner LR. Electrochemical methods: fundamentals and applications. John Wiley & Sons, Inc.; 2001. p. 96 – 9.
[89] Wu W, Guo S, Zhang J. J Electrochem Soc 2017;164:C840–4.
[90] Zhang J. J Appl Electrochem 2014;44:383–90.
[91] Hamel C, Chamelot P, Laplace A, Walle E, Dugne O, Taxil P. Electrochim Acta 2007;52:3995–4003.
[92] Wu W, Guo S, Zhang J. Int J Electrochem Sci 2018;13:225–34.
[93] Manning DL, Mamantov G. J Electroanal Chem 1964;7:102–8.
[94] Fabre S, Cabet C, Cassayre L, Chamelot P, Delepech S, Finne J, et al. J Nucl Mater 2013;441:583–91.
[95] Wang YL, Wang Q, Liu HJ, Zeng CL. Corros Sci 2016;109:43–9.

[96] Olson L, Sridharan K, Anderson M, Allen T. J Nucl Mater 2011;411:51–9.
[97] Ouyang F-Y, Chang C-H, Kai J-Jung. J Nucl Mater 2014;446:81–9.
[98] Zheng G, Kelleher B, He L, Cao G, Anderson M, Allen T, et al. Corrosion 2015;71:1257–66.
[99] Ye X-X, Ai H, Guo Z, Huang H, Jiang L, Wang J, et al. Corros Sci 2016;106:249–59.
[100] Kaesche H. Corrosion of metals: physicochemical principles and current problems. Springer-Verlag; 2003. p. 169.
[101] Koger JW. Alloy compatibility with LiF-BeF$_2$ salts containing ThF$_4$ and UF$_4$, ORNL-TM-4286. Oak Ridge, TN, USA: Oak Ridge National Laboratory; 1972.
[102] Keiser JR. Compatibility studies of potential molten-salt breeder reactor materials in molten fluoride salts, ORNL/TM-5783. Oak Ridge, TN, USA: Oak Ridge National Laboratory; 1977.
[103] Kondo M, Nagasaka T, Xu Q, Muroga T, Sagara A, Noda N, et al. Fusion Eng Des 2009;84:1081–5.
[104] Kondo M, Nagasaka T, Sagara A, Noda N, Muroga T, Xu Q, et al. J Nucl Mater 2009;386–388:685–8.
[105] Misra AK, Whittenberger JD. Fluoride salts and container materials for thermal energy storage applications in the temperature range 973 to 1400 K, NASA Lewis Technical Memorandum 89913. National Aeronautics and Space Administration 1987.
[106] MacPherson HG. Nucl Sci Eng 1985;90:374–80.
[107] Jordan WH, Cromer SJ, Miller AJ. Aircraft nuclear propulsion project quarterly progress report, ORNL-2106, Parts 1–5. Oak Ridge, TN, USA: Oak Ridge National Laboratory; 1956.
[108] Frye JH, Manly WD, Cunningham JE. Metallurgy division annual progress report, ORNL-2422. Oak Ridge, TN, USA: Oak Ridge National Laboratory; 1957.
[109] Franke P, Neuschütz D. Mo-Ni. In: Franke P, Neuschütz D, editors. Binary systems. Part 4: Binary systems from Mn-Mo to Y-Zr. Berlin, Heidelberg: Springer-Verlag; 2006. p. 1–3.
[110] Holcomb DE, Cetiner SM, Flanagan GF, Peretz FJ, Yoder Jr GL. An analysis of testing requirements for fluoride salt-cooled high temperature reactor components, ORNL/TM-2009/297. Oak Ridge, TN, USA: Oak Ridge National Laboratory; 2009.
[111] Cottrell WB, Crabtree TE, Davis AL, Piper WG. Disassembly and postoperative examination of the aircraft reactor experiment, ORNL-1868. Oak Ridge, TN, USA: Oak Ridge National Laboratory; 1958.
[112] MacPherson HG, Alexander LG, Carrison DA, Estabrook JY, Kinyon BW, Mann LA, et al. A preliminary study of molten salt power reactors, CF-57-4-27 (Rev.). Oak Ridge, TN, USA: Oak Ridge National Laboratory; 1957.
[113] Manly WD, Adamson Jr GM, Coobs JH, DeVan JH, Douglas DA, Hoffman EE, et al. Aircraft reactor experiment – metallurgical aspects, ORNL-2349. Oak Ridge, TN, USA: Oak Ridge National Laboratory; 1957.
[114] Koger JW. Effect of FeF$_2$ addition on mass transfer in a Hastelloy N – LiF-BeF$_2$-UF$_4$ thermal convection loop system, ORNL-TM-4188. Oak Ridge, TN, USA: Oak Ridge National Laboratory; 1972.
[115] MacPherson HG. Molten-salt reactor program quarterly progress report, ORNL-2474. Oak Ridge, TN, USA: Oak Ridge National Laboratory; 1958.
[116] MacPherson HG. Molten-salt reactor program quarterly progress report, ORNL-2799. Oak Ridge, TN, USA: Oak Ridge National Laboratory; 1959.
[117] MacPherson HG. Molten-salt reactor program quarterly progress report, ORNL-2973. Oak Ridge, TN, USA: Oak Ridge National Laboratory; 1960.
[118] MacPherson HG. Molten-salt reactor program quarterly progress report, ORNL-2723. Oak Ridge, TN, USA: Oak Ridge National Laboratory; 1959.
[119] Briggs RB. Molten-salt reactor program quarterly progress report, ORNL-3215. Oak Ridge, TN, USA: Oak Ridge National Laboratory; 1961.
[120] Stopher MA. Mater Sci Technol 2017;33:518–36.
[121] McCoy Jr HE. Status of materials development for molten salt reactors, ORNL-TM-5920. Oak Ridge, TN, USA: Oak Ridge National Laboratory; 1978.
[122] Ignatiev V, Surenkov A. J Nucl Mater 2013;441:592–603.
[123] Koger JW. Evaluation of Hastelloy N alloys after nine years exposure to both a molten fluoride salt and air at temperatures from 700 to 560 °C, ORNL-TM-4189. Oak Ridge, TN, USA: Oak Ridge National Laboratory; 1972.
[124] Ouyang F-Y, Chang C-H, You B-C, Yeh T-K, Kai J-J. J Nucl Mater 2013;437:201–7.
[125] Liu M, Zheng J, Liu Y, Li Z, Zou Y, Yu X, et al. J Nucl Mater 2013;440:124–8.
[126] Sona CS, Gajbhiye BD, Hule PV, Patwardhan AW, Mathpati CS, Borgohain A, et al. Corros Eng Sci Technol 2014;49:287–95.
[127] Olson LC, Fuentes RE, Martinez-Rodriguez MJ, Ambrosek JW, Sridharan K, Anderson MH, et al. J Sol Energy Eng 2015;137:061007-1 – 061007-8.
[128] Predel B. Ni-Te (nickel-tellurium). In: Madelung O, editor. Ni-Np – Pt-Zr. Berlin Heidelberg: Springer-Verlag; 1998. p. 1–4.
[129] Lejček P, Šob M, Paidar V. Prog Mater Sci 2017;87:83–139.
[130] Cheng H, Han F, Jia Y, Li Z, Zhou X. J Nucl Mater 2015;461:122–8.
[131] Keiser JR. Status of tellurium – Hastelloy N studies in molten fluoride salts, ORNL/TM-6002. Oak Ridge, TN, USA: Oak Ridge National Laboratory; 1977.
[132] Ignatiev V, Surenkov A, Gnidoy I, Kulakov A, Uglov V, Vasiliev A. J Nucl Mater 2013;440:243–9.
[133] Qiu J, Zhou Y, Yu G, Liu H, Jia Y, Li Z, et al. J Fluorine Chem 2014;168:69–74.
[134] Olson LC. Materials corrosion in molten LiF-NaF-KF eutectic salt. Ph.D. dissertation. Madison, WI, USA: University of Wisconsin-Madison; 2009.
[135] Wang Y, Liu H, Zeng C. J Fluorine Chem 2014;165:1–6.
[136] Ozeryanaya I. Met Sci Heat Treat 1985;27:184–8.
[137] Yoko T, Bailey RA. J Electrochem Soc 1984;131:2590–5.
[138] Peng H, Shen M, Wang C, Su T, Zuo Y, Xie L. RSC Adv 2015;5:76689–95.
[139] Greenwood LR, Garner FA. J Nucl Mater 1996;233–237:1530–4.
[140] Garner F, Greenwood L, Oliver B. A re-evaluation of helium/dpa and hydrogen/dpa ratios for fast reactor and thermal reactor data used in fission-fusion correlations, IAEA-TECDOC-1039. Obnisk, Russian Federation: Proceeding of a Technical Committee Meeting; 1997.
[141] Zhu H, Holmes R, Hanley T, Davis J, Short K, Edwards L. Corros Sci 2015;91:1–6.
[142] DeVan JH. Effect of alloying additions on corrosion behavior of nickel-molybdenum alloys in fused fluoride mixtures, ORNL-TM-2021 Vol. 1. Oak Ridge, TN, USA: Oak Ridge National Laboratory; 1969.
[143] Olson L, Sridharan K, Anderson M, Allen T. Mater High Temp 2010;27:145–9.
[144] Olson LC, Ambrosek JW, Sridharan K, Anderson MH, Allen TR. J Fluorine Chem 2009;130:67–73.
[145] Li X, He S, Zhou X, Huai P, Li Z, Li A, et al. J Nucl Mater 2015;464:342–5.
[146] Li XL, He SM, Zhou XT, Zou Y, Li ZJ, Li AG, et al. Mater Charact 2014;95:171–9.
[147] Xu Z, Jiang L, Dong J, Li Z, Zhou X. J Alloy Compd 2015;620:197–203.
[148] Wang YL, Wang Q, Liu HJ, Zeng CL. RSC Adv 2015;5:32755–60.
[149] Williams DF, Clarno KT. Nucl Technol 2008;163:330–43.
[150] Hosoya Y, Terai T, Yoneoka T, Tanaka S. J Nucl Mater 1997;248:348–53.
[151] Vignarooban K, Pugazhendhi P, Tucker C, Gervasio D, Kannan AM. Sol Energy 2014;103:62–9.
[152] Wang J-W, Zhang C-Z, Li Z-H, Zhou H-X, He J-X, Yu J-C. Sol Energy Mater Sol Cells 2017;164:146–55.
[153] Gomez-Vidal JC, Fernandez AG, Tirawat R, Turchi C, Huddleston W. Sol Energy Mater Sol Cells 2017;166:222–33.
[154] Jeong SM, Shin H-S, Cho S-H, Hur J-M, Lee HS. Electrochim Acta 2009;54:6335–40.
[155] Sakamura Y, Omori T, Inoue T. Nucl Technol 2008;162:169–78.
[156] Colom F, Bodalo A. Corros Sci 1973;12:731–8.
[157] Nishikata A, Numata H, Tsuru T. Mater Sci Eng A 1991;146:15–31.
[158] Shankar AR, Kanagasundar A, Mudali UK. Corrosion 2013;69:48–57.
[159] Shankar AR, Thyagarajan K, Mudaili UK. Corrosion 2013;69:655–65.
[160] Rao ChJ, Shankar AR, Ajikumar PK, Kamruddin M, Mallika C, Mudali UK. Corrosion 2015;71:502–9.
[161] Indacochea JE, Smith JL, Litko KR, Karell EJ. J Mater Res 1999;14:1990–5.
[162] Indacochea JE, Smithm JL, Litko KR, Karell EJ, Raraz AG. Oxid Met 2001;55:1–16.

[163] Ruh A, Spiegel M. Corros Sci 2006;48:679–95.
[164] Kawahara Y. Corros Sci 2002;44:223–45.
[165] Shen Y, Zhang J. J Rare Earths 2017;35:187–92.
[166] Ambrosek JW. Molten chloride salts for heat transfer in nuclear systems Ph.D. thesis Madison, WI, USA: The University of Wisconsin-Madison; 2011.
[167] Shankar AR, Mathiya S, Thyagarajan K, Mudali UK. Metall Mater Trans A 2010;41:1815–25.
[168] Cho SH, Park SB, Lee JH, Hur JM, Lee HS. J Nucl Mater 2011;412:157–64.
[169] Liu S, Liu Z, Wang Y, Tang J. Corros Sci 2014;83:396–408.
[170] Littlewood R, Argent EJ. Electrochim Acta 1961;4:155–69.
[171] Feng XK, Melendres CA. J Electrochem Soc 1982;129:1245–9.
[172] Cho SH, Zhang JS, Shin YS, Park SW, Park HS. J Nucl Mater 2004;325:13–7.
[173] Shankar AR, Mudali UK. Mater Corros 2008;59:878–82.
[174] Salinas-Solano G, Porcayo-Calderon J, Gonzalez-Rodriguez JG, Salinas-Bravo VM, Ascencio-Gutierrez JA, Martinez-Gomez L. Adv Mater Sci Eng 2014;2:1–8.
[175] Polovov IB, Abramov AV, Rebrin OI, Volkovich VA, Denisov EI, Griffiths TR, et al. ECS Trans 2010;33:321–7.
[176] Wang L, Li B, Shen M, Li S, Yu J. Int J Miner Metall Mater 2012;19:930–3.
[177] Li YS, Spiegel M. Oxid Met 2004;61:303–22.
[178] Cho Sh, Park SB, Lee JH, Hur JM, Lee HS. J Nucl Mater 2011;412:157 – 64.
[179] Gibilaro M, Massot L, Chamelot P. Electrochim Acta 2015;160:209–13.
[180] Keiser JR, DeVan JH, Lawrence EJ. J Nucl Mater 1979;8586:295–8.
[181] Calderoni P, Sharpe P, Nishimura H, Terai T. J Nucl Mater 2009;386–388:1102–6.
[182] Fukada S, Simpson MF, Anderl RA, Sharpe JP, Katayama K, Smolik GR, et al. J Nucl Mater 2007;367–370:1190–6.
[183] Simpson MF, Smolik GR, Sharpe JP, Anderl RA, Petti DA, Hatano Y, et al. Fusion Eng Des 2006;81:541–7.
[184] Hara M, Hatano Y, Simpson MF, Smolik GR, Sharp JP, Oya Y, et al. Fusion Eng Des 2006;81:561–6.
[185] Olson LC, Gray JR, Martinez-Rodriguez MJ, Fuentes RE, Garcia-Diaz BL. ECS meeting abstracts, 229th ECS meeting, 2016, San Diego, CA. Abstract 966.
[186] Sellers RS, Cheng WJ, Anderson MH, Sridharan K, Wang CJ, Allen TR. Materials corrosion in molten LiF-NaF-KF eutectic salt under different reduction-oxidation conditions. In: Proceedings of ICAPP'12, Chicago, USA; 2012. Paper no. 12189.
[187] Dai Q, Ye X-X, Ai H, Chen S, Jiang L, Liang J, et al. Corros Sci 2018;133:349–57. https://doi.org/10.1016/j.corsci.2018.01.026.
[188] Mehrabadi BAT, Weidner JW, Garcia-Diaz B, Martinez-Rodriguez M, Olson L, Shimpalee S. J Electrochem Soc 2016;163:C830–8.